

**Phase Change Metamaterials for Fiber and Waveguide Integrated
Compact Modulators with Built in Memory Functionality**

by

Yihao Cui

A thesis submitted in partial fulfillment of the requirements for the degree of

Master of Science

in

Photonics and Plasma

Department of Electrical and Computer Engineering
University of Alberta

© Yihao Cui, 2023

Abstract

Machine learning focuses on the development of algorithms and models that enable a dynamic approach to making predictions or decisions on large data-sets which cannot be readily described by analytical models. Artificial neural networks (ANN) have become the main approach to providing advance functionalities such as pattern recognition, and inference calculations with improved performance through experience and iterative training cycles. Inspired by the structural organization of a biological brain, ANNs consist of interconnected layers of artificial neurons, or nodes, where input signals are weighted, pooled, and passed on to the next layer for analysis. Leveraging the computational hardware performance gains in application specific integrated circuits (ASICs) such as graphics processing units (GPUs), ANNs have proliferated in applications ranging from image recognition, natural language processing, autonomous vehicles, and medical diagnosis. However, the computational requirements for floating-point operations of increasingly complex ANN models have far exceeded performance trends predicted by Moore's Law. Additionally, data movement between arithmetic and memory modules on metallic interconnects in ANN hardware accelerators does not scale in terms of energy consumption, latency, and bandwidth. The incorporation of chalcogenide phase-change metamaterials on photonic platforms such as optical fibers and photonic integrated circuits (PICs) offers a

compact, reversible, and non-volatile device platform to realize a largely distributed and parallel optical computing architecture to accelerate training and inference calculations of ANNs. We demonstrate a cuboid-based germanium antimony telluride (GST) metamaterial integrated on the tip of an optical fiber with a high intensity contrast and switchable group delay dispersion between amorphous and crystalline phases for long haul telecommunication signal transmission across network nodes. Similarly, by eliciting an all-dielectric metamaterial resonance in a subwavelength structured GST grating, an optically or electrically addressable synaptic weight was realized on photonic silicon nitride waveguides. The resonator’s wavelength tunability enables symmetric 30% transmission modulation for both positive and negative weighting values across amorphous and crystalline phases. Lastly, benefiting from the high infrared transparency and the large refractive index contrast between the two phases ($\Delta n > 2.0$ for certain alloy compositions), the thin film inclusion of phase-change materials on photonic waveguide circuits enables efficient and ultra-compact phase-shifter elements with memory functionalities. Furthermore, effective medium metamaterial design concepts allow for specified dispersion engineering required for low insertion loss ($< 0.3dB$) and compact footprint ($L_\pi = 5 - 20\mu m$) designs. Such non-volatile phase-shifters can be embedded within a cascaded MZI mesh to implement a programmable zero static energy consumption matrix vector multiplication layer for an interconnected neural network.

Preface

Mandatory due to collaborative work

Chapter 4 of this thesis has been published as Tiago Martins, Yihao Cui, Behrad Gholipour, Jun-Yu Ou, Orlando Frazao, Kevin F. MacDonald, "Fiber-Integrated Phase Change Metasurfaces with Switchable Group Delay Dispersion", *Adv. Optical Mater* 2021, 9, 2100803. Tiago had performed preliminary simulation work on the GST-based cuboid metasurface and had also carried out the fabrication and experimental characterization of the device in the optoelectronics research centre based in the University of Southampton. I remodeled the fabricated device with the addition of rounded features to accurately portray the measured device. Transmission and phase data was extracted from the simulation models which was analyzed and plotted to produce line and colormap diagrams.

Chapters 1, 3 and 5 consist of my own original work. Staff from the NanoFAB (Aaron Hryciw, Gustavo de Oliveira Luiz and Scott Munro) aided in contributing to the recipe development in chapter 6 involving the layout and fabrication of silicon nitride photonic circuits.

This thesis is dedicated to my parents. I would like to express my appreciation and gratitude towards them for making this endeavour a possibility. It is with their unwavering support for my pursuit of higher education that I can now proudly claim my Masters degree.

Acknowledgements

I would like to express my deepest gratitude towards members of the NanoFAB staff: Aaron Hryciw and Gustavo de Oliveira Luiz. The fabrication and recipe development of my silicon nitride photonics circuits could not have succeeded if it wasn't for their involvement with both deposition/characterization of stoichiometric silicon nitride thin film, and patterning/exposure of photonic components and circuits. The accessibility and support of the Raith GDSII MATLAB toolbox made the process of creating layouts of photonic components, circuits, and testing elements a simple and streamlined process. They were eager to help, teach and aid in my endeavour to develop my exposure recipe parameters, it cannot be overstated that working with Aaron and Gustavo was an absolute pleasure. I am forever grateful.

I'd like to recognize and acknowledge the helpful advice and contributions made by my committee members: Professor Ying Tsui and Professor Vien Van. Specifically, I appreciate the opportunity to attend Dr. Van's ECE 770 course where the lessons learned in that class formed the theoretical basis for my PCM-MZI work.

Research in any capacity cannot be completed in isolation and will always constitute collaboration; therefore, I want to recognize the contributions and productive conversations I've had with Avik Mandal, Ravindu Karunathilake, Kwanghyun Kim, Abbas Sheiki Ansari, Viraj Bhingardive, and Hanfa Song.

Table of Contents

1	Introduction	1
2	Research Objectives	6
3	Literature Review	8
3.1	Metamaterial and Metasurfaces	8
3.2	Chalcogenide Phase Change Materials	10
3.3	Chalcogenide Phase Change Metamaterials	14
3.4	Optical Fiber Integrated Metamaterials	17
3.5	Optical Acceleration of ANNs	22
4	Fiber Integrated Phase Change Metasurfaces With Switchable Group Delay Dispersion	37
5	Chalcogenide Phase-Change Material Integration on Photonic Waveguide Structures	51
5.1	Optically large rectangular waveguides with thin film chalcogenide phase-change material	53
5.2	Addition of resonant GST metamaterial on silicon nitride integrated photonic waveguides	64
5.3	Addition of effective medium based PCM metamaterial on integrated photonic waveguides for dispersion engineering	81
5.4	Reconfigurable non-volatile MZI phase-shifters based on thin film Chalcogenide PCM	89

6 Photonic Silicon Nitride Process Design Kit Development	108
6.1 Stoichiometric silicon nitride material and design of waveguide dimensions	109
6.2 Waveguide coupling and design of power splitters for TE polarization	113
6.3 Design of photonic grating coupler constrained by fabrication limitations	121
6.4 Fabrication process flow, exposure compensation, and scripted GDS layout	128
7 Conclusion & Future Challenges	137
7.1 Conclusion	137
7.2 Future Challenges	139
References	141
Appendix A: Fiber-integrated phase change metasurface with switchable group delay dispersion	158
Appendix B: Chalcogenide phase change MZI phase-shifters	161
Appendix C: Silicon nitride photonic fabrication	165

List of Figures

3.1	Properties of GST-based phase change materials. a.) schematic illustration of the reversible switching between amorphous and crystalline material phases with different pulsing protocols. b.) the stoichiometric dependent change in reflectivity across amorphous/crystalline phases within the ternary composition. c.) figure of merit for various germanium based PCM alloys.	11
3.2	Various metamaterial demonstrations with inclusion of chalcogenide phase change material. a.) asymmetric plasmonic split ring resonator modulated with adjacent GST thin film. b.) excitation of longitudinal resonant modes within subwavelength nanostructured GST gratings. c.) patterning of Frensel lenses in a GST substrate through direct laser amorphization/crystallization. d.) meta-lens with tunable focal lengths between amorphous and crystalline phases.	16
3.3	Optical fiber integrated meta-lens demonstrations. a.) phase-gradient plasmonic metasurface on a photonic crystal fiber. b.) all-dielectric TiO ₂ based meta-lens integration with focusing efficiencies of 70%. c.) inverse designed meta-lens fabricated with two-photon absorption 3D printing technique.	18
3.4	Hierarchical overview of a fully connected neural network: neurological connections of a biological brain is represented within a DNN as input and output layers separated by interconnected hidden layers performing weighted summation operations with a non-linear threshold activation which can be represented as matrix vector multiplications.	23

3.5	Neural network hardware accelerators based on photonic Mach-Zehnder interferometer networks. a.) two MZI configurations to implement an equivalent unitary matrix transformation. b.) optical interference unit fabricated on SOI platform for vowel recognition. c.) programmable linear optical processor based on singular value decomposition.	26
3.6	Examples of arrayed banks of micro-ring resonators implementing matrix vector operation with wavelength division multiplexing scheme. a.) positive value matrix vector multiplication. b.) matrix computation for massive MIMO communication systems. c.) schematic illustration of "broadcast and weight" scheme. d.) programmable cross-bar arrays of microdisk resonator cavities for signal processing. .	29
3.7	Chalcogenide phase change material integration with MZI circuits. a.) GST patch on silicon nitride rib waveguide platform. b.) single arm GST actuation in an unbalanced MZI. c.) addition of low loss Sb ₂ S ₃ PCM on MZI for reduced insertion losses. d.) dynamic control and reconfigurability of a shifted MZI spectra hybridized with Sb ₂ Se ₃ material.	33
3.8	Phase change material integration on photonic micro-ring resonators. a.) spectrally separated MRRs attenuating input signal at different resonant wavelengths. b.) binary switching of MRR resonant behaviour between amorphous and crystalline GST phases. c.) discretized GST nanodisks to achieve intermediate transmission values upon successive phase transition of the individual structures.	35
4.1	a.) Near-infrared spectral dispersion of the refractive index (n) and the extinction coefficient (κ) of GST in the amorphous (blue) and crystalline (red) phases. b.) schematic diagram of the fiber-integrated phase change metasurface optical switch based on GST. c.) scanning electron microscope image of the fiber metadvice; inset, detail of the cuboid GST metasurface structure.	42

4.2	a.) experimentally measured and b.) simulated transmission spectra for arrays of GST cubes with $w = 80nm$, $t = 200nm$ and P taking three different values: 900, 950, 1000nm. c.) corresponding simulated spectral profile of the Group Delay Dispersion (GDD); the grey dashed line identifies the level of dispersion introduced by 1m of single-mode telecom fiber (considering a fiber group velocity dispersion of 20 ps/nm km); the black, red, and blue dashed traces show the off-resonance GDD for arrays with $P = 900, 950, 1000nm$, respectively.	44
4.3	a.) measured and b.) simulated transmission spectra for a metasurface with $w = 80nm$, $t = 200nm$, $P = 900nm$, in the amorphous (black) and crystalline (red) phases; along with corresponding numerically simulated transmission of metasurfaces ranging from 850nm to 1050nm periods in c.) amorphous and d.) crystalline states, with resonances covering the E, S, and C telecommunication bands.	46
4.4	Numerically simulated GDD for amorphous and crystalline states of a metasurface with $w = 80nm$, $t = 200nm$, $P = 900nm$, along with corresponding b.) phase and c.) FOM calculated for metasurfaces with periods ranging from 850nm to 1050nm. The color black indicates FOM=0. Magenta line indicates the region where $T_a = T_c$	48
5.1	Simulation workflow diagram to analyze PCM integrated waveguide devices. From left to right, waveguide characteristics are first determined with MODE solutions, the mode propagates in 3D FDTD environment down the device where ports extract relevant S-parameters, and subsequently overall circuit response is generated from INTERCONNECT with the imported compact model.	52
5.2	Schematic of chalcogenide phase change material incorporated on a large dimension silicon nitride photonic waveguide in a thin film format (left) and a metasurface subwavelength grating structure (right) to modulate signal intensities at designated wavelengths of interest.	53

5.3	Material dispersion profile of silicon, silicon nitride and GST-255 across the telecommunication wavelengths: ranging from the O-band to the L-band. a.) Refractive index and b.) extinction coefficient	55
5.4	Cross section of the GST integrated waveguide (signal propagation in the z-direction) intensity modulator for different core materials: a.) silicon, b.) silicon dioxide, c.) silicon nitride	56
5.5	Spectral tunability of GST thin film integrated photonic waveguide demonstrated with changing thicknesses. Thicknesses of 500nm, 550nm, and 600nm correspond to resonances centered at $\lambda = 1367nm$, $1467nm$, and $1565nm$ respectively.	58
5.6	a.) transmission for a range of GST patch lengths ($40\mu m$ to $100\mu m$) in the waveguide propagation direction for a constant thickness of 550nm. b.) transmission depth as a function of varying GST thin film length, defined as the transmission delta between off-resonance ($\lambda = 1300nm$) and on-resonance ($\lambda = 1467nm$).	59
5.7	Reconfigurability of phase change GST illustrates signal intensity modulation. a.) amorphous GST produce 3 distinct metamaterial resonance responses with the main resonance interaction centered at 1428nm, while crystalline GST produces a flat high transmission response. b.) Modal field interaction with the amorphous GST meta-gratings. c.) Transmission contrast between amorphous and crystalline phases. d.) the lack of modal field interaction with crystalline GST meta-gratings.	61
5.8	Changes in the period of nanograting metasurface show tunable narrowband to wideband operation across the telecommunication spectrum for a.) Period = 750nm, b.) Period = 850nm, c.) Period = 950nm	62
5.9	Corresponding group delay dispersion profiles for periods of 750nm, 850nm, and 950nm. Solid line shows the amorphous phase, while dashed line represents the crystalline phase.	64

5.10	Optical characteristics of silicon nitride waveguides offered by the ANT process design kit. a.) the effective index for the fundamental TE polarization mode for various waveguide width dimensions compared to oxide refractive index baseline. b.) the insertion loss associated with a 90-degree bend considering interface mode mismatch and propagation loss for various bend radii for the chosen waveguide dimensions of $400nm \times 750nm$	66
5.11	Schematic of the proposed chalcogenide phase-change intensity modulator based on silicon nitride waveguide platform (left) and close up of the metasurface device defined by physical dimensions such as buffer thickness, PCM thickness, period, and slot width (right).	67
5.12	The metamaterial resonant behaviour with and without the inclusion of a 100nm thick ITO buffer layer. a.) overall spectrum for both configurations within the range of 1500 – 1600nm. b.) electric field intensity of the waveguide mode interaction with GST grating metasurface separated by 100nm of ITO at 1515nm. c.) electric field intensity of the waveguide mode interaction with GST grating metasurface separated by 100nm of ITO at 1560nm.	70
5.13	Comparison across the two spectral response generated from crystalline and amorphous phases. a.) transmission for amorphous (black) and crystalline (red) GST. b.) electric field intensity of the GST meta-grating in amorphous phase. c.) electric field intensity of the GST meta-grating in crystalline phase.	71
5.14	Resonance tuning of the GST meta-grating modulator by adjusting a.) period and b.) duty cycle	73
5.15	Spectral response of GST meta-grating with the inclusion of silicon dioxide as buffer layer material. a.) resonance tuning by adjusting period of the meta-grating structure. b.) electric field intensity of amorphous GST meta-grating with structure outline showing resonance centered at $\lambda = 1555nm$, for a period of 850nm.	74

5.16	Comparison of spectral response for two periods at 850nm (black) and 880nm (red) for both amorphous and crystalline phases, represented by solid and dashed lines respectively. Blue arrow indicated the transmission contrast achievable for a shifted resonance spectrum	76
5.17	Electric field intensity distribution between the waveguide and the GST meta-grating structure with a period of 850nm for a.) amorphous, b.) crystalline GST and contrasted with a shifted response for amorphous GST with period of 880nm	76
5.18	a.) spectral response for the GST meta-atom micro-block resonator in amorphous (black) and crystalline (red) material phase, b.) electric field intensity of the resonant coupling within amorphous GST meta-atom, c.) electric field intensity demonstrating the absence of resonant coupling within crystalline GST meta-atom.	78
5.19	Resonance tuning of the GST meta-atom block by adjusting parameters such as a.) thickness and b.) length dimensions.	79
5.20	a.) Spectral response of the buried (black) and top (red) configuration for the placement of ITO micro-heater component, b.) electric field intensity showing the buried configuration, c.) electric field intensity showing the top configuration.	80
5.21	Schematic of a Mach Zehnder Interferometer (MZI) circuit (left) with the incorporation of a non-resonant metasurface phase-change material for a dispersion engineered phase response (right).	84
5.22	The achieved effective index variations, represented by color, for various duty cycles for a GST and silicon dioxide material pair across the telecom C-band spectrum in a.) amorphous phase and b.) crystalline phase.	86
5.23	a.) The effective index difference between amorphous and crystalline phases, represented as color, for a range of duty cycles. b.) The effective index difference as a function of increasing duty cycle at a singular wavelength of 1550nm.	87

5.24	GST metasurface phase-shifter integration on a single arm MZI configuration; a.) the calculated phase difference between amorphous and crystalline states for various patch lengths to determine minimum length required to achieve π phase shift, b.) overall spectral response from the MZI GST metasurface phase-shifter for amorphous (red) and crystalline (black) phases.	88
5.25	a.) Effective index difference between amorphous and crystalline phases for a GST and ITO material combination. b.) The calculated phase difference between amorphous and crystalline phases for various metasurface patch lengths for two duty cycles: $dc = 0.357$ ($W_{pcm} = 107nm$, black) and $dc = 0.643$ ($W_{pcm} = 193nm$, red).	89
5.26	Schematic cartoon depicting the integration of chalcogenide phase-change material on MZI photonic circuits. a.) Single arm integration of PCM-based phase shifters. b.) dual arm or push-pull integration of PCM-based phase shifters.	90
5.27	a.) The effective index difference between the amorphous and crystalline states for four different PCM alloys: $Ge_2Sb_2Te_5$ (orange), $Ge_2Sb_2Se_4Te_1$ (blue), Sb_2Se_3 (red), and Sb_2S_3 (green). Inset shows the cross-sectional silicon nitride waveguide geometry with PCM thin film integration. b.) The physical patch length difference between a single and dual arm configuration to achieve the required π phase shift.	95
5.28	Achievable phase-difference between arms of a MZI visualized as a distribution of color based on the effective index difference and patch length for a.) single arm integration and b.) dual arm integration.	97
5.29	The cross-sectional parameter design space for thin film PCM integration on photonic waveguides with (c,d) and without (a,b) the inclusion of micro-heater element ITO. The first row of colormaps illustrate the achievable effective index contrast between amorphous and crystalline phases for without (a) and with 100nm of ITO (c). The second row is the associated range of patch lengths required for a π phase shift for without (b) and with 100nm of ITO (d).	98

5.30	The achievable phase-difference between arms of a MZI visualized as a distribution of color based on the effective index difference and patch length with the addition of ITO for a.) single arm integration and b.) dual arm integration.	101
5.31	Differentiation between single mode and hybrid mode operation depending on the thickness of the integrated SbS layer; a.) plot of the effective index for SbS thickness ranging from 0-150nm with a grey dashed line demarcating the separation between single and hybrid mode operation. X-component electric field intensity distribution for SbS thickness of 86nm in b.) first mode amorphous phase, c.) first mode crystalline phase, and d.) second mode crystalline mode.	102
5.32	Spectral response of SbS integrated MZI photonic circuit in a.) single arm configuration and b.) dual arm configuration.	103
5.33	Comparison between spectral response for photonic MZI circuits with different phase-shift elements including a.) phase-change materials, b.) thermo-optic effect, c.) charge carrier modulation in PN junctions.	105
6.1	Dispersion profile of stoichiometric silicon nitride at a thickness of 300nm, deposited through LPCVD. Dashed and solid lines represent pre-thermal annealing and post-thermal annealing respectively. Blue correspond to the refractive index and orange refers to the extinction coefficient.	110
6.2	Properties of the chosen silicon nitride waveguide dimensions; electric field intensity distribution for a.) TE polarization and b.) TM polarization, c.) effective indices of the first fundamental and second waveguide modes for TE and TM polarizations, d.) bend radii for both polarizations with an insertion loss value of -0.1dB marked by a grey dashed line.	112
6.3	Parallel waveguide coupling dynamics; real component of the x direction electric field for a.) symmetric supermode and b.) anti-symmetric supermode. c.) The resulting cross over length for a given waveguide separation gap fitted with an exponential relation.	115

6.4	Properties and characteristics of 3dB directional coupler; a.) insertion loss for a waveguide s-bend geometry of various lengths, b.) electric field intensity distribution of the directional coupler at an operating wavelength of 1550nm, c.) spectral response for the cross (black) and bar (red) ports of the 3dB directional coupler.	117
6.5	Design and simulation of Y-branch splitter/combiner; a.) schematic of the discretized splitter geometry into several distinct width parameters, b.) broadband transmission response at the output with inset showing the electric field intensity distribution at wavelength of 1550nm.	120
6.6	Design and simulation of TE grating coupler; a.) cross sectional schematic of a fully etched apodized grating structure, b.) spectral response of a 2D apodized grating with inset showing coupling of electric field from free space into the slab waveguide.	124
6.7	Performance comparison between two waveguide taper geometries; electric field intensity distribution for a.) a linear and b.) sine parabolic shape. c.) Broadband transmission response for linear (black) and sine parabolic (red).	126
6.8	Normalized spectral response of the optimized TE grating coupler with red dashed line marking the 1dB value to illustrate the bandwidth of the coupling efficiency.	127
6.9	Typical process flow for the fabrication of photonic integrated circuits based on low loss stoichiometric silicon nitride material.	130
6.10	Incorrect exposure of patterns and geometries due to the presence of the proximity effect inherent to electron beam based lithography techniques. Top cartoon show the dispersion of incident electrons leading to a broadening and over exposure of adjacent features. Bottom SEM image show at sufficient exposure doses closely spaced features will merge into one.	131

6.11	The process of proximity effect correction; starting with a.) Monte Carlo simulation of electron trajectories incident on a layer stack of resist and silicon nitride material, b.) normalized energy distribution along the radial direction away from the center of the incident beam, c.) simulated post-exposure photoresist profile with dose correction applied, d.) exposure dose fracturing applied to the grating coupler GDS layout.	134
6.12	Fabricated grating coupler with the application of proximity effect correction (fractured exposure dosage pattern); a.) top view of the fabricated grating coupler with an inset representing variable exposure dosage as color, b.) cross sectional view of fabricated grating coupler cut with focused ion beam milling.	135
6.13	Development of MATLAB based toolbox for layout and exposure preparation; a.) hierarchical organization of layout classes and definitions, b.) layout of waveguide spiral based on FBMS lines with text elements, c.) arrayed layout of various components and geometries consisting of grating coupler, waveguides and single pixel lines. .	136
A.1	Numerically simulated change in transmission between amorphous and crystalline phases for metasurface ranging from 850nm to 1050nm periods.	159
A.2	Electric (a.,b.) and magnetic (c.,d.) field distribution of a metasurface with $w = 80nm$, $t = 200nm$, and $P = 900nm$, in the amorphous (a.,c.) and crystalline (b.,d.) crystalline phases; plotted at their respective resonance wavelengths.	160
B.1	GDS layout of sample photonic chip submitted for fabrication with Applied Nanotools containing various MZI circuit configurations with PCM and passive photonic calibration circuits for testing.	162
B.2	Expanded view of the passive calibration circuits for evaluating and comparing the performance of photonic silicon nitride micro-ring resonators, TE polarization grating couplers, 1x2 50% y-branch splitters and combiners, 2x2 3dB directional couplers and spiral waveguides. .	163

B.3	11 Column array of MZI with the incorporation of PCM in both single and dual arm configurations with metallic electrode integration to actuate a phase transition through thermal switching.	164
C.1	Silicon dioxide thickness measurement of a 4-inch wafer via spectroscopic reflectometry tool: Filmetrics.	165
C.2	Stoichiometric silicon nitride thickness measurement of a 4-inch wafer with Filmetrics metrology tool. Thickness values are represented as color with violet and red corresponding to the minimum and maximum values respectively.	166
C.3	Thickness measurement of photoresist Ma-N2403 on silicon nitride sample chip with Filmetrics.	167

Abbreviations

AI Artificial Intelligence.

ANN Artificial Neural Network.

ANT Applied Nanotools.

ASIC Application Specific Integrated Circuit.

CMOS Complementary Metal Oxide Semiconductor.

CVD Chemical Vapour Deposition.

DBR Distributed Bragg Reflector.

DCS DiChloroSilane.

DNN Deep Neural Network.

EBL Electron Beam Lithography.

FDE Finite Difference Eigenmode.

FDTD Finite Difference Time Domain.

FOM Figure of Merit.

FP Fabry Perot.

GD Group Delay.

GDD Group Delay Dispersion.

GDS Graphic Design System.

GPU Graphics Processing Unit.

GST Germanium Antimony Telluride.

ICPRIE Inductively Coupled Plasma Reactive Ion Etching.

ITO Indium Titanium Oxide.

LIDAR Light Imaging Detection and Ranging.

LPCVD Low Pressure Chemical Vapour Deposition.

MFD Modal Field Diameter.

ML Machine Learning.

MMI Multimode Interference.

MRR Micro Ring Resonator.

MZI Mach Zehnder Interferometer.

PCM Phase Change Material.

PCRAM Phase Change Random Addressable Memory.

PDM Polarization Division Multiplexing.

PIC Photonic Integrated Circuit.

PML Perfectly Matched Layers.

PSO Particle Swarm Optimization.

PVD Physical Vapour Deposition.

SDM Spatial Division Multiplexing.

SEM Scanning Electron Microscope.

SGD Stochastic Gradient Decent.

SOI Silicon on Insulator.

SVD Singular Value Decomposition.

TCO Transparent Conductive Oxide.

TMAH tetramethylammonium hydroxide.

WDM Wavelength Division Multiplexing.

Chapter 1

Introduction

Classical software programming and algorithms have demonstrated a robust, reliable, and efficient approach to solving problems that can be relatively easily described through analytical methods. In recent years, the rapid growth and advancement in high-speed broadband telecommunication architectures have realized a dependable data-stream infrastructure to carry and transmit enormous volumes of data from an ever-increasing number of interconnected devices and sensors. Inundated by the large volume of datasets, classical sorting and filtering techniques are no longer sufficient to provide accurate, timely, and nuanced data analysis. To address this data challenge, artificial intelligence (AI) and machine learning (ML) systems have demonstrated remarkable performance in pattern recognition, classification tasks, and trendline predictions on abstract datasets without prior explicit programming [1]. Machine learning accelerated programs have driven innovation in areas such as healthcare diagnosis and drug discovery, to autonomous vehicles and robotics and has also provided unique insight in semiconductor manufacturing methods to minimize and predict unwanted fabrication non-idealities. The most widely deployed ML

methods are supervised learning methods where a classifier algorithm is tuned on a set of labelled training data which maps the correct output y for a given input x (or a probability distribution function $f(x)$ for given x). Specifically, deep neural networks (DNN) have proven to be an efficient classifier algorithm for supervised learning. By mimicking the structural organization of interconnected neurons within a biological brain, the multilayered networks of summation and threshold units of DNNs generate an input output mapping. The correctness of outputs is determined by minimizing the generated output errors by using gradient decent optimization routines to tune the internal weighting parameters of the connected layered network [2]. Applications in computer vision and image detection have gravitated towards convolutional feature extraction which is highly compatible for matrix array data format [3]. Although, modern parallel computing solutions have made it possible to support DNN models that contain billions of parameters, the energy and computational performance scaling towards complex applications of the future is not viable.

The main driving factor behind the exponential growth and advancements in ML can be attributed to improvements in computational performance in generalized computing units such as central processing units (CPUs) and specialized hardware accelerators such as graphics processing units (GPUs) and tensor processing units (TPUs). Computational requirements for the training and deployment of DNNs in recent years (since 2012) have shown an exponential increase following a 3.4 month doubling trendline; however, in comparison integrated circuits have only improved following Moore's law of doubling every 18 months [4, 5]. As classification and inference task become furthermore sophisticated, for example demonstrated by AlphaGO,

the compute requirements of DNNs will surpass the electronic scaling of Moore’s law. Indeed, scaling performances for integrated circuits have already deviated away from Moore’s law, although physical transistor dimension continue to shrink. Channel leakage currents and considerable power dissipation in the form of heat impose strict design limitations on higher clock-rate frequencies and the number of logic cores [6–8]. Responsible for a proportionally large fraction of on-chip energy dissipation, repeated charging and discharging of interconnect wiring capacitance and resistance for every bit of information communicated, leads to wasteful energy consumption on the order of picojoules per bit [9]. The distributed and largely parallel nature of DNN hardware acceleration platforms will be configured with design architectures that only exacerbates the high energy dissipation issue.

Considering the underlying physics of optics and photonics, analog computing in the optical domain offers several promising performance advantages over conventional CMOS (complementary metal oxide semiconductor) electronics. Confined electromagnetic waves propagating within photonic waveguides or optical fibers do not encounter a capacitive nor resistive load; therefore, time limiting charging properties and energy dissipation through joule heating is non-existent. Unhindered by electronic RC time delay and or electron/hole mobility through charge carrying wires, photonics presents a platform for large bandwidth and low latency interconnects. Signal attenuation is present due to waveguide propagation losses from routing geometries, intrinsic material absorption, and scattering from sidewall roughness; however, significant progress in material and fabrication optimization have resulted in losses suppressed beyond $1dB/cm$ [10, 11]. Following the advancements in pursuing next-generation telecommunications infrastructure, integrated photonics components

have delivered modulators up to $100GHz$ [12] and photodetectors exceeding $200GHz$ [13] in performance which provide superior speed and bandwidth opportunities compared to electronic counterparts. Information transmission capacities can be further expanded by leveraging wavelength division multiplexing (WDM) and spatial mode division multiplexing (SDM) encoding techniques. Current optical computing demonstrations, either on photonic integrated silicon circuits or with free space diffractive optics and spatial light modulators, rely on volatile actuation mechanisms to switch, reconfigure, and route optical signals according to predefined weighting values of a trained neural network. Although arithmetic operation on the data stream leverages the advantages offered in the optical domain, programming of the overall network requires repeated addressing within the electrical domain which is still constrained by physical limitations. The transfer of data between arithmetic logic units and memory units is known as the Von-Neumann computing bottleneck that is highly undesirable for large scale data-driven neural networks. Chalcogenide phase-change material alloys present an attractive platform to surpass the Von-Neumann bottleneck and realize a power efficient reconfigurable in-memory optical computing architecture for the acceleration of neural networks. Comprised of group 16 elements (sulfur, selenium, and tellurium), phase-change chalcogenide compounds can achieve a wide range of unique optical properties spanning across ultraviolet-visible and into the mid-infrared spectrum. With a high-throughput combinatorial deposition technique, several material compositions such as Ge-Sb-Te, Sb-S, and Sb-Se, have been discovered to exhibit non-volatility and reconfigurability. Such alloy formulations have been the focus of intense research as they are uniquely adaptable for photonic applications because of favourable properties such as near-infrared transparency and

high refractive index contrasts between two distinct material phases: amorphous and crystalline. Integration of phase-change materials (PCMs) with metasurfaces/metamaterials and integrated photonic circuits presents scalability opportunities on two fronts: improved energy efficiencies, and reduction in physical footprint. Optical in-memory computing with PCMs eliminates crossing of domain boundaries and avoid wasteful electro-optic conversion for signal processing.

Chapter 2

Research Objectives

The efforts of this thesis focus on the design and implementation of chalcogenide phase-change material based metasurfaces/metamaterials and thin film inclusion on two optical waveguide platforms consisting of optical fibers and integrated photonic waveguides, to demonstrate reconfigurable non-volatile modulations of signal intensity and phase.

1. Demonstrate optical fiber-tip integrated all-dielectric GST phase change metamaterial with wavelength tunable resonances showing intensity modulation and switchable group delay dispersion (GDD) within the near-infrared telecommunications spectral band.
 - (a) Cuboid unit cell of the GST metamaterial structure is modelled in Lumerical finite difference time domain (FDTD) simulation environment with rounded edges and corners to imitate the smoothing effects of focused ion beam milling fabrication process.
 - (b) extraction of transmission and phase data across amorphous and crystalline phases of GST.

2. Investigate chalcogenide phase change metamaterial integration on silicon nitride photonic waveguides in both resonant and non-resonant regimes.
 - (a) Resonant: design of GST grating structures to couple evanescent waveguide modes to elicit confined resonant modes; thereby, generating spectral resonances at specified center frequencies.
 - i. Modelling of GST meta-grating on silicon nitride waveguide in Lumerical FDTD for the extraction of transmission and phase profiles.
 - (b) Non-resonant: thin film integration of GST material in a stratified configuration to enable the dispersion engineering of waveguide phase-shifter elements within Mach-Zehnder Interferometer (MZI) circuits.
 - i. With ellipsometry measured optical constants of phase change materials such as GST, SbS, and SbSe, the waveguide cross section is simulated, and propagation characteristics extracted for the telecommunication wavelength range ($1300nm - 1600nm$) to create a compact model.

Chapter 3

Literature Review

3.1 Metamaterial and Metasurfaces

Metamaterials are composite materials artificially engineered with unique electromagnetic properties not found in naturally occurring materials. Initially conceived as a paradigm to design novel electromagnetic properties, unachievable through traditional chemical formulations, the metamaterial concept has seen rapid growth in many scientific fields and applications ranging from nonlinear nanophotonics to biomedical assays. The unprecedented electromagnetic phenomena exhibited in metamaterials arise from sub-wavelength periodic and/or non-periodic metamolecule resonators embedded within a host medium of a particular chemical composition. Deliberate micro/nano-structuring of the geometrical resonator design and specific formulation of material stoichiometries aid to elicit extraordinary electromagnetic behaviour because of the engineered effective permittivity and permeability, and by extension the refractive index. Initial terahertz-frequency optical metamaterials were demonstrated with the use of plasmonic metals, such as gold, silver, and aluminum, to enable the engineering of optical wavefronts through the extreme confinement

and localization of light, induced by the resonant excitation of conduction electrons-plasmons. All-dielectric metamaterials based on Mie resonances-creation of electric and magnetic dipoles in dielectrics-provided an alternative mechanism for achieving high confinement of light at subwavelength scales; thus, avoiding the ohmic losses associated with the plasmonic interaction. Well-documented metamaterial behaviours include negative refractive index with implications for invisibility cloaking applications [14, 15], perfect absorption for high efficiency imaging and detection systems [16, 17], and ultra-thin meta-lenses to realize compact and aberration free optical systems [18, 19]. In the past decade, significant research interests have shifted focus to transforming the passive and static nature of classical metamaterials into tunable and adaptive devices—also called metadevices. These metadevices have incorporated functional materials within the subwavelength metamolecule framework to alter their electromagnetic properties in the presence of an external stimuli.

The progression of passive metamaterials into active metadevices serve as foundational building blocks to tackle future challenges in applications such as information transfer, signal processing, sensing, imaging, and display technologies. Active tunability of metamaterial properties can be differentiated into two categories: altering of physical geometry of the subwavelength resonators or modulating the permittivity/permeability of the surrounding media through the incorporation of a functional material. Geometrical alterations of the resonant structure can be further subdivided into two approaches: by redefining near-field interaction between adjacent periodic resonators or by changing the shape and dimensions of individual resonators itself. These approaches were one of the initially demonstrated solutions of achieving reconfigurability in plasmonic and dielectric metamaterials. The ubiquitous split ring

metamolecule have been fabricated on deformable membranes [20], thermal [21] and magnetically driven nanowires [22], and electro-static platforms [23], to illustrate resonate frequency tunability through physical displacement. Modulation of the inherent electromagnetic properties of the surrounding media have also been proven as an equally effective method of changing resonant conditions in both plasmonic hybrid and all-dielectric metamaterials. Such examples include the thermo-optic effect, free carrier plasma dispersion, microelectromechanical actuation, and phase transition materials with markedly different refractive indices between two distinct material states (vanadium dioxide, gallium, and liquid crystals) [24–27]. One significant drawback underpinning these approaches lie in the inherent volatility associated with the switching mechanisms. The constant energy requirement for operation limits the widespread adoption and scalability of such devices for use in large scale compound optical systems.

3.2 Chalcogenide Phase Change Materials

The rapid adoption of artificial intelligence and machine learning in various industries has resulted in an increasing need for better computing, data storage, and telecommunication hardware. With each progressive generation of telecommunication networks that expand on bandwidth, data rates, and reduced latencies, data generated by interconnected smart devices such as autonomous vehicles, environmental sensors, and smartphones will require efficient data processing with minimal energy consumption. Reconfigurable and programmable photonic devices are poised to meet these data processing demands; however, current actuation mechanisms are a volatile process—requiring constant energy input to enable reconfigurable proper-

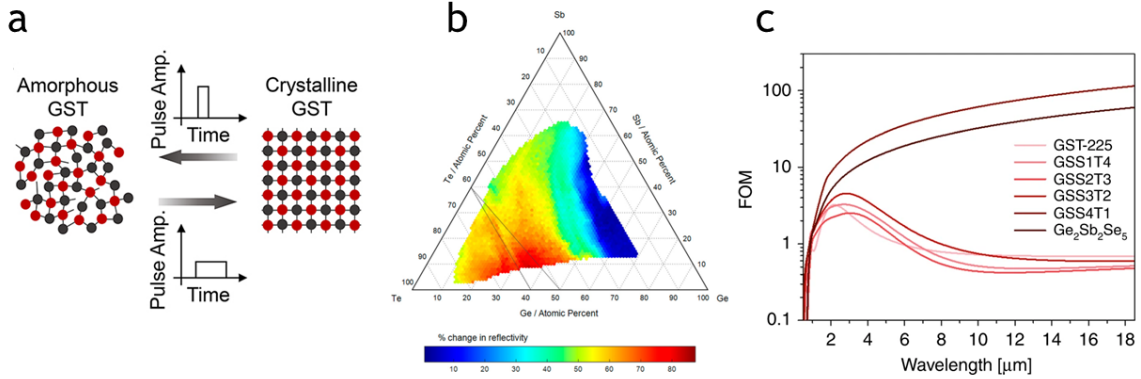


Figure 3.1: Properties of GST-based phase change materials. a.) schematic illustration of the reversible switching between amorphous and crystalline material phases with different pulsing protocols. b.) the stoichiometric dependent change in reflectivity across amorphous/crystalline phases within the ternary composition. c.) figure of merit for various germanium based PCM alloys.

ties. Chalcogenide phase-change materials offer a non-volatile switching mechanism to address this energy concern. The ramifications of the non-volatile property of phase-change materials are two-fold: low energy consumption for large scale optical systems, and distinct memory functionality where the material phase can be encoded with digital information.

Chalcogenide phase change materials are a type of material allow that exhibit changes in atomic structure from a crystalline to an amorphous state, or in reverse (as shown in Figure 3.1), in response to an external stimulus in the form of electrical, thermal, or optical energy [28]. The rearrangement of the material’s atomic structure translates to significant changes in the materials electronic (resistivity) and optical (transparency) properties. Without the need for an external energy supply to sustain the material in a particular atomic structure, chalcogenide PCMs have been a key-component in data storage applications in optical media such as CDs and DVDs

and in electronic memory, for example phase change randomly addressable memory (PCRAM). Specifically, laser rewritable optical storage medium of CDs and DVDs employed the ternary alloy of germanium (Ge) antimony (Sb) telluride (Te), pioneered by researchers at Panasonic, demonstrated remarkably fast switching speeds ($< 50ns$) and observed phase change cycling beyond 10^5 times [29]. However, reconfigurable photonic devices targeting optical switching and signal modulation require PCM compositions to offer fast phase change dynamics, low threshold switching, large switching endurance, thermal stability in the amorphous phase and large optical/electrical contrast between the two phases [30, 31]. Quantitatively, a figure of merit (FOM) describing the change in refractive index (Δn) that is proportional to the change in the materials extinction coefficient ($\Delta\kappa$) is an efficient value to correlate between the different classes of photonic devices. The figure of merit is defined as:

$$FOM = \frac{\Delta n}{\Delta\kappa} \quad (3.1)$$

Figure 3.1c demonstrate a widely varying range of FOM achievable across different PCM alloy compositions, which suggests that the traditional GST-225 formulation might not be the optimum stoichiometry for all photonic applications. High throughput combinatorial deposition of ternary chalcogenide alloys has been demonstrated to be an efficient method to identify ideal material properties in a rapid process. For example, Guerin *et al.* presented a combinatorial synthesis of the GeSbTe alloy through a simultaneous and controlled co-deposition of the atomic elements on a substrate through evaporation to yield a compositional gradient thin film. For any given sample position, the alloy composition is the normalized sum of the con-

stituent elements that were co-deposited. The authors found optical reflectivity contrast between amorphous and crystalline phases was maximized for antimony poor compositions, measuring at 85% with the commercially explored alloy of GST-225 exhibiting a contrast of 56.7% in comparison. Moving along the Sb_2Te_3 — GeTe tie line compositions of GeSb_4Te_7 , GeSb_2Te_4 , and Ge_4SbTe_5 demonstrate an increase in the optical contrast (panel b of Figure 3.1) [32].

Actuating a phase change event requires the application of external thermal, electrical or optical energy. Transitioning from a crystalline phase to the amorphous phase constitutes the delivery of energy to heat the phase change material above its threshold melting temperature, causing atomic vibrations to disrupt the long-range crystal lattice arrangement into a disordered amorphous structure. Once the external energy supply is discontinued, the material is allowed to rapidly cool. Typically, the cooling rate of $1^\circ\text{C}/\text{ns}$ is required of GST-based phase change materials [33]. This amorphization process is known as a melt-quench process. Conversely, by applying a long and moderate energy pulse to amorphous PCM, the material heats up to the glass transition temperature where atoms rearrange to form a crystalline lattice. This is known as crystallization and generally involves two events: nucleation of small crystalline domains and the subsequent growth of such domains to expand throughout the rest of the material. The nucleation process is primarily governed by the thermodynamics of phase change process, while crystal growth is dominated by the kinetics of atomic motion. Crystallization processes at low temperatures close to the glass transition temperature is slow because the atomic mobility is small; therefore, fast crystallization processes occur at elevated temperatures such as 300°C for GST. Furthermore, it is important to distinguish crystallization speeds between as-

deposited amorphous PCM and melt-quenched PCM is not the same. PCM with prior phase change cycling posses subcritical crystalline domains (sparse framework of crystal lattice) so the slow nucleation process can be bypassed [28].

3.3 Chalcogenide Phase Change Metamaterials

The incorporation of chalcogenide phase change materials brought dynamic control over the polarization, intensity, and phase of optical wavefronts which have facilitated a wide range of active tunable nanophotonic metamaterial demonstrations that exhibit unique functionalities in a miniaturized footprint compared to traditional optical approaches. Most importantly, the inclusion of phase change materials provide a switching mechanism that avoids any physical geometric alterations to the underlying nanostructure. Early demonstrations show that the optical response of plasmonic metamaterials, which strongly depend on the near-field interaction between the metallic structures and the surrounding dielectric environment, can be modulated with the addition of a functional layer such as chalcogenide alloys. Gholipour *et al.* presents a planar array of asymmetric split rings on a 50nm thick gold film that supports trapped mode plasmonic excitation targeting operation in the near to mid infrared spectrum [34]. A laser induced phase transition in the adjacent GST-225 material presents an optically controlled hysteresis response between the amorphous and crystalline phases. The associated refractive index increases for a GST phase transition from amorphous to crystalline phase, resulting in a red shifted response by around 200nm. With a unit cell size of 400nm, targeting operation in the telecom range, a transmission contrast of 2.5dB was observed. Larger unit cells of 900nm for mid-infrared operation ($4 - 8\mu m$) generated a contrast of 4dB since the extinction

coefficient of GST is reduced.

At optical frequencies, the near-field propagation of surface plasmon polaritons in metallic elements encounter substantial ohmic losses which limit their applications in low loss optical components. Highly confined Mie resonant based all-dielectric metamaterials present an opportunity to avoid such losses and utilize the phase change layer as the resonant structure itself. Authors Karvounis *et al.* demonstrated near-infrared transmission and reflection resonances in 300nm GST film deposited on a quartz substrate [35]. The metasurface pattern consisted of nano-grating arrays with subwavelength periods ranging between 750nm and 950nm corresponding to resonances within the spectral ranges of 1100nm-1700nm. The relatively high refractive indices of GST in amorphous ($n_{am} \approx 3.1$) and crystalline ($n_{cr} \approx 6.2$) phases generate high quality spectral transmission/reflection resonances due to a strong confinement of the incident light. Under illumination from a grating aligned polarization (TE), the physical dimensions of the structured GST layer exhibit a combination of thin film interaction and longitudinal grating modes. Phase switching the GST layer from amorphous to crystalline results in a spectral red-shift by 150nm which is sufficient to produce a transmission contrast of -4dB. Indeed, without nanostructuring photonic components such as reconfigurable metasurfaces and Fresnel zone plates can be dynamically written on a GST thin film canvas as the large refractive index contrast between amorphous and crystalline is sufficient to hold dielectric resonances as demonstrated by Wang *et al.* [36].

Apart from intensity modulation, the incorporation of phase change material in metamaterial demonstrations has also inspired the design and characterization of reconfigurable varifocal metalenses. Authors Qin *et al.* presented the inclusion of

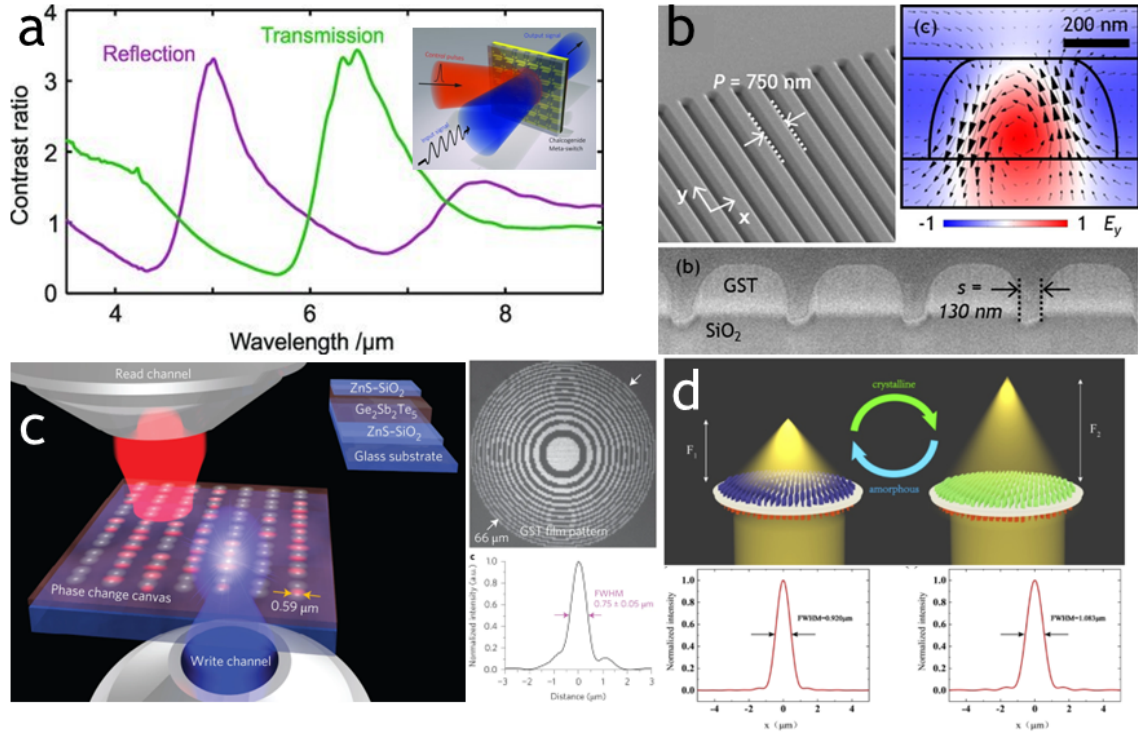


Figure 3.2: Various metamaterial demonstrations with inclusion of chalcogenide phase change material. a.) asymmetric plasmonic split ring resonator modulated with adjacent GST thin film. b.) excitation of longitudinal resonant modes within subwavelength nanostructured GST gratings. c.) patterning of Frensel lenses in a GST substrate through direct laser amorphization/crystallization. d.) meta-lens with tunable focal lengths between amorphous and crystalline phases.

phase change material Sb₂S₃ as a functional layer to implement a reconfigurable meta-lens with two distinct focal lengths that can achieve a full width half max (FWHM) diffraction limited focal point [37]. Targeting operation centered at a wavelength of 1310nm, Sb₂S₃ was the phase change chalcogenide material of choice due to the combination of a refractive index contrast of 0.6 and a negligible extinction coefficient across both amorphous and crystalline states. The meta-lens consisted of two vertically stacked array of silicon and Sb₂S₃ nanofins separated by a silicon dioxide

layer. Engineering of the phase distribution of the two layers with the Pancharatnam - Berry phase method, produced a phase shift difference corresponding to a π radian and 2π radian for the amorphous and crystalline phase respectively. Such a design permitted the metalens to toggle resulted in focal lengths of $15\mu m$ and $20\mu m$. Numerical simulation with FDTD resulted in focal lengths of $15.41\mu m$ and $20.38\mu m$ with numerical aperture values that indicated near diffraction limited performance.

3.4 Optical Fiber Integrated Metamaterials

Despite the technological process and the ubiquitous use of optical fibers, conventionally, they have been limited to serve as connection links between individual network nodes. Although fiber-based devices as such as fiber Bragg gratings and erbium doped fiber amplifiers demonstrate the possibility of functionalizing the traditionally passive light guiding structure, advanced operations such as signal generation, processing, and computation are mostly confined to electronic integrated circuits. The electro-optic signal conversion required for such an arrangement present an energy intensive, bandwidth and data rate limited bottleneck. Recently, in planar free-space configurations, metamaterials and metasurface made from various metal, dielectric and semiconductor materials including reconfigurable chalcogenide phase change materials have shown great promise towards the realization of phase, amplitude and polarization control of the incident light through enhanced light-matter interactions. A wide range of functionalities have been demonstrated including beam steering, aberration free focusing, polarization control and holography—all at a fraction of the operating wavelength in size [38–45]. Enabled by advancements in nanofabrication and lithography techniques, the integration of metamaterial/metasurfaces on

optical fibers allude to the possibility of an all-optical signal carrying and processing platform. Fiberized metasurface examples include beam focusing, beam steering and deflection, and logic operations.

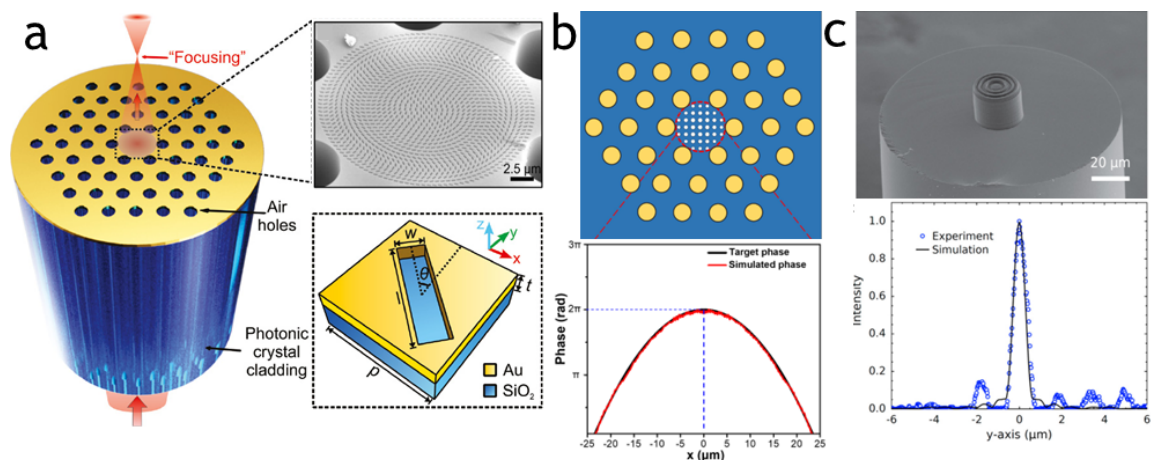


Figure 3.3: Optical fiber integrated meta-lens demonstrations. a.) phase-gradient plasmonic metasurface on a photonic crystal fiber. b.) all-dielectric TiO_2 based meta-lens integration with focusing efficiencies of 70%. c.) inverse designed meta-lens fabricated with two-photon absorption 3D printing technique.

Mode conversion between optical fiber and subsequent free space optics or integrated photonic platforms require precise mechanical alignment and bulky optical components to match the highly divergent output beam. Fiber integrated meta-lens devices offer polarization conversion and beam forming capabilities in an ultra-compact footprint. In 2019, Yang *et al.* experimentally demonstrated an ultra thin geometric phase based metasurface lens on the end facet of a photonic crystal fiber with a maximum enhanced optical intensity as large as 234% [46]. The radially distributed array of rectangular slots patterned on a 40nm thick gold film with varying rotational angles between 0 and 164deg constructed the full 2π hyperbolic phase profile as depicted in panel a of Figure 3.3. The large core diameter of a photonic

crystal fiber ($25\mu m$) compared to that of a single mode fiber ($8\mu m$) provided a larger fabrication area to define the phase profile required to achieve efficient focusing functionality. Two patterns corresponding to focal lengths of $30\mu m$ and $40\mu m$ targeting a center wavelength of 1550nm had respective numerical apertures of 0.37 and 0.28 . The polarization conversion efficiency (from right hand to left hand circularly polarized light) was 16.4% due to plasmonic losses of the metallic metalens design. Authors Zhao *et al.* investigated two alternative design changes to increase conversion efficiencies: increased fiber core diameter and the use of an all – dielectric material design [47]. Panel b of Figure 3.3 show the larger core diameter ($50\mu m$) offered support for more unit cells with higher resolution to tune the required phase profile and allow for longer focal lengths to be designed. To increase the modal diameter of the photonic crystal fiber while constrained to single mode operation, the air-holes are filled with fluorine doped glass rods; thus, decreasing the refractive index contrast between core and cladding. Leveraging the same geometric phase design approach, varying diameters of TiO_2 nanopillars achieved the full 2π profile for three separate communication windows stretching from 800nm to 1550nm . The in-fiber metalens showed a focusing efficiency of 70% at a focal length of $300\mu m$. Accomplished through a 3D direct laser writing technique, authors Hadibrata *et al.*, demonstrated the practicality of a fiber integrated metalens approach to transform the parallel wavefront into a spherical wavefront at the near-infrared range within a compact package [48]. A computational inverse design based on FDTD was used to explore and optimize the permittivity distribution of the optical material within a bounded 2D region. The optimized design represented a two-dimensional lens and to generate a full 3D lens, rotational symmetry was applied to produce concentric rings

with a shape like Fresnel lenses. The optimized lens design was fabricated on the tip of a single mode optical fiber, shown in panel c of Figure 3.3, with a commercial system (Nanoscribe) through a process known as two-photon polymerization. The single mode fiber is immersed in the IP-Dip photoresist and the metalen design was printed layer by layer with a femtosecond laser at an exposure wavelength of 780nm. The performance of the fiber tip integrated metalens was evaluated within an experimental two photon polymerization setup as an alternative objective for direct patterning. The smallest linewidth obtainable was 220nm which was 70nm smaller than what is achieved with the commercial platform.

As the demand for an expanded bandwidth and faster data transmission speeds of optical fiber communication networks continue to increase, modern networks have deployed advanced modulation techniques to allow for more efficient use of the available frequency spectrum. One such modulation scheme is known as polarization-division-multiplexing (PDM), where data channels are separated based on the polarization property of light. Conventionally, network nodes that utilize such a modulation protocol will need to distinguish and select between a mix of polarization modes into TE and TM channels. This is often performed by a mode converter component which has a significant footprint and can be complex to fabricate. Here, authors Zhou *et al.*, demonstrate a fiber integrated all - dielectric metasurface which facilitates polarization-controlled beam manipulation to separate between TE and TM polarization [49]. Two separate phase profiles corresponding to each polarization is solved for the same coordinates such that the resulting silicon nano-brick metasurface will produce a vortex beam for TE-polarized light and a collimated beam for TM-polarized light. Within the context of optical interconnect applications, the authors

demonstrate the practicality of this device as a polarization selective switch where a transmission contrast of 15dB is achieved between TE and TM polarized light. Instead of mitigating the ohmic losses associated with plasmonic based resonant metamaterials, the fiber integrated all optical signal modulation presented by Xomalis *et al.* show controllable coherent absorption to demonstrate proof-of-principle logic functions such as XOR, NOT and AND operations within the telecommunication band between 1530nm and 1565nm [50]. The planar metasurface absorber consists of a 70nm thick gold film patterned with an array of asymmetrically split ring apertures within a $25\mu m$ square area centered on a polarization maintaining single mode fiber core. The alignment of the metasurface is oriented along the slow axis of the fiber such that the split ring symmetry is aligned. An optical fiber-based interferometer setup was realized to produce coherent interaction of light. A standing wave resulted from the interaction of two opposite propagating continuous light signals, resulting in destructive (nodes) and constructive (anti - nodes) interference. When the metasurface absorber is positioned at such nodes and anti-nodes, the output signal intensity can be controlled from 9% to 57% corresponding to coherent absorption and transparency respectively. Modulated on a 10kHz frequency, logical ones and zeros represented by high and low intensities pass through the fiber integrated metasurface absorber system and exhibit XOR output through a combination of coherent absorption and transparency. Through the application of an external phase shift between the supplied input signals, other logic operations such as NOT, OR, and AND can be demonstrated.

3.5 Optical Acceleration of ANNs

The potential of machine learning (ML) algorithms in recent years have proven to revolutionize many different disciplines ranging from education, healthcare, finance, to supply chain logistics and engineering design. At its core, machine learning is a pattern recognition algorithm that can distinguish hidden correlations between different data elements to generate new perspectives that was not predefined. The ability of ML programs to learn and describe a collection of datasets with a series of fundamental guiding principles can be applied to many applications that are otherwise resource intensive or impracticable to manually anticipate as no analytical form exist to model the problem. Owing to its flexibility and scalability, the neural network (NN) approach (schematic depicted in Figure 3.4) has dramatically improved the state of the art in speech recognition, visual object detection, high throughput drug discovery and genetic sequencing.

Facilitating the learned mapping between desired output y or $f(x)$ to a set of inputs x , NN are trained on a predefined dataset in a process known as supervised learning. Specifically, the procedure is called stochastic gradient decent (SGD) where gradient-based optimization routines are used to adjust parameters throughout a multilayered network of threshold units to minimize the output error difference between the desired output for the respective input dataset. Optimizing these network parameters in recent years for larger datasets, added complexity and additional layer densities of NN have constituted an enormous demand for computational power and performance in terms of operations per second, latency, and power consumption. The amount of computing resources required for training and inference calculations of

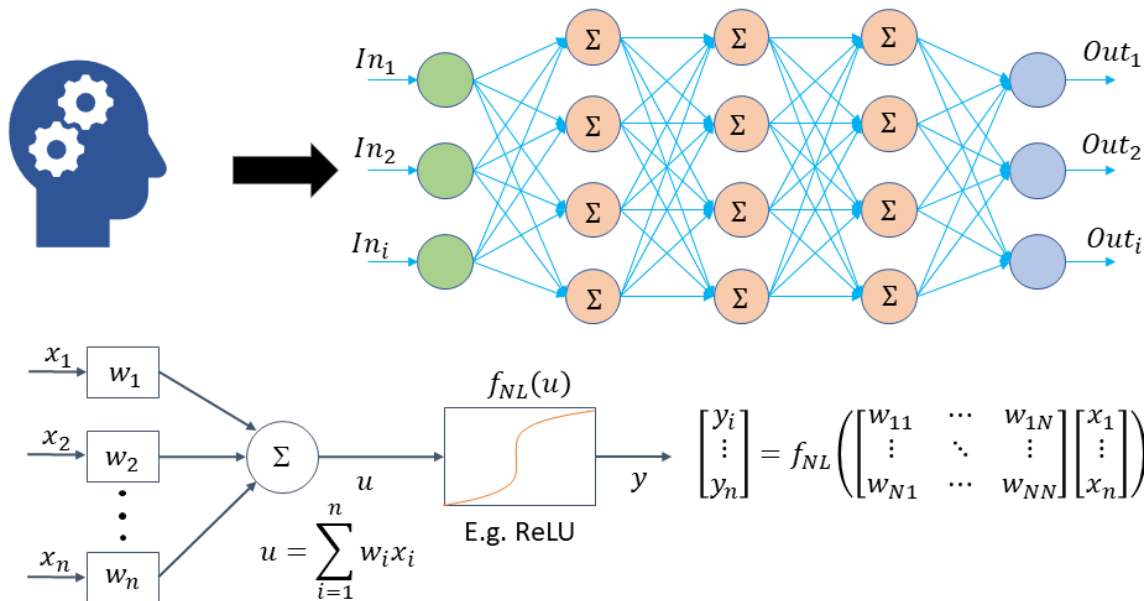


Figure 3.4: Hierarchical overview of a fully connected neural network: neurological connections of a biological brain is represented within a DNN as input and output layers separated by interconnected hidden layers performing weighted summation operations with a non-linear threshold activation which can be represented as matrix vector multiplications.

state-of-the-art NNs has followed an exponential increase with a 3.4 doubling rate [4]. In comparison, following Moore’s law computational performance doubled every 18 months. Progress in NNs algorithms has continued as hardware acceleration moved away from CPUs and towards dedicated designs or application specific integrated circuits (ASICs) such as GPUs and TPUs. However, physical limitations underpinning digital electronics still exist due to inherent losses in metallic interconnects and unavoidable RC time constants which constrain faster clock cycles and wider bandwidth. Therefore, a design paradigm shift towards computation in the optical domain should be considered as a viable alternative as the use of photons allow large bandwidth operation, light speed propagation latency, and near zero interconnect

power consumption.

Silicon photonic integrated circuits (PICs) demonstrate an adaptable and scalable platform to implement next generation hardware accelerators for NNs. PICs have proliferated in many technologically significant domains including data communications, sensing, and emerging applications such as light detection and ranging (LiDAR). The rapid adoption of silicon photonics has been enabled by the mature fabrication process and manufacturing scalability solutions developed for the complementary metal oxide semiconductor (CMOS) based electronic integrated circuit technology. In contrast to optical fibers, the highly confined optical modes supported by silicon waveguides allow for higher density integrations of both active and passive components directly on the same CMOS silicon wafer. An expansive library of photonic components ranging from direct laser integration, high speed modulators and photodetectors, to efficient couplers, power splitters and high-quality factor resonators enable the creation of signal processing systems in the optical domain [51–62]. Conventionally, silicon photonics transported and routed analogue information which was then converted into electrical signals that are mixed, filtered and processed in the digital domain. Recently, the development of programmable and tunable photonics has enabled signal processing functionalities within the optical domain. Addressable through sophisticated electronic control circuits, dynamic manipulation of the flow of light in cascaded photonic networks has proven that linear functionalities and matrix vector operations can be performed in an efficient analogue format that could accelerate machine learning algorithms such as deep neural networks [63, 64]. Photonic neural network accelerator architectures can be differentiated into two configurations: coherent and incoherent. Both networks' configurations implement

matrix vector multiplication operations by modulating the input signals amplitude and phase as it propagates through the photonic network.

Mach – Zehnder Interferometers (MZI) in silicon photonics have been a widely used component in high-speed optical modulators, encoding and decoding in optical communications, and environmental sensing. The basic concept behind a MZI consists of splitting the incident monochromatic light with a multi-mode interferometer (MMI) or y-branch junction into two equal portions which are then routed into two non – coupled waveguides. As the divided optical signal propagates through the two arms, they experience unequal phase-shift across the two paths. The recombination of the two signals with another MMI or reverse y-branch component facilitates constructive and destructive interference according to the phase-shift value. Alternatively, the MZI can be thought of as a 2×2 analogue optical gate which projects the light from two input waveguides onto two output waveguides as a linear combination. If propagation loss and insertion losses of each constituent elements are negligible, then this corresponds to an unitary matrix transformation first proposed in 1994 by Reck *et al.* [65]. A single MZI, representing a 2×2 unitary transformation matrix, can be expressed as a $SU(2)$ rotation matrix defined as:

$$R(n) = \frac{1}{2} \begin{bmatrix} e^{i\alpha}(e^{i\theta} - 1) & ie^{i\alpha}(e^{i\theta} + 1) \\ ie^{i\beta}(e^{i\theta} + 1) & e^{i\beta}(1 - e^{i\theta}) \end{bmatrix} \quad (3.2)$$

Where θ, α, β represents the single internal and two external phase shifters of the MZI respectively. Any arbitrary $n \times n$ unitary transformation matrices $SU(N)$ can be decomposed into a product series of $SU(2)$ submatrices corresponding to a cascaded MZI mesh network. Furthermore, generalizing to any complex valued matrix M ,

which is not limited to unitary operation, the singular value decomposition method can be used to describe matrix $M = U\Sigma V^t$ where U is an $m \times m$ unitary matrix, Σ is an $m \times n$ rectangular diagonal matrix with non negative real numbers on the diagonal, and V^t is the complex conjugate of the $n \times n$ unitary matrix V .

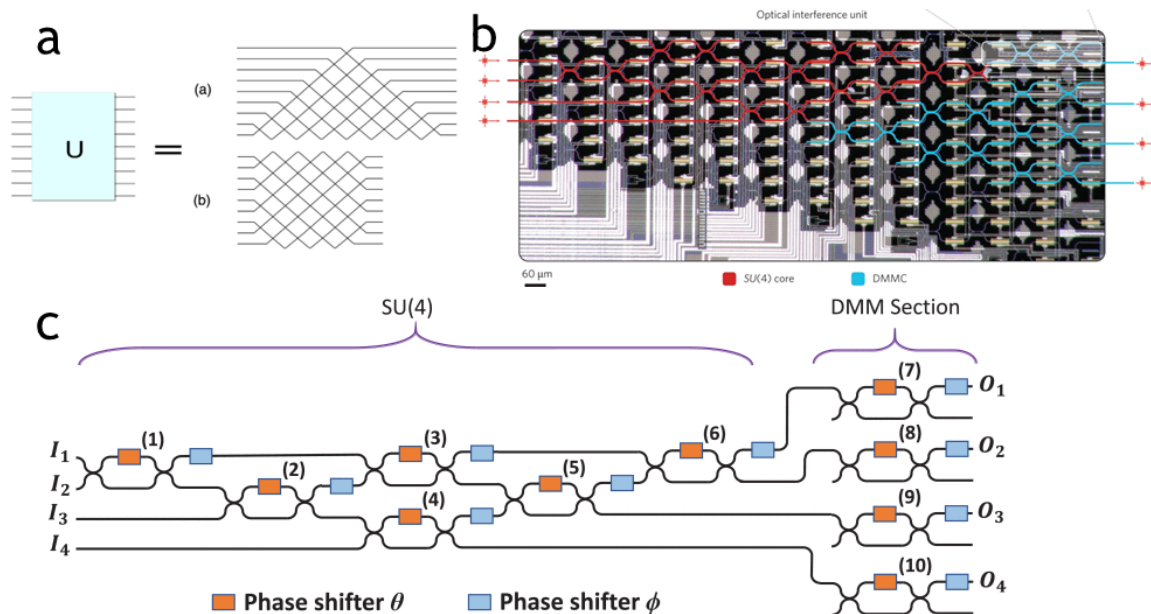


Figure 3.5: Neural network hardware accelerators based on photonic Mach-Zehnder interferometer networks. a.) two MZI configurations to implement an equivalent unitary matrix transformation. b.) optical interference unit fabricated on SOI platform for vowel recognition. c.) programmable linear optical processor based on singular value decomposition.

Such a cascaded programmable MZI mesh network utilizing SVD have been experimentally demonstrated by Shen *et al.* to carry out NN operations for vowel recognition [66]. 360 data points collected from 90 different people pronouncing four different vowels including A, B, C, and D were collected and preprocessed with a standard algorithm. The preprocessed signals are then encoded onto the amplitude

of optical pulses that propagate through the interconnected MZI network. The entire optical network was composed of 56 programmable MZIs where each interferometer is comprised of two thermo-optic phase shifters: one between two 3dB directional couplers (θ) followed by another one (ϕ). The splitting ratio is controlled by the internal phase (θ), while the differential output phase is controlled through the external phase (ϕ). The trained and optimized weighting values of the neural networks were then programmed to such phase shifters throughout the entire network. Vowel recognition evaluated on the MZI network resulted in a 76.7% detection accuracy compared to an accuracy of 91% from a conventional 64-bit digital computer. The difference in performance can be attributed to a limited computational resolution of the optical platform. The authors identified several practical non-idealities, that could impact the computational resolution including thermal cross talk, coupling drift due to fabrication imperfections, finite precision of phase shift values, and optical dynamic range. However, the realization of such an experiment illustrates the feasibility of an optical neural network which in principle can possess order of magnitude improvement in latency and bandwidth compared to single digit GHz clock rate limited electronics. Although commercial foundries offer fabrication services with tuned and optimized recipes, process variations and deviation from ideal geometries introduce undesirable random phase offset within photonic circuits which can contribute to limited computational resolution for neural network inference operations. Therefore, authors Shokraneh *et al.* present an effective calibration scheme prior to programming a photonic MZI mesh network by exploiting properties of an unitary matrix transformation within singular value decomposition [67]. The linear optical processor consisted of 6 MZIs constructing the unitary transformation ma-

trix and 4 additional MZIs to represent the diagonal matrix multiplication section to form an overall linear matrix transformation represented as:

$$[D]_{4 \times 4} = [\Sigma] \cdot [T_{SU(4)}] = \begin{bmatrix} u_{11}^7 & 0 & 0 & 0 \\ 0 & u_{11}^8 & 0 & 0 \\ 0 & 0 & u_{11}^9 & 0 \\ 0 & 0 & 0 & u_{11}^{10} \end{bmatrix} \cdot \begin{bmatrix} U_{11} & U_{12} & U_{13} & U_{14} \\ U_{21} & U_{22} & U_{23} & U_{24} \\ U_{31} & U_{32} & U_{33} & U_{34} \\ U_{41} & U_{42} & U_{43} & U_{44} \end{bmatrix} \quad (3.3)$$

Where U_{kl} $k, l \in 1, 2, 3, 4$ are elements in the unitary matrix $[T_{SU(4)}]$ which is the product of a 2×2 matrix $[D_{MZI}]$ describing the linear transformation of a single MZI stage consisting of an internal (θ) and external (ϕ) phase shifter where $[D_{MZI}]$ is defined as:

$$[D_{MZI}] = j e^{j(\frac{\theta}{2})} \begin{bmatrix} e^{j\phi} \sin(\frac{\theta}{2}) & e^{j\phi} \cos(\frac{\theta}{2}) \\ \cos(\frac{\theta}{2}) & -\sin(\frac{\theta}{2}) \end{bmatrix} \quad (3.4)$$

Optimized weighting values representing a sample neural network correspond to elements in the unitary matrix $[T_{SU(4)}]$. To program the corresponding phase shift values within each MZI segment, $[T_{SU(4)}]$ is successively multiplied by the inverse of $[D_{MZI}]$ such that off diagonal elements in the lower triangle of the resultant matrix becomes zero in a similar method to Gaussian elimination. Here, the programmable MZI network was implemented on a ridge-based SOI waveguide targeting a wavelength of operation of 1310nm. Resistors placed above the optical waveguide layer is utilized as a thermo-optic phase shifter. Characterization of each MZI is carried out by applying the necessary voltage to tune the phase shifters such that each MZI are either in the cross or bar state to serve as a reference. By minimizing the number of

uncharacterized MZI on the path of a single input, the measured output power can be correlated to the applied bias voltage to determine the calibration value required to mitigate fabrication-based phase tolerances. The calibration values are then added to the bias voltages corresponding to the calculated phase shift values to program the overall optical processor.

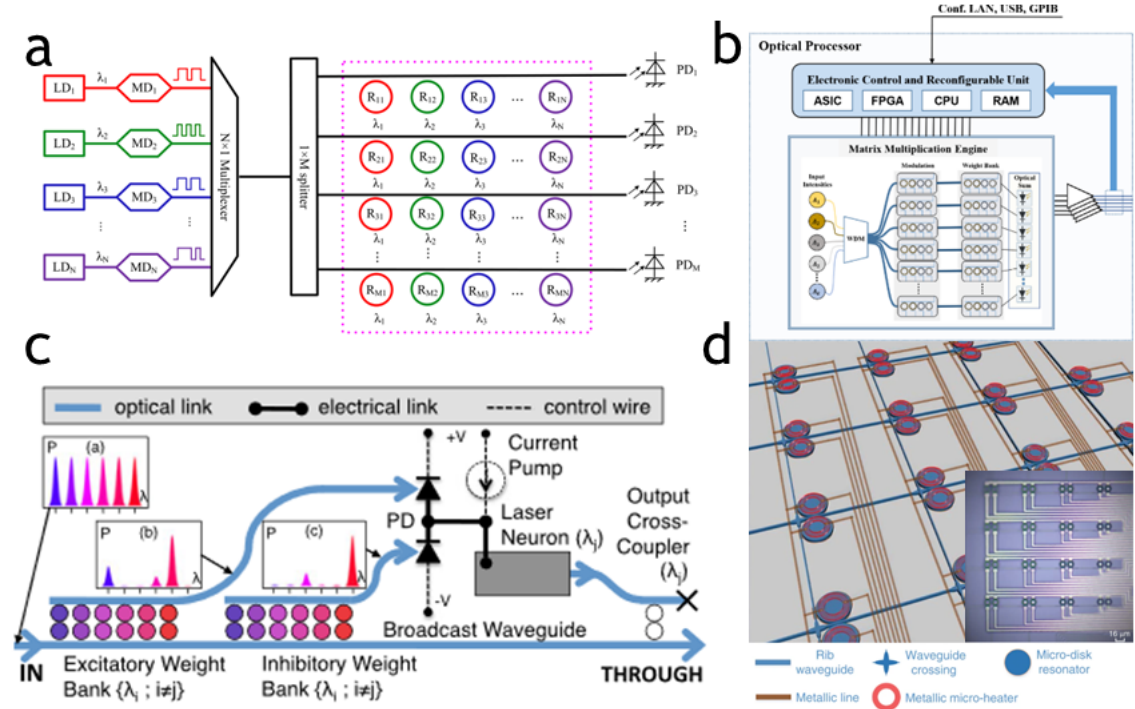


Figure 3.6: Examples of arrayed banks of micro-ring resonators implementing matrix vector operation with wavelength division multiplexing scheme. a.) positive value matrix vector multiplication. b.) matrix computation for massive MIMO communication systems. c.) schematic illustration of "broadcast and weight" scheme. d.) programmable cross-bar arrays of microdisk resonator cavities for signal processing.

Alternatively, matrix multiplication can be directly mapped onto PIC platforms by exploiting one of the degrees of freedom of photonic waveguides such as wavelength, mode, and polarization. Complementary to MZIs, micro-ring resonators (MRRs)

are another foundational photonic building block to realize complex systems. The closed waveguide loop of the MRR permits constructive interference of light leading to the generation of high-quality factor resonances and large intensity buildup. Conditions for constructive interference is satisfied if the MRR circumference is equal to integer multiples of select wavelengths. The sharp resonant profiles of MRRs have found widespread use for communications filtering and high sensitivity sensing but more recently demonstrations of matrix vector multiplication have been proven to be realizable by leveraging the wavelength-division-multiplexing encoding scheme. Assuming an input with multiple wavelength channels, an array of reconfigurable MRRs can be utilized to independently configure the transmission coefficient of each wavelength channel; thus, performing a weighting operation. This can be described by the following matrix relation:

$$\begin{bmatrix} y_1 \\ \vdots \\ y_N \end{bmatrix} = \begin{bmatrix} w_{11} & \cdots & w_{1N} \\ \vdots & \ddots & \vdots \\ w_{N1} & \cdots & w_{NN} \end{bmatrix} \begin{bmatrix} \lambda_1 \\ \vdots \\ \lambda_N \end{bmatrix} \quad (3.5)$$

Where each output element y can be summarized as: $y_i = \sum_{j=1}^N w_{ij}\lambda_j$. The weighted combination of wavelengths does not mix or interfere with each other and propagate down a common output waveguide which is then received by a photodetector that performs the summation of the total optical power. Early implementations of a WDM based scheme for matrix vector multiplication was demonstrated by Yang *et al.* in 2012 [68]. The optical signal processor consisted of a 4 x 4 array of micro-ring PIN diode modulators acting on four equally spaced wavelength channels fabricated on a commercial SOI platform. Current injection into the PIN diode region resulted

in a change in the refractive index of the silicon waveguide, causing a blue shift (shifting to shorter wavelengths) in the resonance spectra under forward bias. The wavelengths were generated from a tunable laser, multiplexed onto a single input bus waveguide, and split evenly among the rows of the micro-ring array. Simultaneous amplitude modulation of the input wavelength and through port transmission modulation of the micro-ring modulators encoded the corresponding elements of the vector array. Photodetectors at the output translated the total output optical power to a corresponding voltage value which represented the matrix multiplication operation. Afterwards, authors Tait *et al.* generalized such a WDM scheme and describe a hierarchical system architecture called “broadcast and weight” [69]. Inspired by neuromorphic computing principles mimicking the neural processing of a human brain, the broadcast and weight protocol describes signals from multiple sources are collected, weighted, and summed to reach an activation threshold before a new output signal is generated. At every input of a photonic node, two series of wavelength filter banks (micro-ring resonators) represent an excitatory and inhibitory weighting profiles. Corresponding photodetectors, outputting a current that represents total optical power, are configured in a balanced format to generate both positive and negative weighting values similar to synaptic connections of biological neurons. The output current of the photodetector can then act as a control pump signal for the excitation of a laser component which will generate a proportional signal broadcasting to subsequent layers within the network.

Indeed, current technology schemes for application specific hardware acceleration of machine learning or neural network training and inference calculations, such as dedicated GPUs and TPUs, have delivered sufficient performance for the deployment

of advanced multilayered networks; however, as the progression of neural networks move towards a higher degree of dimensionality and need for greater programmability, an increase in computation and data movement is required. Scaling and expanding capabilities of future neural networks to encompass both visual and audio-based inference increases the amount of data generated and large datasets require a proportionally large number of weighting values to be read and written to in memory. Not only are the sequence of arithmetic operations limited by the slow clock frequency in electronics, but it has been shown that data movement is more energy costly than computation itself [7]. Both optical hardware accelerator architectures, either SVD MZI mesh or WDM MRR arrays, are not exempt from this data movement constraint. In either configuration, volatile actuation mechanisms are used to change the refractive index of photonic waveguide elements to implement phase shifters or amplitude modulators in MZIs and MRRs respectively. During training and inference operations, phase shift or amplitude based weighting values will need to be reconfigured and programmed by applied bias voltages that are stored on external memory modules. The integration of non-volatile chalcogenide phase-change materials on integrated photonic platforms would bring in-memory computing capabilities to the optical domain and avoid the energy inefficiencies of the Von-Neumann bottleneck. The memristive properties of PCMs would help realize inference weighting elements with sufficient longevity and retention functionalities.

Early demonstrations of phase change material integration onto photonic integrated circuits were presented by Rios *et al.* in 2014 as a viable method to realize a photonic memory element [70]. Owing to its large refractive index contrast across the near-infrared telecommunication wavelength ranges, phase change mate-

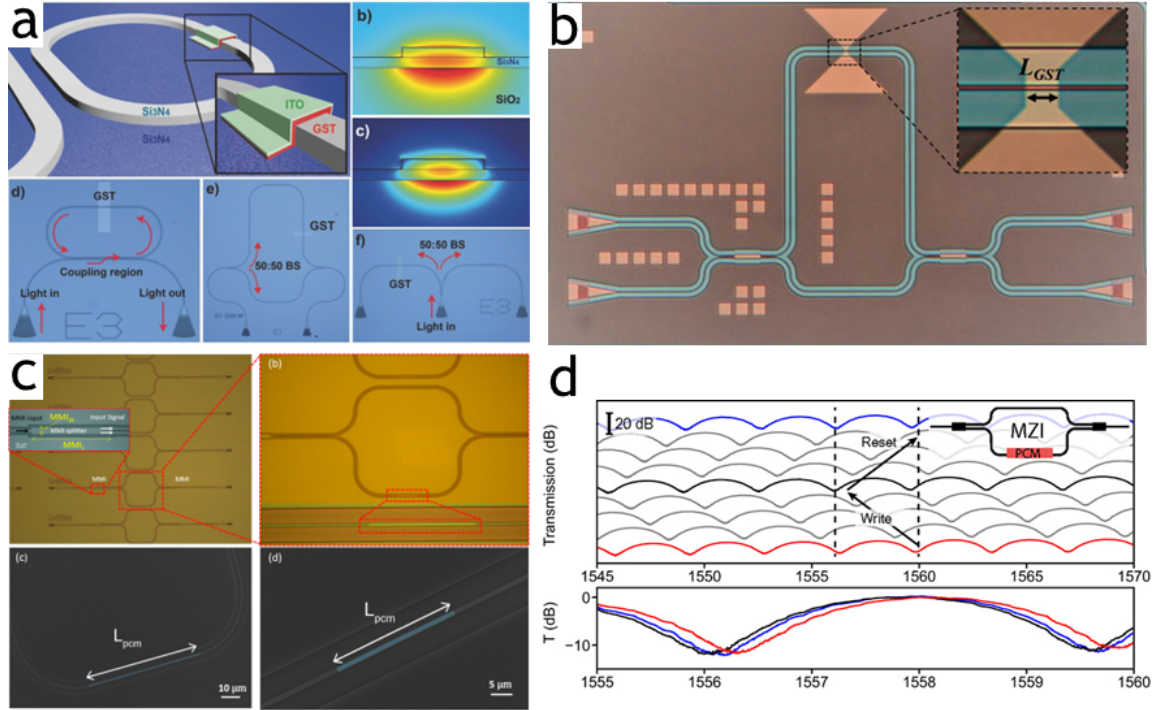


Figure 3.7: Chalcogenide phase change material integration with MZI circuits. a.) GST patch on silicon nitride rib waveguide platform. b.) single arm GST actuation in an unbalanced MZI. c.) addition of low loss Sb₂S₃ PCM on MZI for reduced insertion losses. d.) dynamic control and reconfigurability of a shifted MZI spectra hybridized with Sb₂Se₃ material.

rial GST-225 was deposited on silicon nitride MZIs to modulate the relative phase difference across the amorphous and crystalline material phases. Balanced beam splitters divided the input optical signal between two waveguides with a path length difference of $200\mu\text{m}$. A series of varying GST patch lengths ranging from 500nm to $20\mu\text{m}$ with a constant thickness of 10nm were deposited on the longer arm of the MZI and the overall transmission spectra were characterized. By crystallizing the as-deposited amorphous phase GST thin film with a hotplate, the interference spectrum red-shifted to obtain a π phase shift with a GST length of $10\mu\text{m}$. The state of

operation was preserved without the supply of any additional external power; thus, demonstrating optical memory functionality. A similar demonstration was shown by Zhang *et al.* for the integration of GST on a SOI platform; however, the silicon ridge-waveguide carried a different propagating mode resulting in a spectral shift with different GST patch dimensions [71]. For a path length difference of $400\mu m$, a 20nm thick GST layer was deposited on the long arm with lengths ranging from 300nm to $7\mu m$. With such a configuration, a maximum π phase shift was achieved for a GST length of around $4\mu m$ which is a dramatic reduction in footprint. A phase transition associated with crystallizing GST also results in an increase in the materials extinction coefficient resulting in higher losses and contributing to lower extinction ratios for a MZI device. Therefore, Faneca *et al.* have explored alternative low loss phase-change materials such as Sb₂S₃ and Sb₂Se₃ to improve insertion loss and extinction ratio values [72]. Measured insertion losses for SbS and SbSe cladded waveguides produced $0.04\text{dB}/\mu m$ and $0.09\text{dB}/\mu m$, respectively. Although inherent material losses are lower in both amorphous and crystalline phases for both materials, this comes at the expense of a diminished refractive index contrast. A lower refractive index contrast is compensated for a longer PCM patch length to achieve the full π phase shift. For example, in another demonstration, authors Delaney *et al.* show a π phase shift for every $25\mu m$ long patch of SbSe [73].

Furthermore, phase change incorporation on micro-ring resonators have received extensive attention to realize the functionality of a fully optically addressable photonic memory cell for wavelength division multiplexing applications. Rios *et al.* in 2015 embedded 10nm thick GST films on three MRRs with different radii to demonstrate reconfigurable multi-level transmission outputs in a wavelength dense

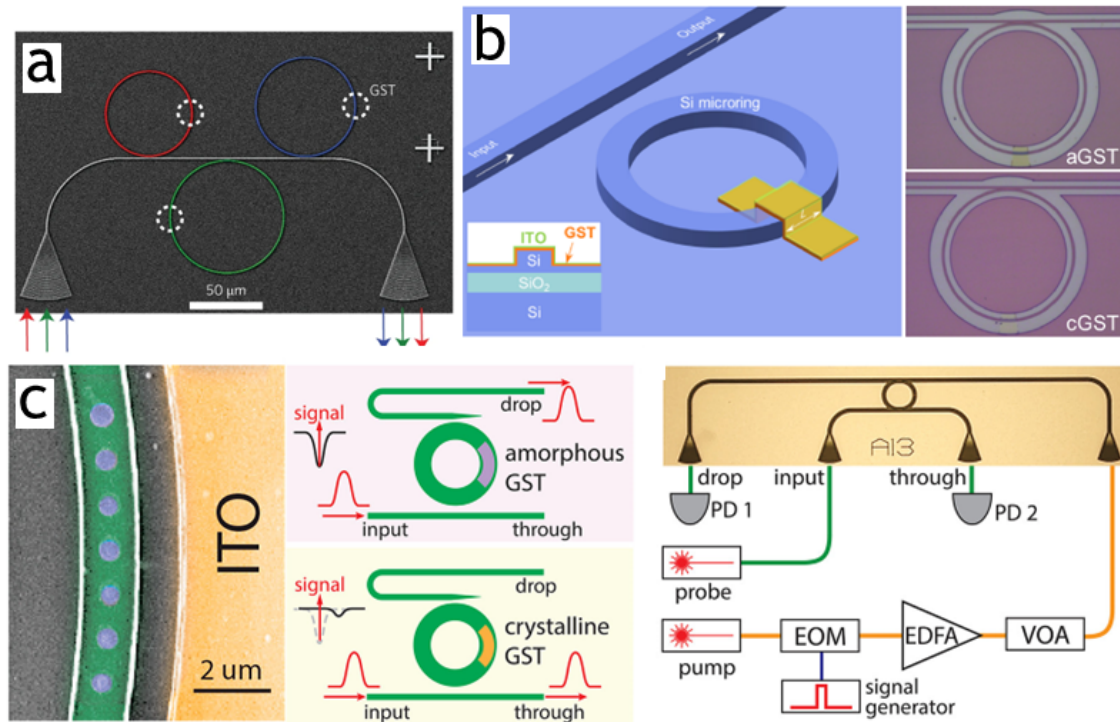


Figure 3.8: Phase change material integration on photonic micro-ring resonators. a.) spectrally separated MRRs attenuating input signal at different resonant wavelengths. b.) binary switching of MRR resonant behaviour between amorphous and crystalline GST phases. c.) discretized GST nanodisks to achieve intermediate transmission values upon successive phase transition of the individual structures.

configuration [74]. Laser pulses spectrally positioned on resonance of the respective MRRs served as the pump signal to switch GST between amorphous and crystalline phases. Inherent material losses of GST in both phases absorbed the optical intensity build up within the micro-ring cavity, to generate thermal energy resulting in an increase in the material temperature which were sufficient to reach both crystallization and amorphization temperatures. Differing only in pulsing protocols, a 10ns pulse amorphized GST while a train of consecutive 50ns pulses crystallized the material. Detuned away from the resonance wavelength, another signal is used to probe the

state of the GST MRRs. Shifting between the two phases resulted in a transmission contrast of 3dB. Extending this design concept to achieve a greater transmission contrast, authors Zheng *et al.* designed a series of MRRs to satisfy the critical coupling condition for amorphous GST which is comparatively lower in loss than crystalline GST [75]. GST strips of 20nm thickness were deposited on the outer portion of the micro-ring with various lengths ranging between 1 to $10\mu\text{m}$. Sharp resonance responses are observed for the amorphous phase; however, upon crystallization of GST, linewidths broadened and the spectrum red-shifted corresponding to an increase in loss and an increase in effective index respectively. At a GST patch length of $4\mu\text{m}$, switching between amorphous and crystalline phases resulted in a transmission contrast of 33dB. Prior demonstrations illustrate the non-volatile tunability of PCM embedded MRRs between two distinct states or transmission levels; however, to realize a “broadcast and weight” based matrix vector multiplication scheme increased resolution of the weighting values is required. Authors Wu *et al.* present a segmented integration of GST on a MRR structure to achieve multi-level phase states [76]. A 10nm thick layer of GST was deposited and patterned into 500nm diameter disks on a silicon nitride micro-ring resonator. The dimensions of the nanodisk structures are sufficiently subwavelength to avoid unwanted scattering and critical coupling was designed for the amorphous phase. Optical pulsing provided the external energy to actuate a phase transition and eight distinct intermediate transmission states was observed during the amorphization process.

Chapter 4

Fiber Integrated Phase Change Metasurfaces With Switchable Group Delay Dispersion

We report on the demonstration of a fiber-integrated non-volatile reconfigurable metasurface providing high-contrast group delay dispersion switching functionality, which may be engineered to operate at wavelengths across the near-infrared (telecommunication) band. Light-induced amorphous-crystalline phase switching in a chalcogenide (germanium antimony telluride) metasurface, only a fraction of a wavelength thick fabricated on the end facet of a single mode optical fiber, enables intensity and phase modulation of the guided wave at metasurface designated bands. Such devices present a range of opportunities in fiberized remotely programmable phase/intensity multiplexing and dynamic dispersion compensation for emerging telecommunications and data storage processing applications, including in photonic neural networks and neuromorphic computing architectures.

Global data networks face a ‘capacity crunch’, as we approach the fundamental nonlinear Shannon limit of single-mode fiber transmission. This has galvanized in-

tense global research efforts in developing techniques based on a number of emerging signal multiplexing platforms that call for a new generation of components including rapidly reconfigurable spatial channel multiplexers, dispersion compensation devices, routers and memory elements with small physical footprints [77, 78]. Today’s data networks are largely optically opaque, consisting of electronic nodes connected by point-to-point fiber-optic links, reliant upon a series of volatile electro-optic conversions to move information across the network. This creates substantial data latency issues, large thermal footprint and substantial power consumption requirements. To date, the potential for in-fiber all-optical control (switching, routing, processing, and storage) of signals, which would remove electronic bottlenecks, remains largely unrealized and unexploited in networks. In pursuit of this goal, during the past decade, there has been increasing research interest in adaptive/tunable multi-material optical fibers [79–82], and in combining planar and fiber devices incorporating a range of materials through a variety of manufacturing techniques [83–85]. At the same time, there is rapidly growing interest in radically different photonic network architectures for neuromorphic (brain-inspired) computing and implementation of machine learning, which take advantage of the inherent parallelism of photonic technologies and again require ultra-compact, integrated elements for dynamic phase/amplitude modulation and optical memory [86, 87]. Functional media can be integrated with solid-core fiber and planar waveguides generically in one of two ways, based either on evanescent coupling to the guided mode [88] – whereby a material or structure is positioned around the waveguide side wall; or inline coupling – whereby a thin film, nanostructure or device intercepts the path of the guided mode, e.g. via a micro-collimator assembly (as in a variety of recent applications to nonlinear optics and sensing [50, 89–91]. In

the present case, we adopt the latter methodology to demonstrate fiber-integrated non-volatile dispersion switching elements based upon chalcogenide semiconductor phase-change metasurfaces manufactured on single-mode optical fibers. Photonic metasurfaces are artificial electromagnetic media nanostructured on the subwavelength scale. They present a highly flexible technology paradigm for engineering electromagnetic space and (actively) controlling the propagation of light and its interaction with matter. An extensive range of enhanced optical properties, including dynamically tunable/switchable and nonlinear functionalities, have been demonstrated at near-infrared and visible frequencies, in metamaterials and metasurfaces comprised of nanostructured plasmonic metals and high-index dielectrics [92]. Recently, the field of photonic metamaterials has evolved from being a nanotechnology-enabled paradigm for engineering new electromagnetic properties to the device and system levels [93], where practical devices for real world applications capable of field-deployment, can be realized through the integration of nanophotonic metamaterials and metasurfaces with optical fiber technology. To this end, a large number of different material platforms are being explored for use in photonic metasurfaces, including noble plasmonic metals, conductive oxides, refractory nitrides, perovskite, chalcogenides and superconductors [94, 95]. Among them, chalcogenide semiconductors (alloys of sulphur, selenium and tellurium) present an uniquely flexible material platform that can be manufactured in various forms; optical fibers, thin films, nanoparticles and monolayers; and grown and patterned using CMOS compatible processes [96, 97]. They have been at the core of optical disk technology (DVDs/Blu-rays) and emerging memristive electronic random-access memory devices [98–101]. However, they have much more to offer, aside from being good hosts for a variety of

metallic and rare-earth dopants, they present a number of compositionally tunable properties [102], from photo-conduction and infrared transparency to high optical nonlinearity and photorefractivity. Notably, the spectral dispersion of their response to electromagnetic fields is compositionally-controllable and spans a wide range of regimes (plasmonic, low and high refractive index) [103]. Therefore, such materials can provide for a variety of unusual and intriguing electromagnetic wave and light-matter interaction phenomena across ultraviolet (UV) to infrared IR frequencies. They can also exhibit heat/current/light-induced non-volatile, reversible switching between optoelectronically distinct amorphous and crystalline phase states, leading to substantive broadband changes in refractive index on femtosecond to nanosecond timescales [104].

Germanium antimony telluride ($\text{Ge}_2\text{Sb}_2\text{Te}_5$ or GST), as employed in this work, is a high-index dielectric in both its amorphous and crystalline states across the near-infrared spectral range. The amorphous to crystalline transition here entails an increase in the real part of the refractive index along with an associated increase in extinction coefficient as seen in Figure 4.1. The high refractive index and index contrast between phase states offered by GST at near-infrared wavelengths has been harnessed in the realization of thermally switchable hyperbolic metamaterials as well as laser-rewritable and optically switchable ‘all-dielectric’ and plasmonic (i.e. all-chalcogenide) metasurfaces [105]. In the visible range, crystalline GST is plasmonic (metallic), and phase switching can thus be engaged to turn the plasmonic resonances of all-chalcogenide metasurfaces on/off [106]. GST films with a thickness $t = 200\text{nm}$ are deposited on cleaved single mode optical fibers with a core size of $8\mu\text{m}$ (Thorlabs SM980-5.8-125), by RF sputtering. A base pressure of 2×10^{-4} mbar

is achieved prior to deposition and high-purity argon is used as the sputtering gas (70 ccpm to strike, 37 ccpm to maintain plasma). The fibers are held within 10K of room temperature on a rotating plate 150mm from the target to produce low-stress amorphous as-deposited films. Sub-wavelength period (i.e. non-diffractive) cuboids, with a fixed linewidth $W = 80\text{nm}$ and period P ranging from 900 to 1000nm, each covering an area of approximately $15\mu\text{m} \times 15\mu\text{m}$ (roughly twice the size of the core diameter), were etched through the GST layer by focused ion beam (FIB) milling, as illustrated in Figure 4.1 b and c. During processing, special care is taken to align the nanostructured area over the fiber core, ensuring experimental light measurements reflect the interaction of light with the structured medium fabricated on the tip of the fiber. The transmission characteristics of the fiberized devices were subsequently measured by focusing near-IR light ($1000 \leq \lambda \leq 1750\text{nm}$) from a broadband light source (Thorlabs SLS201L) onto the nanostructured fiber tip surface using a near-IR objective (Mitutoyo M Plan Apo NIR 10x; $NA = 0.26$) and collecting the output using an Optical Spectrum Analyzer (Ando AQ-6315E).

Figure 4.2a shows the normalized (relative to an unstructured GST-coated fiber tip) measured transmission spectra of three fiber-integrated phase change metasurfaces with periods 900, 950, and 1000nm. These show transmission resonances with spectral positions dependent upon the period of the nanostructured cuboids. Figure 4.2b presents the simulated transmission spectra corresponding to three different periods of GST metasurfaces in their as-deposited amorphous phase with the same geometry as those experimentally fabricated. The simulations were run using a finite difference time domain solver (Lumerical FDTD Solutions [107]). The model assumes a lossless non-dispersive silica substrate with refractive index of 1.45 and

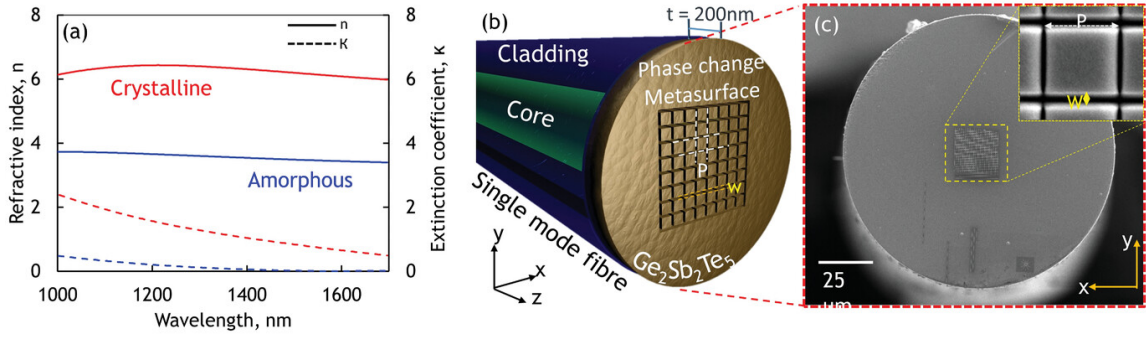


Figure 4.1: a.) Near-infrared spectral dispersion of the refractive index (n) and the extinction coefficient (κ) of GST in the amorphous (blue) and crystalline (red) phases. b.) schematic diagram of the fiber-integrated phase change metasurface optical switch based on GST. c.) scanning electron microscope image of the fiber metadvice; inset, detail of the cuboid GST metasurface structure.

uses ellipsometry measured values of the complex permittivity for GST, as presented in Figure 4.1a. In addition, normal-incidence illumination using a plane wave is considered. By virtue of periodic boundary conditions, an infinite array of GST cuboids in the x and y planes is simulated. The spectral positions of the resonances are aligned between experimentally measured and numerically simulated transmission spectra suggesting that the overall metamaterial geometries are in good agreement. Therefore, owing to the fact that the nanostructured GST covers an area of the fiber tip surface far greater in size than the core, considering a simple geometry for our model consisting of a periodic array of GST cuboids on top of a silica substrate, with refractive index equal to that of the fiber core, is found to be sufficient in establishing a good qualitative and quantitative representation of the fiber-tip-integrated experimental device characteristics. Discrepancies in the shape and value of the transmission spectrum across the three periods can be attributed to imprecise experimental measurement setups and manufacturing imperfections, i.e. deviations

from the ideal model geometry such as slight over-milling of etched lines into the substrate, the tapered/rounded cross-sectional profile of milled lines and the possible contamination/stoichiometric drift in the GST layers during FIB milling, which may slightly modify the refractive index. The resonant response of the metasurface presents an opportunity for spectral phase modulation at structurally engineered wavelength bands dictated by the metamolecule geometry. The group delay dispersion (GDD) is shown in Figure 4.2c. Group delay dispersion is the second derivative of the change in spectral phase with respect to wavelength given by the equation:

$$GDD = \frac{\lambda^3}{2(\pi c)^2} \left[\frac{d\phi}{d\lambda} + \frac{\lambda}{2} \frac{d^2\phi}{d\lambda^2} \right] \quad (4.1)$$

where λ is the wavelength, c is the speed of light in vacuum, and ϕ is the spectral phase. Here, the phase and transmission for each metasurface in both amorphous and crystalline phases, across the spectral range of $\lambda = 1370\text{nm}$ to 1570nm , were extracted from Lumerical FDTD and imported into MATLAB for processing. Within the FDTD environment, the grating S-parameter analysis group was utilized to obtain both transmission and phase data through the complex scattering parameter S21. As longer periods are considered and keeping with the ensuing enhanced Q-factors linked to the transmission dips, higher maximum absolute GDD is attained for metasurfaces with $P = 1000\text{nm}$, showing 0.33 ps^2 as the highest possible numerically simulated GDD. Positive (normal) and negative (anomalous) GDD values can also be engineered around the resonant spectral position.

The amorphous to crystalline transition in chalcogenides is an annealing process that can be instigated through heating the material to a temperature above the materials' glass-transition point T_g ($\approx 160^\circ\text{C}$ for GST), but below its melting point T_m

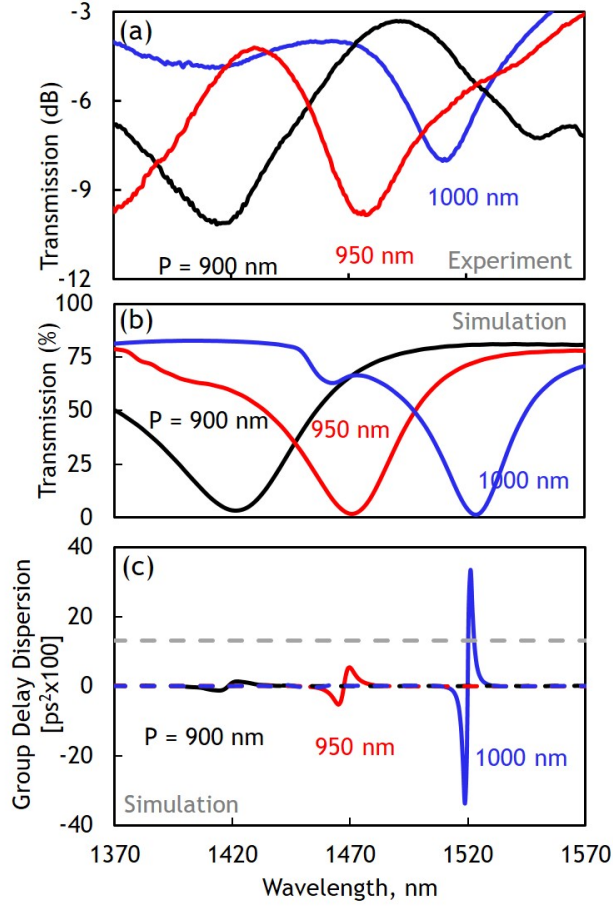


Figure 4.2: a.) experimentally measured and b.) simulated transmission spectra for arrays of GST cubes with $w = 80\text{nm}$, $t = 200\text{nm}$ and P taking three different values: 900, 950, 1000nm. c.) corresponding simulated spectral profile of the Group Delay Dispersion (GDD); the grey dashed line identifies the level of dispersion introduced by 1m of single-mode telecom fiber (considering a fiber group velocity dispersion of 20 ps/nm km); the black, red, and blue dashed traces show the off-resonance GDD for arrays with $P = 900, 950, 1000\text{nm}$, respectively.

(600°C). The reverse transition, a melt-quenching process can be driven by shorter higher energy pulsed excitation that momentarily brings the material to a temperature above T_m . To evaluate the performance of our device in both structural phases,

the fiber-integrated metasurfaces are illuminated with continuous wave (CW) laser light at $\lambda = 1550nm$, which thermally anneals the surface area overlapping the fiber core, where the metasurface is fabricated. Reflectivity of the metasurface/fiber interface is monitored through the fiber via a circulator where an increase in reflectivity at $\lambda = 1550nm$ being indicative of GST crystallization. This experimental configuration enables light-induced crystallization of the GST metasurface via the fiber, i.e. in a manner compatible with remotely programmable fiber-integrated device architectures.

The changes in the spectral dispersion of transmission resulting from the crystallization of the nanostructured GST metasurface are presented in Figure 4.3, with corresponding numerical simulations of the expected transmission change presented in Figure A.1. The transition from the amorphous to the crystalline state involves an increase in the real part of the GST refractive index which results in a red-shift and substantial broadening of the resonant feature, rendering it almost imperceptible. This is accurately reproduced in corresponding numerical simulations Figure 4.3a and b. While the corresponding increase in the imaginary part of the GST refractive index brings about a decrease in average transmission of the device across the spectral range under investigation and a broadening of the overall resonance feature. It should be noted that as stated previously, phase transitions are actuated using a coupled CW laser light at $\lambda = 1550nm$, which thermally anneals the surface area overlapping the fiber core, where the metasurface is fabricated. In simulations this is assumed as a perfectly uniform spatial distributed phase transition; however, in reality, this will create a randomly distributed mixture of slightly different clusters with different levels of crystallinity in the metasurface, which translates to the slight

discrepancy seen in the crystalline phase simulations.

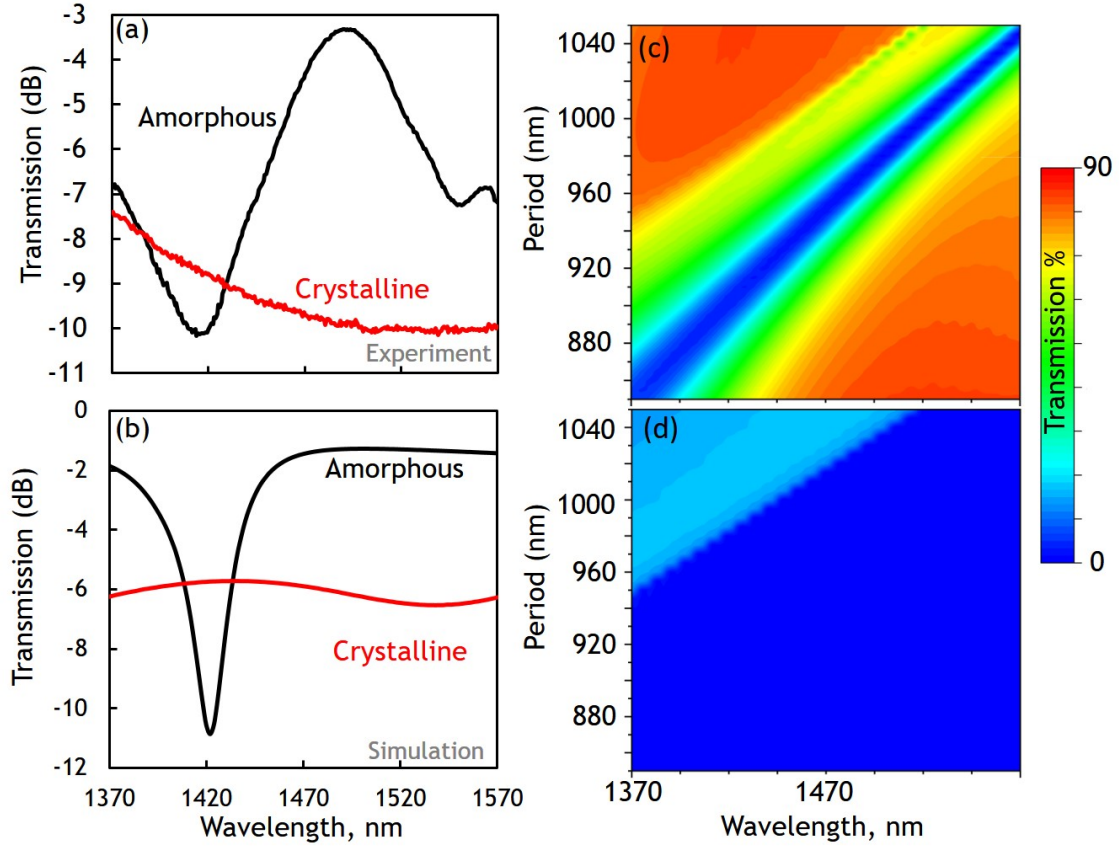


Figure 4.3: a.) measured and b.) simulated transmission spectra for a metasurface with $w = 80nm$, $t = 200nm$, $P = 900nm$, in the amorphous (black) and crystalline (red) phases; along with corresponding numerically simulated transmission of metasurfaces ranging from 850nm to 1050nm periods in c.) amorphous and d.) crystalline states, with resonances covering the E, S, and C telecommunication bands.

Numerically simulated field maps display the spatial profiles of the electric field in the metasurfaces along with the magnetic field (Figure A.2), along a vertical plane cutting through the GST cuboids in both fully amorphous and crystalline phases of the GST layer. These field profiles help to characterize the resonances harbored by

the proposed reconfigurable fiber-tip-integrated nanostructures. In a closed-packed metasurface array arrangement, the observed resonance is seen to arise from the collective mode of the array. Therefore, the electric field can be seen mostly confined to the gap between cuboids (either in the silica substrate or constrained to the air/GST interface), with little electric field intensity confined inside the GST layer. The field maps in Figure A.2, section 8.1 of the appendix, demonstrate that for both the electric and magnetic fields, the variation in optical parameters associated with the structural phase transition induced in the GST film leads to a change in the spatial distribution of electric and magnetic field intensity confined in the GST layer as well as at the GST/air and silica interfaces.

As Figure 4.4a exemplifies, by changing the phase of the GST layer in a structure with $P = 900\text{nm}$, the considerable phase modulation observed in the amorphous state is rendered almost imperceptible after crystallization. Consequently, the GDD collapses, being reduced from a maximum absolute value of 0.013ps^2 in the amorphous state down to a maximum of 0.0021ps^2 upon crystallization. The change in GDD translates to a substantial change in the optical phase of a propagating signal as shown in Figure 4.4b. With a view to practical applications, a figure of merit (FOM) is defined, relating the change in transmission (T) of a given signal with the change in GDD upon structural phase transition (A and C denote amorphous and crystalline phases respectively):

$$FOM = \frac{|GDD_A - GDD_C|}{|T_A - T_C|} \quad (4.2)$$

In such a representation, the higher the FOM, the higher the capability of the fiber integrated metasurface to introduce a large change in dispersion accompanied by a

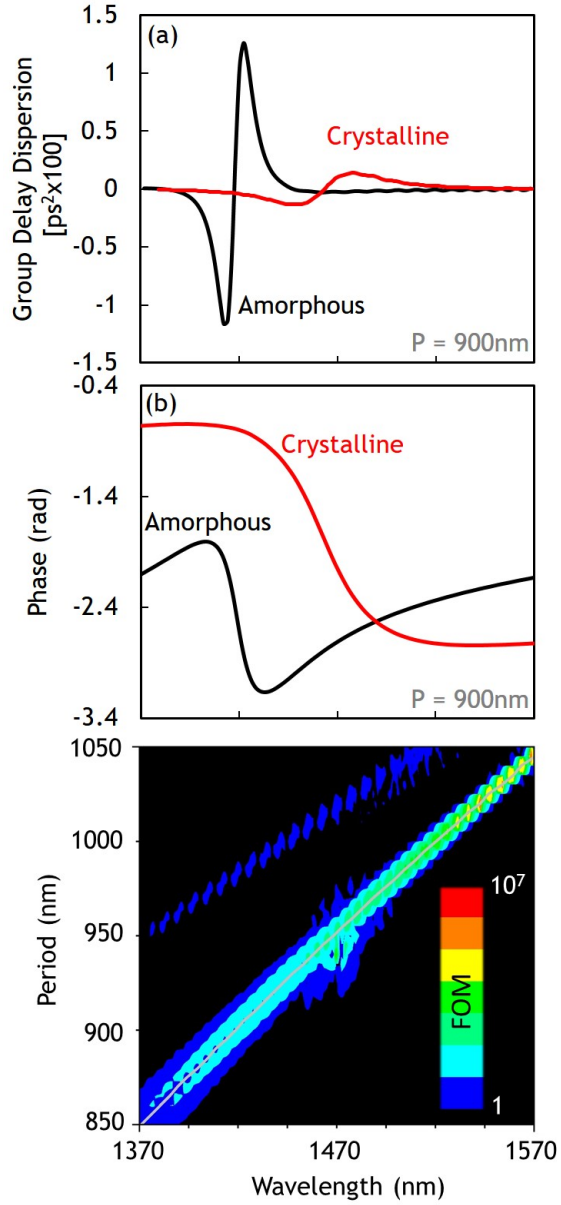


Figure 4.4: Numerically simulated GDD for amorphous and crystalline states of a metasurface with $w = 80\text{nm}$, $t = 200\text{nm}$, $P = 900\text{nm}$, along with corresponding b.) phase and c.) FOM calculated for metasurfaces with periods ranging from 850nm to 1050nm. The color black indicates FOM=0. Magenta line indicates the region where $T_a = T_c$

small change in the amplitude of the transmitted signal. As shown in Figure 4.4c, the highest FOM is observed at the spectral position of the resonance wavelengths for a given metasurface. This can be tuned from the E to C telecom bands by changing the period of the cuboid metamolecule and shows a gradual increase at higher wavelengths due to the reduced losses in the GST layer which brings about an increase in the quality factor of the resonant feature. It should be noted that at positions where $T_A = T_C$, the FOM will yield high values that tend to infinity. These regions have been indicated by the violet diagonal trendline in panel c of Figure 4.4.

In conclusion, we have demonstrated reconfigurable phase-change metamaterials with intensity and dispersion switching capability nanofabricated directly on the tip of a silica optical fiber. Such devices can be mechanically spliced to existing networks enabling the merging of the optical fiber and reconfigurable metamaterial fields into a single robust monolithic device platform free from alignment issues and ready for commercialization and integration in global telecommunication networks, drastically reducing physical footprint, data latency, bottlenecks, and power consumption in such devices. Specifically, this work establishes a new device platform for non-volatile all-optical intensity and phase modulation using fiber-integrated metasurfaces based on nanostructured subwavelength thickness phase change GST films deposited on fiber tips. The use of metasurfaces enables the tuning of the spectral position of the metasurface transmission resonances, by adjusting metamolecule geometry, enabling structurally engineered resonant operation anywhere within the transparency range of the GST alloy. The device concept is, furthermore, transferrable to other spectral bands and through using different metamolecules and/or other chalcogenide alloys

can be used for non-volatile control of a variety of different optical properties in all-fiber devices, including group velocity and polarization mode dispersion, for low power, all-optical long-range data transmission as well as reconfigurable channel multiplexing in emerging photonic lantern technologies. Moreover, such devices enable control over signal intensity and phase with built-in memory functionality, thus provide solutions well beyond purely telecommunication network applications. These devices unlock a range of exciting applications in endoscopic imaging and smart textiles for wearable technologies to LiDAR for autonomous vehicles and adaptive industrial process monitoring.

Chapter 5

Chalcogenide Phase-Change Material Integration on Photonic Waveguide Structures

The large information-carrying capacity of low loss optical fibers are suitable for long-haul communication links between high density data processing nodes within a network. Due to the constraints of the fiber drawing process during fabrication, optical fiber – based complex signal modulation functionalities have not been realized. Consequently, optical fibers have largely remained as a passive signal transmission component. Recent advancements in CMOS processing technologies have enabled the development of a comprehensive library of both passive and active photonic components including, high speed modulators, integrated narrow-linewidth lasers, and ultrafast germanium photodetectors to address the growing demand for large bandwidth low latency telecom networks [108]. In this chapter, we explore the integration of non-volatile chalcogenide phase-change materials on silicon photonic waveguides to realize signal intensity and phase modulation capabilities with optical in-memory functionalities.

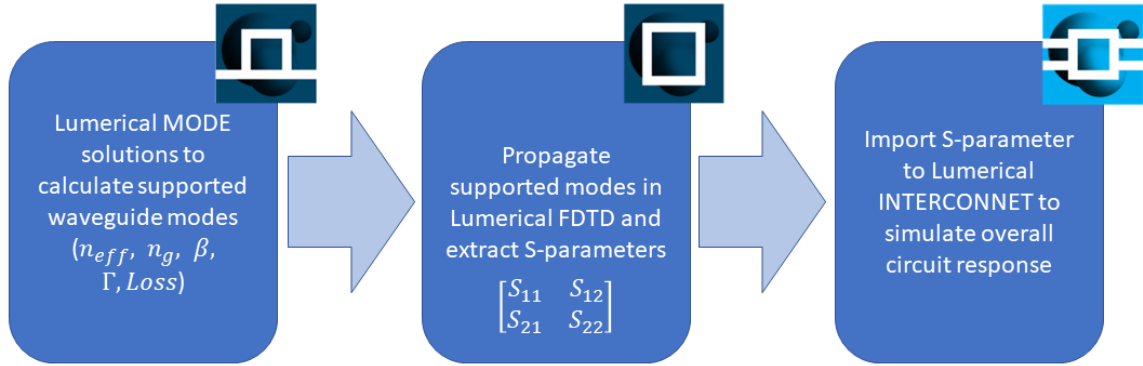


Figure 5.1: Simulation workflow diagram to analyze PCM integrated waveguide devices. From left to right, waveguide characteristics are first determined with MODE solutions, the mode propagates in 3D FDTD environment down the device where ports extract relevant S-parameters, and subsequently overall circuit response is generated from INTERCONNECT with the imported compact model.

Figure 5.1 depicts a typical simulation workflow to construct and characterize the PCM integrated photonic device. The photonic waveguide with PCM structure is modelled within Lumerical MODE solutions to determine the fundamental propagating TE polarized mode. Specifically, the finite difference eigenmode (FDE) solver is used to calculate all possible modes of the hybrid dielectric waveguide structure. Metal boundary conditions are used which necessitate convergence testing. The span of the bounding box is swept to ensure the placement of the metal boundary does not interact with the evanescent mode of the waveguide. The defining properties of the mode such as effective index, group index, and loss values are extracted. For either inclusion of thin film PCM or subwavelength nanostructured metasurface arrangement, the impact of a finite PCM patch on phase and intensity is determined using a fully vectorial solve in Lumerical 3D FDTD. Port objects are utilized as convenient source and monitor objects to ultimately determine scattering parameters that will

become the compact model response to describe the component. Finally, the compact model is imported into the photonic circuit simulator—INTERCONNECT—to analyze the overall circuit response. An optical spectrum analyzer object is used to extract the intensity spectrum plotted across wavelength.

5.1 Optically large rectangular waveguides with thin film chalcogenide phase-change material

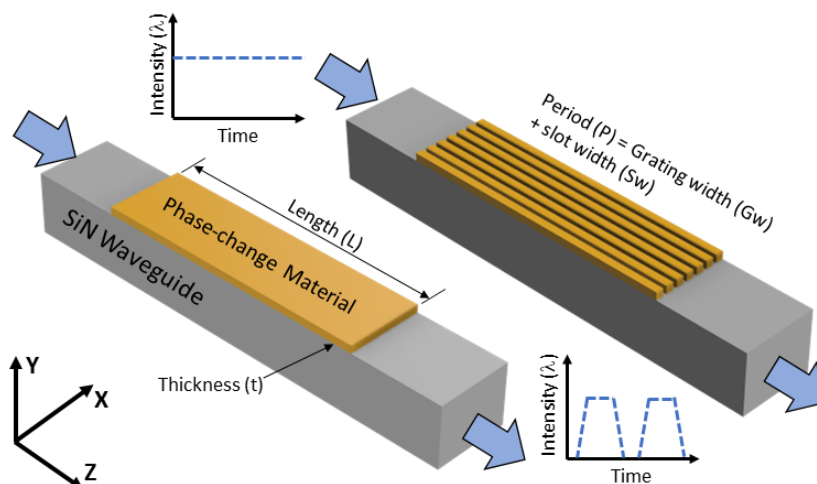


Figure 5.2: Schematic of chalcogenide phase change material incorporated on a large dimension silicon nitride photonic waveguide in a thin film format (left) and a meta-surface subwavelength grating structure (right) to modulate signal intensities at designated wavelengths of interest.

We report on the utilization of (GST – 225) as a functional material to realize a non-volatile zero static power consumption intensity modulation device on integrated silicon photonic waveguide platforms. Previous literature examples showcasing the functionalization of optical waveguides with phase – change material, in particular the thin film integration of side-polished (or “D-shaped”) fibers creating a reconfig-

urable Fabry-Perot cavity resonance at designated spectral frequencies by Martins *et al.* [88], served as a starting point for the monolithic planar waveguide structures explored here. Employing numerical modelling software (Lumerical finite-difference eigenmode – MODE solutions) a similarly sized rectangular waveguide core ($8 \times 4\mu\text{m}$) was modelled and simulated. Within this integrated system, the refractive indices should be considered for maximizing interaction between the propagating waveguide mode, and the addition of a functional PCM layer. To satisfy the dielectric waveguiding condition, the core waveguide structure should possess a higher refractive index than the surrounding medium; therefore, platforms such as silicon-on-insulator and silicon nitride-on-insulator are prime candidates which meet this criterion. Presented in Figure 5.3 are the experimentally extracted dispersion relations between silicon, silicon nitride and amorphous/crystalline GST across the telecommunications near-infrared spectrum. GST is a high index dielectric medium within this wavelength range, having a refractive index ($n = 3.46$ at $\lambda = 1550\text{nm}$)—comparable to silicon ($n = 3.45$)—in the amorphous phase and increasing to a refractive index of $n = 6.1$ upon crystallization. Following a material phase transition, the GST phase-change material becomes optically lossy due to a significant increase in the extinction coefficient; therefore, to minimize insertion losses and improve transmission contrast ratios of signal modulation devices, it is advantageous to engineer resonant conditions within the amorphous phase.

Owing to the maturity and CMOS compatibility of the silicon-on-insulator (SOI) platform, initial investigations were carried out on a silicon core waveguide architecture. Within the finite-difference eigenmode solver module of Lumerical MODE solutions, the phase-change waveguide model consisted of an $8\mu\text{m}$ wide by $4\mu\text{m}$ thick

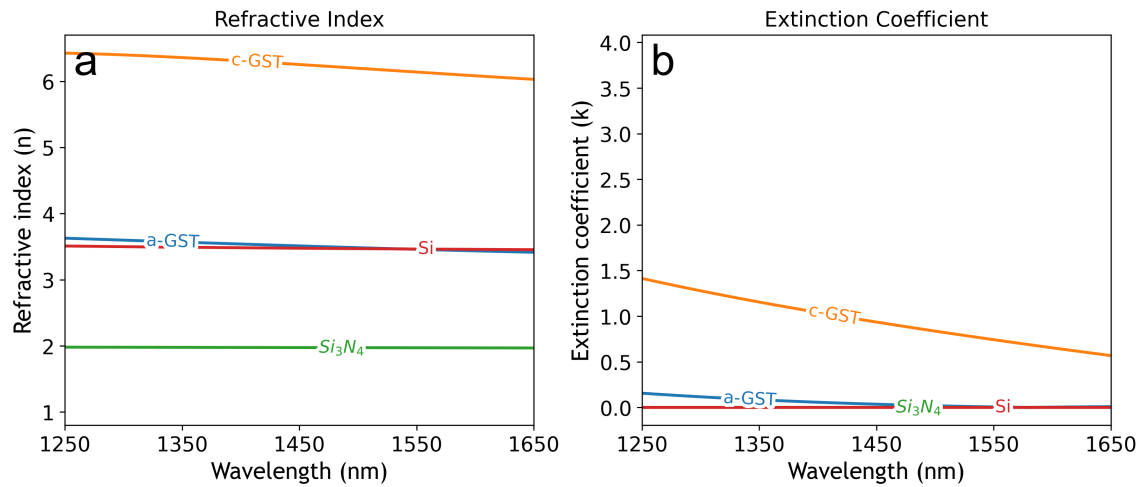


Figure 5.3: Material dispersion profile of silicon, silicon nitride and GST-255 across the telecommunication wavelengths: ranging from the O-band to the L-band. a.) Refractive index and b.) extinction coefficient

silicon waveguide on a silicon dioxide substrate with an air clad surrounding. The simulation boundaries were metallic and placed sufficiently far such that the evanescent modal fields decayed below -20dB to ensure convergent results. A 500nm thick layer of GST was placed on top of the waveguide and subsequently the supported eigenmodes were calculated. Illustrated in Figure 5.4a, is the fundamental transverse electric (TE) mode, showing a highly confined modal field without any noticeable interaction with the GST layer due to the combination of the high refractive index of silicon and the large dimensions of the waveguide core. To elicit a stronger field interaction with the GST film a silicon dioxide waveguide core was considered next, with the substrate material holding an index value lower than glass which can be achieved through photoresist or optical printing resin. This configuration created a similar index environment to the side polished optical fiber and from Figure 5.4b, an enhanced field interaction with the GST layer is confirmed. However, the proximity

of the high index amorphous GST film to the silicon dioxide waveguide core created favourable waveguiding conditions within the GST film itself, and thereby lead to multi-mode propagation and high insertion losses. Therefore, a balance between single mode integrity and field interaction with the GST thin film should be carefully assessed. The refractive index of the silicon nitride material platform presents an attractive solution as the ratio of silicon to nitrogen elements directly impacts the optical refractive index of the material. Specifically, stoichiometric silicon nitride (Si_3N_4) with a refractive index value of 1.97 across the main telecommunication bands of interest, demonstrate the desired balanced between single mode propagation and field interaction with the GST layer as shown in Figure 5.4c. Therefore, moving forward, stoichiometric silicon nitride was chosen for the waveguide core material.

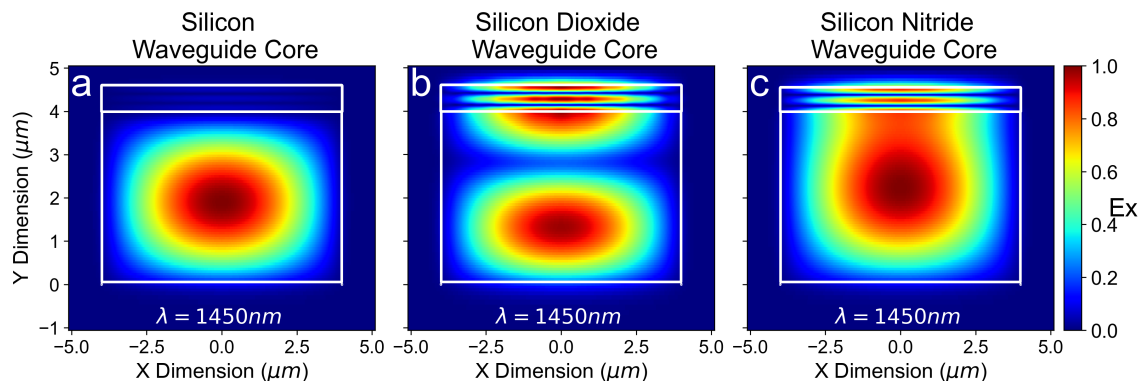


Figure 5.4: Cross section of the GST integrated waveguide (signal propagation in the z-direction) intensity modulator for different core materials: a.) silicon, b.) silicon dioxide, c.) silicon nitride

The induced thin film resonance within the amorphous GST layer can be considered as a quasi Fabry-Perot (FP) cavity. Exemplified in Figure 5.4c, two dis-

tinguishable electric field maxima lobes are present in the 550nm thick GST film. Considering the physical geometry of a FP resonant cavity dictates the spatial distribution of modal electric field interactions and consequently the spectral positioning of optical resonances, we show the tunability of this thin film resonance by changing the GST layer thickness. Shown in Figure 5.5 are three different GST thicknesses: 500nm, 550nm, and 600nm, each corresponding to different spectral positions centered on 1367nm, 1467nm, and 1565nm respectively. The waveguide integrated GST thin film platform demonstrates a broadband shift of 200nm throughout a thickness variation of only 100nm, resulting in a thickness to spectral resolution ratio of 2:1. The calculated transmission response for this configuration, generated from Lumerical MODE solutions, makes the assumption that the signal solely propagates in the hybrid waveguide structure; therefore, the next parameter to consider is the minimum required length of the integrated GST layer to achieve lowest resonance transmission depth and maximize extinction ratio (the ratio between high and low transmission values in signal modulation components).

Within a fully vectorial 3-dimensional FDTD (finite difference time domain) solver in Lumerical, the GST hybridized silicon nitride waveguide was modelled with an input and output section without the inclusion of the GST thin film. Port objects were used as both the source to inject the fundamental TE mode as well as the monitor to detect this propagating mode along the z – direction. Perfectly matched layers (PML) were used as the boundaries along the z – direction to aid in the absorption of the optical signal, while metallic boundary conditions were used in the periphery as most of the modal field strength is concentrated within the waveguide core. For a constant GST thickness chosen to be 550nm, a range of patch length

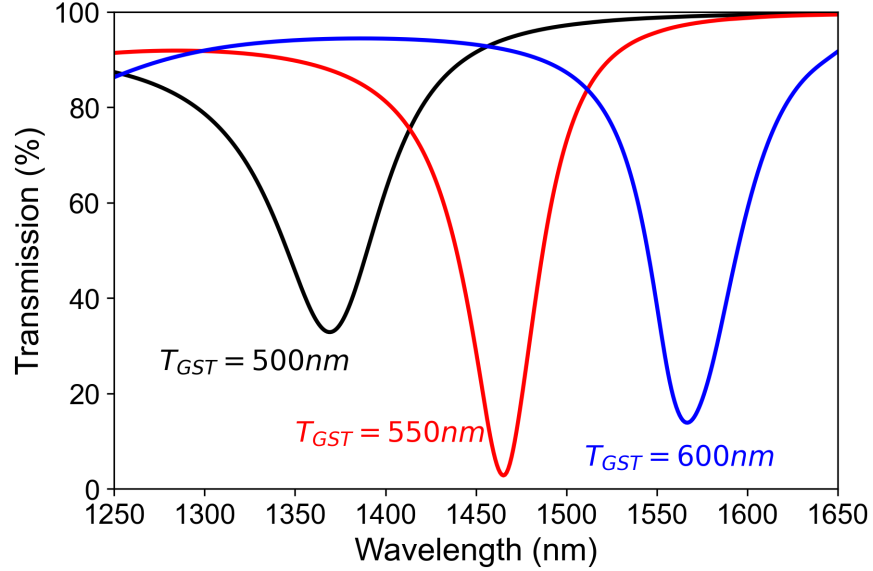


Figure 5.5: Spectral tunability of GST thin film integrated photonic waveguide demonstrated with changing thicknesses. Thicknesses of 500nm, 550nm, and 600nm correspond to resonances centered at $\lambda = 1367nm$, $1467nm$, and $1565nm$ respectively.

values were considered and simulated. Depicted in Figure 5.6a, are the set of transmission spectra corresponding to patch lengths ranging from $40\mu m$ to $150\mu m$. With a resonance centered on $1467nm$, a trend appears in the transmission curve which correlates that the patch length is proportional to the achievable resonance depth, but up to a certain point. Defining transmission depth as:

$$\Delta T = T_{off \text{ resonance}} - T_{on \text{ resonance}} = T_{\lambda=1300nm} - T_{\lambda=1467nm} \quad (5.1)$$

Figure 5.6b shows the relation between transmission depth and the GST thin film length. Transmission depth increases sharply between length values of $40\mu m$ to $100\mu m$ before flattening and starts to decrease for lengths larger than $110\mu m$.

Although small but not negligible, the extinction coefficient of amorphous GST is the source of optical loss for resonant modes propagating over large distances; however, in the limit of short distances, the modal interaction is restrained, thereby leading to low transmission depth. A GST thin film length of $100\mu m$ is the ideal choice to both maximum transmission depth and minimize insertion losses.

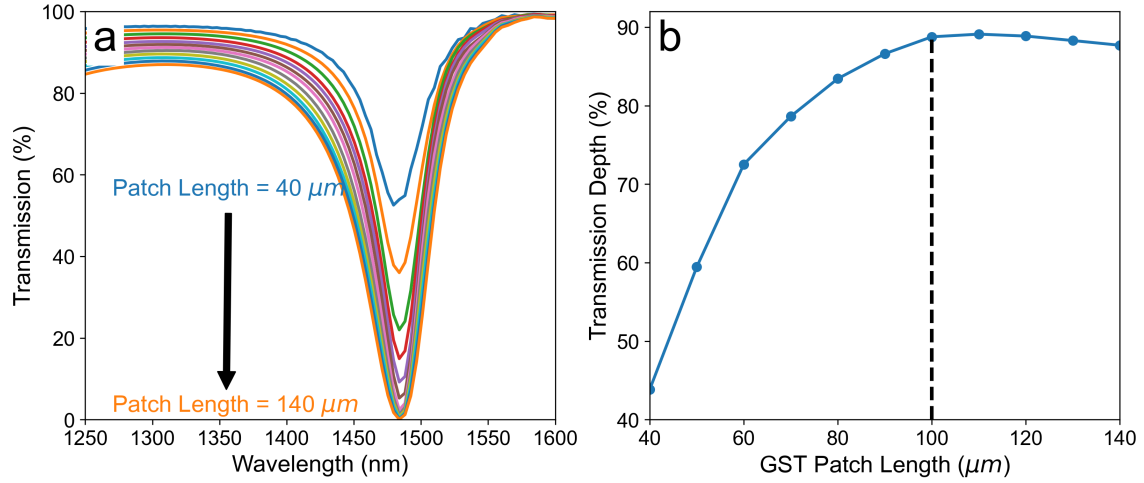


Figure 5.6: a.) transmission for a range of GST patch lengths ($40\mu m$ to $100\mu m$) in the waveguide propagation direction for a constant thickness of $550nm$. b.) transmission depth as a function of varying GST thin film length, defined as the transmission delta between off-resonance ($\lambda = 1300nm$) and on-resonance ($\lambda = 1467nm$).

Given the fixed refractive index profile of the chosen phase-change material (GST), nanostructuring the thin film layer at the subwavelength scale provides another design dimension to engineer desired optical responses that are otherwise unavailable through material discovery methods. By leveraging effective medium and Mie resonance design philosophies utilized in metamaterial and metasurface devices, we can generate similar optical resonant responses in a compact footprint on a waveguide platform. The same $550nm$ thick GST with nanostructuring along the signal prop-

agation direction was explored. Building upon the established FDTD model in the previous section, a series of etch gratings with fixed widths of 130nm, are placed within the GST layer, creating an all-dielectric phase-change material meta-grating (Figure 5.2). Illustrated in Figure 5.7a is the meta-grating response in the amorphous and crystalline phases for a grating period of 750nm. A pronounced multi-spectral resonance is produced in the amorphous phase, while a flat line response is associated with the crystalline phase. The markedly difference in the optical response is evident in the electric field interaction plotted in panel b and panel d for amorphous and crystalline GST respectively. The propagating waveguide mode couples into the low loss amorphous phase, creating discretized resonance modes within the grating bars. In contrast, the large refractive index difference between stoichiometric silicon nitride and crystalline GST limits any significant field coupling into the grating bars. Through reconfigurable phase transitions between amorphous and crystalline phases, field coupling to the meta-grating structure can be regulated. The switching functionality between high and low transmission centered on the spectral position of the meta-grating resonance ($\lambda = 1428nm$) can provide signal intensity modulation with a transmission contrast up to 5dB where transmission contrast ratio is defined as the transmission ratio of the amorphous to crystalline phase in log scale.

For any metamaterial/metasurface device, a subwavelength resonant unit cell structure is arrayed across a finite area to generate an artificially induced optical response. The physical spacing between adjacent subwavelength nanostructures—or period—determines specific resonant conditions for the field distributions such that only a small range of wavelengths can satisfy. By changing the period of the GST meta-grating structure, we show spectral tunability across the entire telecommuni-

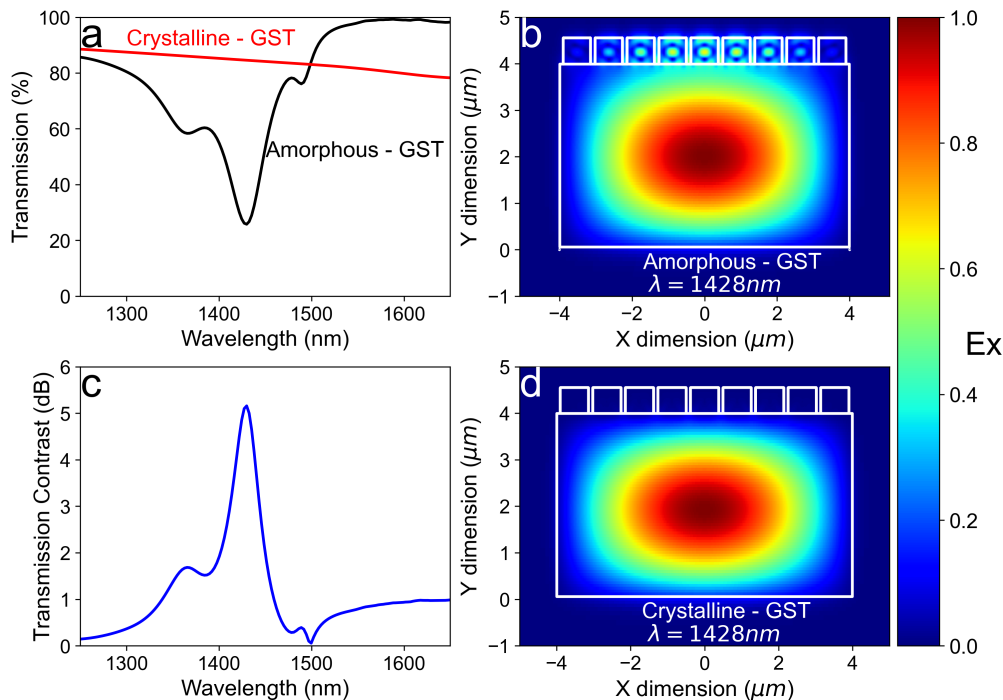


Figure 5.7: Reconfigurability of phase change GST illustrates signal intensity modulation. a.) amorphous GST produce 3 distinct metamaterial resonance responses with the main resonance interaction centered at 1428nm, while crystalline GST produces a flat high transmission response. b.) Modal field interaction with the amorphous GST meta-gratings. c.) Transmission contrast between amorphous and crystalline phases. d.) the lack of modal field interaction with crystalline GST meta-gratings.

cations range for both narrowband and multi-resonant broadband responses. Three periods including 750nm, 850nm and 950nm are compared in Figure 5.8. An increase in period, results in the red-shifting of meta-grating resonances and due to the increase in grating geometry, multiple resonance modes appear at different wavelengths.

Signal propagation down a dielectric waveguide, whether in optical fibers or integrated photonic circuits, experience distortion in the form of pulse broadening

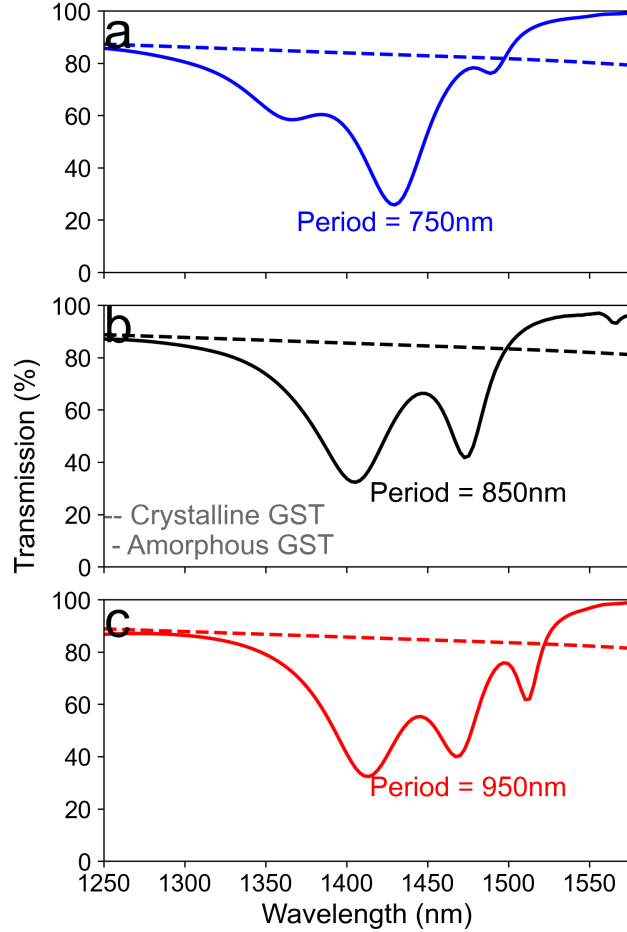


Figure 5.8: Changes in the period of nanograting metasurface show tunable narrow-band to wideband operation across the telecommunication spectrum for a.) Period = 750nm, b.) Period = 850nm, c.) Period = 950nm

due to the wavelength dependence of optical materials refractive index—commonly known as dispersion or chromatic dispersion. This phenomenon is the reason why a prism will split an incoming ray of white light into a multicolored spectrum. The pulse broadening effect ultimately limits the data carrying capacity of an optical waveguide channel. As two consecutive pulses representing bit 1s for example are

transmitted down an optical waveguide, both pulse profiles will spread in time after propagation leading to the two signals overlapping and becoming indistinguishable from each other. A material's refractive index wavelength dependency gives rise to group velocity (the speed of which the envelope of a signal pulse travels defined by: $v_g = \frac{d\omega}{dk} = \frac{c}{N_g} = \frac{c}{n - \lambda \frac{dn}{d\lambda}}$) being dependent on wavelength. Therefore, each spectral component of a signal pulse will travel at different group velocities and after propagating through a fixed length (L), each component will experience a different group delay ($\tau_g = \frac{L}{v_g}$). The group delay difference or group delay dispersion (GDD) can be defined in terms of spectral phase as:

$$GDD = \frac{\lambda^3}{2(\pi c)^2} \left[\frac{d\phi}{d\lambda} + \frac{\lambda}{2} \frac{d^2\phi}{d\lambda^2} \right] \quad (5.2)$$

where c is the speed of light in vacuum, and $\phi = \beta L$. Plotted in Figure 5.9, are the corresponding group delay dispersion associated with the three periods of the GST meta-grating for both amorphous phase in solid line and crystalline phase in dashed line. Due to the lack of field interactions in the crystalline phase, as seen in Figure 5.7d, the GDD contributions are negligible; whereas, the metamaterial resonant modes in the amorphous phase generate both positive and negative GDD values around the resonant spectral location. Therefore, by engineering the period of the GST meta-grating, different GDD profiles can be achieved to compensate for signal pulse broadening. The broadband multi-spectrum resonances generated by the amorphous phase contribute GDD values ranging from $\pm 11 fs^2$ to $\pm 52 fs^2$.

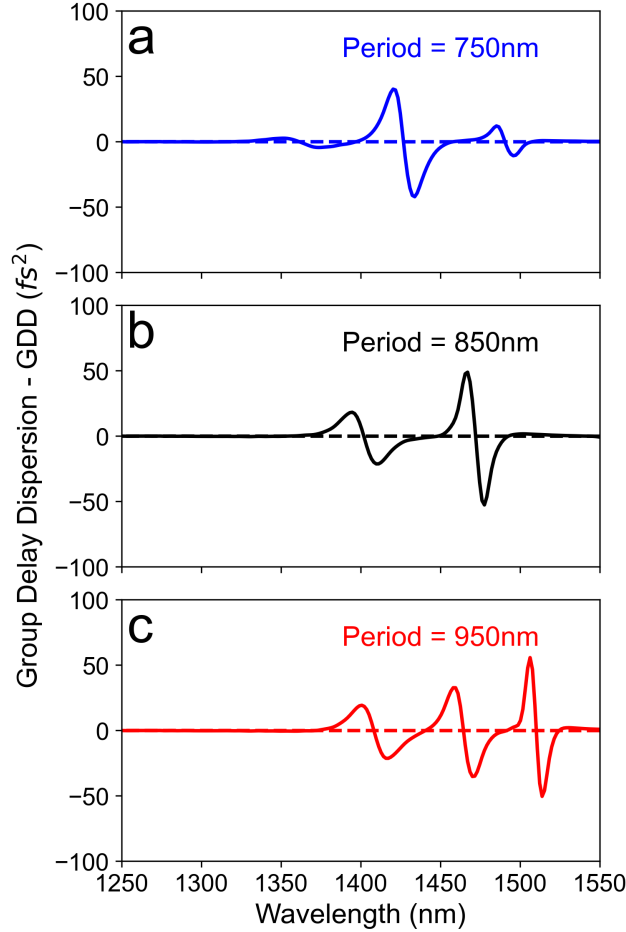


Figure 5.9: Corresponding group delay dispersion profiles for periods of 750nm, 850nm, and 950nm. Solid line shows the amorphous phase, while dashed line represents the crystalline phase.

5.2 Addition of resonant GST metamaterial on silicon nitride integrated photonic waveguides

Stoichiometric silicon nitride at thicknesses above 300nm begin to exhibit significant internal compressive stresses which leads to fracturing, cracking of the thin film and possibly, delamination from the substrate layer. Various mitigation strategies

can be employed to overcome this challenge such as iterative deposition at tens to hundreds of nanometers followed by thermal annealing to reach the desired thicknesses or damascene-based deposition which helps to alleviate the build-up of stress points along a certain direction of the thin film [11]. Considering the dimensions of the waveguide in the previous section, a thickness of 4 microns presents a significant fabrication barrier to overcome given the unproven reliability of the mitigation strategies. Therefore, small—sub micron—dimension silicon nitride waveguides should be considered to implement modulation devices based on phase-change chalcogenide integration achievable across the materials two markedly different phases of amorphous and crystalline.

A mature integrated photonics process based on silicon nitride is available from Applied Nanotools (ANT)—a local company providing rapid turnaround prototyping for photonic integrated circuits and components [109]. Company associates provided the relevant information for their silicon nitride process including material dispersion data and the dimensions of the routing waveguide which consisted of 400nm thick silicon rich SiN_x at a width of 750nm. Using Lumerical MODE solutions, the refractive index data and the geometry of the waveguide was modelled to understand the optical properties of the photonic platform. Figure 5.10a show the effective index of the fundamental TE mode gradually increase as the width of the waveguide is increased. At the width of 750nm, the effective index of 1.589 is significantly higher than the baseline index established by purely silicon oxide material: corresponding to a well confined waveguide mode. Figure 5.10b illustrates the various bend radii insertion loss of the silicon nitride waveguide platform for 90 degrees bend. Calculation of the insertion loss considers the mode overlap between straight and bend waveguide

section as well as the propagation loss associated with 90 degrees bend itself. From the plot, an insertion loss of -0.01dB or less is achievable for a bend radius of $75\mu\text{m}$ or more; however, negligible reductions in losses are observed for radii larger than $100\mu\text{m}$. Therefore, moving forward with the intent of generating a photonic circuit layout, bend radius of $100\mu\text{m}$ will be considered appropriate.

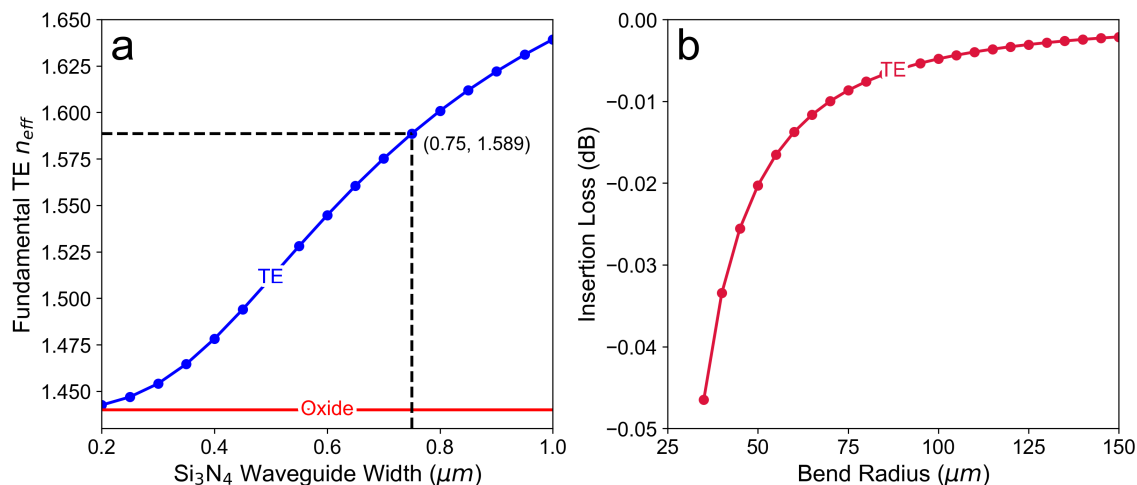


Figure 5.10: Optical characteristics of silicon nitride waveguides offered by the ANT process design kit. a.) the effective index for the fundamental TE polarization mode for various waveguide width dimensions compared to oxide refractive index baseline. b.) the insertion loss associated with a 90-degree bend considering interface mode mismatch and propagation loss for various bend radii for the chosen waveguide dimensions of $400\text{nm} \times 750\text{nm}$.

Based on the metamaterial design concepts established in the previous section, the same grating geometries are implemented for the new waveguide dimensions. The change in dimensions for the waveguide width from $8\mu\text{m}$ down to 750nm alter the geometric resonant conditions for the nanostructured phase-change chalcogenide metasurface. Previously, longitudinal dielectric resonant modes are generated within the PCM metasurface leading to the observed multi-spectral resonances; however, with

the reduction in waveguide dimensions this mode is no longer possible as nanostructured gratings oriented along the propagation direction would have subwavelength geometries constituting only an effective medium response. Therefore, to generate a similar dielectric resonant mode a rotated grating structure is explored as illustrated in Figure 5.11. The overall spectral response is dictated by several design parameters including buffer material choice and thickness, PCM thickness, grating period, and corresponding slot widths as indicated on the right-hand side of the schematic.

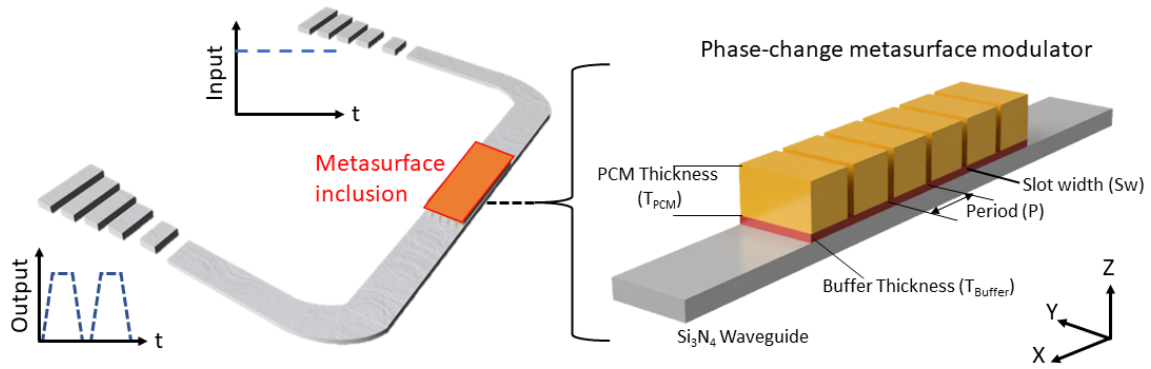


Figure 5.11: Schematic of the proposed chalcogenide phase-change intensity modulator based on silicon nitride waveguide platform (left) and close up of the metasurface device defined by physical dimensions such as buffer thickness, PCM thickness, period, and slot width (right).

Modelling and simulations for the device were carried out in Lumerical 3D FDTD. Silicon dioxide was used to model the insulating substrate layer and the ANT specific silicon nitride waveguide was modelled on top. A fully vectorial three-dimensional FDTD region was instantiated with the background index set to that of the silicon dioxide material to represent oxide cladding for the waveguide which is consistent with the fabrication process provided by ANT. All boundary conditions for the FDTD region consisted of perfectly matched layers (PML) to absorb scattered

fields associated with the inclusion of the GST metasurface grating to prevent erroneous simulation results. Placement of the PML boundaries to avoid perturbing the waveguide mode was determined by sweeping the span of the simulation region and monitoring the convergence of the effective index of the silicon nitride waveguide to a singular value. For the specified dimensions of the ANT SiN platform, a simulation span of $5 \times 5 \mu m$ is sufficient. Port objects are utilized as both a source object to generate the guided optical mode, and a monitor object to collect the spectral response for the given mode. Finally, field and index monitors are placed in the XZ plane to collect electric field data which can be extracted and plotted in either MATLAB or Python.

Previous GST based metamaterial grating modulator demonstration highlighted the markedly different spectral response across the two material phases of amorphous and crystalline; however, the actuation mechanism to achieve a phase transition in GST would need to be from an external source. Prior literature has presented diverse range of possible switching mechanisms including external train of femtosecond pulse laser excitations, electrical switching, and various thermal switching approaches for planar metasurfaces or integrated photonic circuit components [110–115]. Metallic micro-heaters are an established switching mechanism in conventional silicon photonic circuits, serving as both actuation for modulation and compensation for tuning micro-ring resonator devices [56, 116]. Due to the ohmic losses associated with the induced plasmonic interactions between the evanescent electric field of the propagating waveguide mode and the metallic heater element, micro-heaters are often placed above the silicon waveguide separated by a considerable layer of silicon dioxide to ensure low insertion losses. The micrometer thick silicon dioxide layer poses a signif-

ican thermal insulator for the micro-heater, resulting in a relatively large thermal response time for the heat to propagate down to the silicon waveguide. The temperatures required to reach amorphization (600°C) and crystallization (160°C) for a given GST-based photonic device will result in switching times in the range of micro to milliseconds which will limit the usability of the device for high-speed applications. Therefore, to address the large thermal time constant issue, the micro-heater element needs to be placed adjacent to the GST layer to avoid thermal propagation through silicon dioxide. Transparent conductive oxides (TCOs) are materials that can conduct current but are optically transparent, making them the ideal candidate for implementing a low loss micro-heater in the vicinity of the waveguide structure. A comparison study was conducted to understand the influence of the inclusion of an ITO (indium tin oxide) layer with the GST metasurface grating structure. The spectral response was generated and plotted in Figure 5.12a for an amorphous GST meta-grating configuration with thickness of 700nm , a length along the propagation direction of $5\mu\text{m}$, a duty cycle (ratio of GST grating length to the period of the unit cell) and a period of 850nm . Without an ITO layer, the adjacent GST meta-grating is positioned directly above the waveguide where the modes are perturbed, leading to mostly optical scattering and a depreciable resonant mode centered at $\lambda = 1580\text{nm}$ as shown in red. The addition of a 100nm thick ITO layer between the top of the silicon nitride waveguide and the bottom of the GST meta-grating simultaneously increases the overall transmission of the spectral response and elicits a stronger more defined resonance centered at $\lambda = 1560\text{nm}$. The physical separation between the meta-grating and the main waveguide permits a greater field distribution in the GST layer in both X and Z directions, as shown in Figure 5.12c, where a

mixed standing wave pattern is present. Corroborated by the significant difference in the electric field intensities at the waveguide output towards the positive X direction, the on ($\lambda = 1560nm$) and off ($\lambda = 1515nm$) resonance behaviour corresponds to a transmission contrast of over 30%.

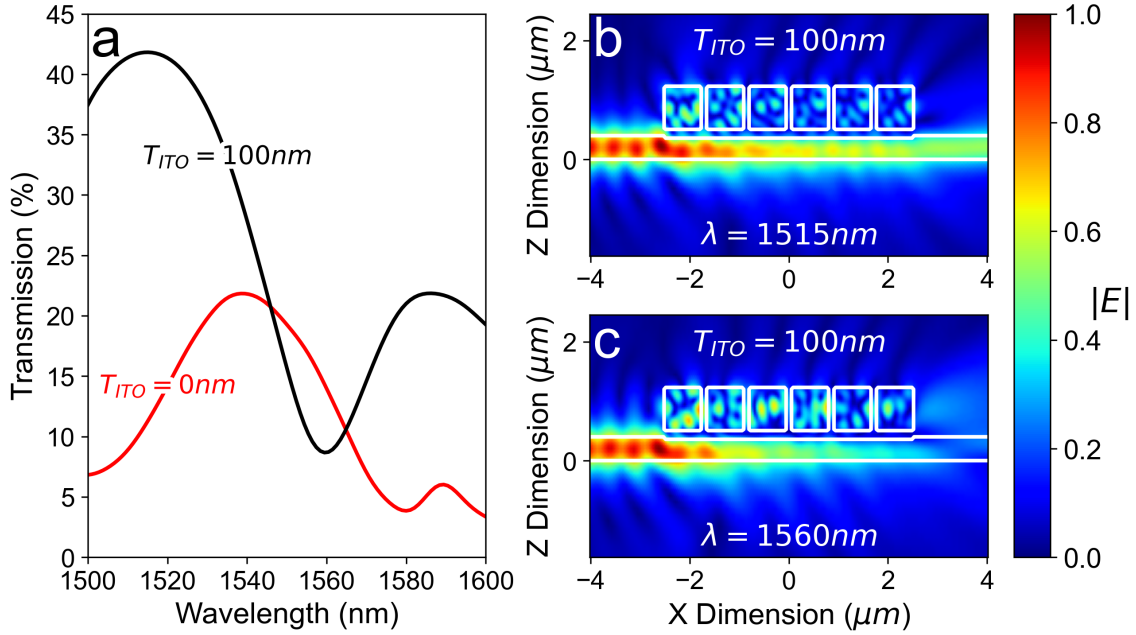


Figure 5.12: The metamaterial resonant behaviour with and without the inclusion of a 100nm thick ITO buffer layer. a.) overall spectrum for both configurations within the range of 1500 – 1600nm. b.) electric field intensity of the waveguide mode interaction with GST grating metasurface separated by 100nm of ITO at 1515nm. c.) electric field intensity of the waveguide mode interaction with GST grating metasurface separated by 100nm of ITO at 1560nm.

Once the field interactions for the amorphous GST meta-grating is understood, the crystalline phase is modelled and simulated. Figure 5.13a demonstrate the drastic change in optical response between the two material phases. The high refractive index of crystalline GST, within the telecommunications C-band range, do not permit the

coupling of waveguide modes into the meta-grating structure and thus produces a flat transmission spectral response across the wavelength ranges of $1500\text{nm} - 1600\text{nm}$. Comparing the electric field intensities across amorphous and crystalline phases at the same spectral location of $\lambda = 1560\text{nm}$, Figure 5.13b,c show coupling of the waveguide mode and no significant interaction respectively. The distinctly different interaction between the amorphous and crystalline phases for GST demonstrates the viability of such an integrated component platform to realize reconfigurable and non-volatile intensity modulators within a photonic circuit.

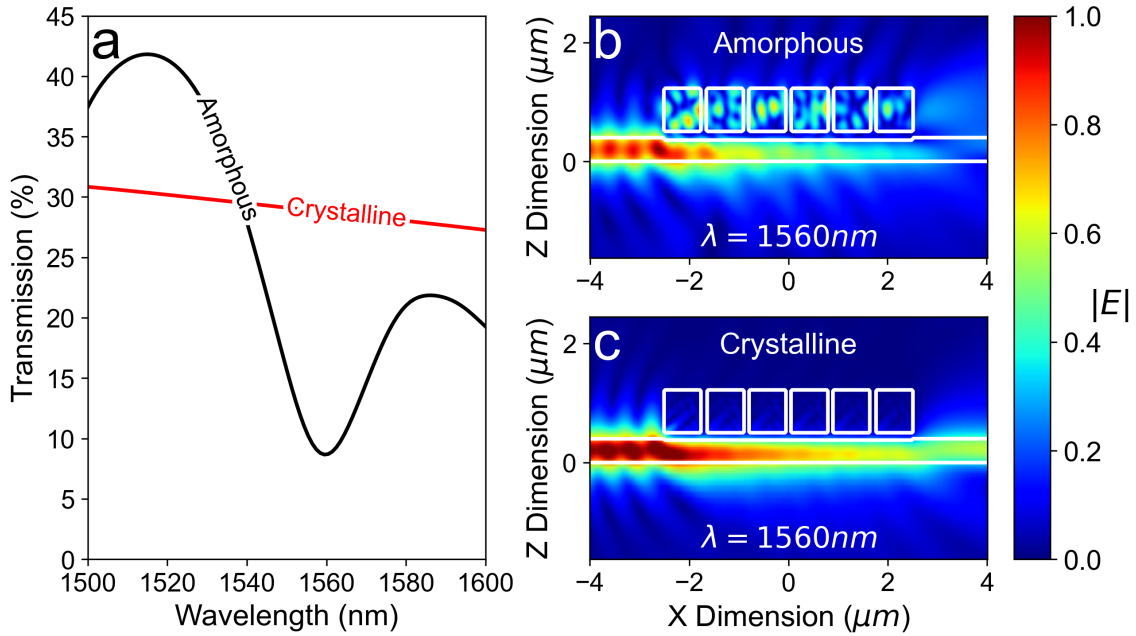


Figure 5.13: Comparison across the two spectral response generated from crystalline and amorphous phases. a.) transmission for amorphous (black) and crystalline (red) GST. b.) electric field intensity of the GST meta-grating in amorphous phase. c.) electric field intensity of the GST meta-grating in crystalline phase.

The metamaterial design approach for the integration of GST material on pho-

tonic waveguides offers several parameters to adjust and tune the spectral resonance to target the desired frequency channels. The period and the duty cycle of the meta-grating geometry offers such degrees of freedom to shift the spectral response for amorphous GST with little to no changes to the overall response shape and profile. Figure 5.14a show the translation of the spectral plot with the resonance centered at $1540nm$ for a period of $820nm$ shifted to $1560nm$ for a period of $850nm$ for a constant duty cycle of 0.847 . The change in the physical geometry of the resonant metamaterial allows for either longer or shorter wavelengths to establish a distributed resonant mode corresponding to a larger or smaller nanostructure. The $30nm$ dimensional change in period which produces a $20nm$ shift in spectra, resulting in a resolution of 1.5 . In contrast, Figure 5.14b illustrates the high sensitivity of the GST meta-grating structure to changes in duty cycle. A set of transmission spectra is plotted for a series of duty cycles incrementing at 0.02 with the period fixed at $850nm$. It is observed that a change in duty cycle of 0.08 , results in a shift of $40nm$.

Although transparent conductive oxides, such as ITO, are an ideal candidate for the implementation of a non-intrusive micro-heater for photonic waveguides, the electrical conducting properties of this class of materials translates to a high optical extinction coefficient. To explore low insertion loss alternatives for the GST meta-grating modulator, the ITO layer is replaced with a silicon oxide buffer layer. Figure 5.15a displays a series of transmission spectra showing lower insertion losses across the wavelength range than previous demonstrations and exhibiting the same resonance tunability with changes in the period. Here, a $30nm$ change in period results in a $24nm$ shift in the spectral position of the meta-grating resonance. Figure 5.15b illustrates the on-resonance ($\lambda = 1555nm$) electric field intensity for the

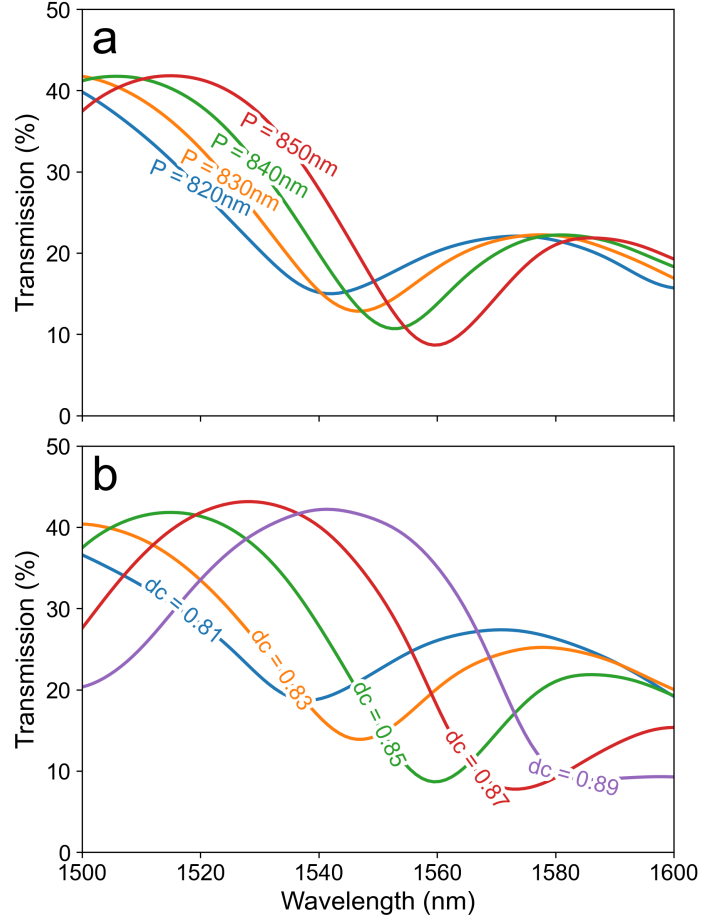


Figure 5.14: Resonance tuning of the GST meta-grating modulator by adjusting a.) period and b.) duty cycle

amorphous GST meta-grating, with a period of 850nm. The waveguide modal field efficiently couples into the meta-grating nanostructure, generating a uniform resonant field distribution consisting of a high order spatial mode with three distinct maxima in both X and Z directions. This is mostly evident in the first two GST grating bars as the field propagates from the negative to the positive X direction. Due to the extinction coefficient of GST within these wavelength ranges, the intensity

of the electric field diminishes along the length of the meta-grating. Nevertheless, the non-volatile reconfigurable resonant properties offered by this GST meta-grating device demonstrate a unique approach for implementing synaptic weighting elements for the realization of wavelength – division multiplexing (WDM) for applications in computational photonics.

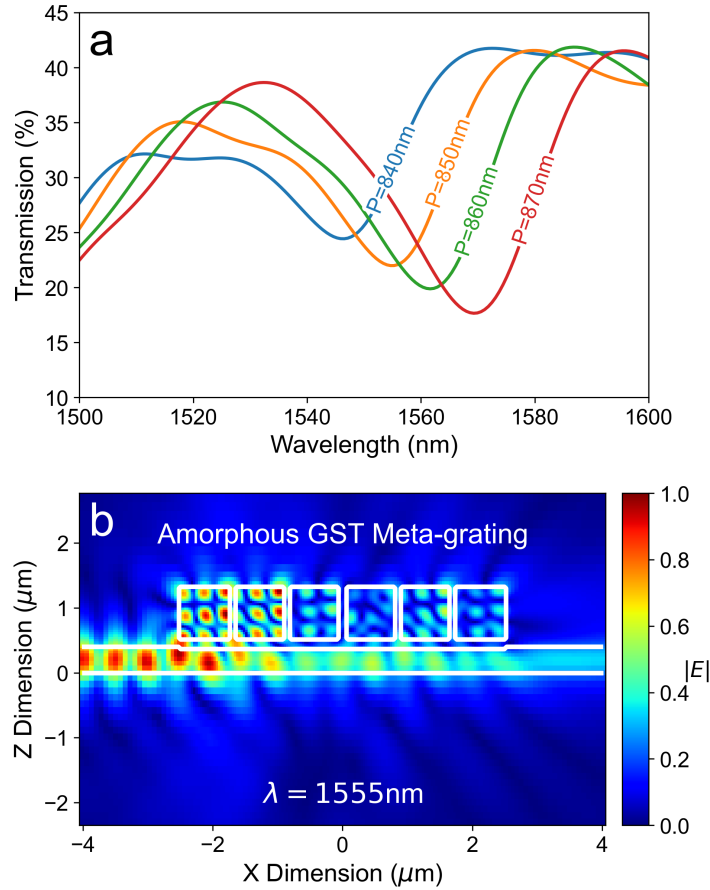


Figure 5.15: Spectral response of GST meta-grating with the inclusion of silicon dioxide as buffer layer material. a.) resonance tuning by adjusting period of the meta-grating structure. b.) electric field intensity of amorphous GST meta-grating with structure outline showing resonance centered at $\lambda = 1555\text{nm}$, for a period of 850nm.

By leveraging metamaterial design principles, for example by of changing grating periodicity to address and target specific operating wavelengths, coupled with the hysteresis properties of phase-change chalcogenide GST, both positive and negative synaptic weighting values are realizable. Figure 5.16 compares the overall transmission spectrum for two periods 850nm (black) and 880nm (red) in both amorphous (solid lines) and crystalline phases (dashed lines). By shifting the resonant response of the GST meta-grating such that the high transmission region of the newly shifted spectrum aligns with the low transmission of the resonant region of the previous spectrum (indicated by the blue arrow), two distinct intensity levels are attainable. Comparing the electric field intensities at the same spectral location of $\lambda = 1575nm$ across periods of 850nm and 880nm in Figure 5.17 (left and right panels respectively), a distinguishable difference is noticeable between on and off resonance. The on-resonance mode within the GST meta-grating is uniformly distributed—establishing clear electric field maxima and minima—ultimately absorbing the incoming propagating signal creating a decrease in transmission. In contrast, the off-resonance mode at $\lambda = 1575nm$ for the period of 850nm display a chaotic mix of field intensities inside the GST meta-grating with some scattering but no major decrease in transmission. Since the crystalline response produces a flat transmission profile (indicative of the lack of coupling and interaction with the meta-grating as illustrated in the middle panel of Figure 5.17) over the entire spectral range, irrespective of the period of the GST meta-grating, it establishes an optical intensity baseline or reference value. Therefore, if two GST meta-grating devices of different periods are incorporated on the same bus waveguide within a WDM based photonic computing network, then based on the material phase of GST positive, negative or neutral values in the form

of transmission can be encoded.

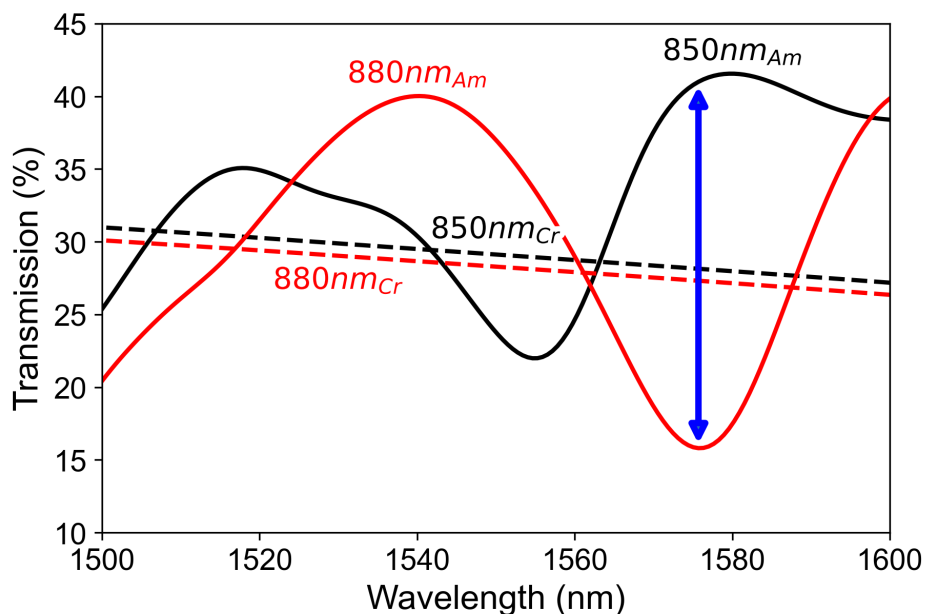


Figure 5.16: Comparison of spectral response for two periods at 850nm (black) and 880nm (red) for both amorphous and crystalline phases, represented by solid and dashed lines respectively. Blue arrow indicated the transmission contrast achievable for a shifted resonance spectrum

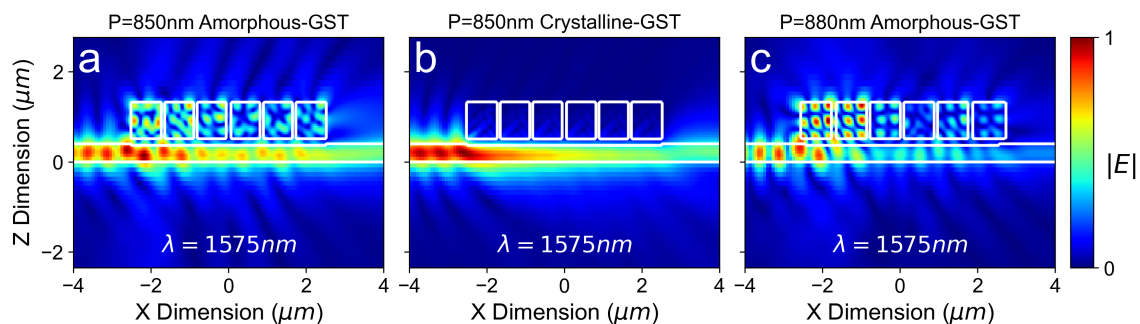


Figure 5.17: Electric field intensity distribution between the waveguide and the GST meta-grating structure with a period of 850nm for a.) amorphous, b.) crystalline GST and contrasted with a shifted response for amorphous GST with period of 880nm

Favourable resonant conditions for the GST meta-grating, as previously demonstrated, are obtained for grating lengths of 6 GST blocks. Sample simulations are performed to analyze the influence of grating lengths on the overall spectrum; however, it was found that any deviations from this geometry resulted in weak mode coupling and chaotic field distributions within the GST blocks. Long meta-gratings lead to increased insertion losses as the extinction coefficient of GST absorb the propagating optical signal, while short grating lengths lead to increases in overall scattering without a clearly confined resonant mode. However, at the limit of a single GST block—or meta-atom—configuration, significant field coupling is observed for the amorphous phase and the same flat high transmission response is observed for the crystalline phase. Figure 5.18a show the markedly different response between the amorphous and crystalline phases (for a GST meta-atom with a thickness of 620nm and a length of 745nm); where the on-resonance transmission is 42%, while the off resonance is as high as 81%. The crystalline spectrum is nearly constant at 82% across the entire wavelength range from 1500nm to 1600nm. When examining the electric field intensity for the amorphous phase, a clear distinguishable resonant mode—resembling that of a whispering gallery mode—can be identified in Figure 5.18b. Strong field coupling from the bus waveguide to the amorphous GST meta-atom results in weak field intensities at the output corresponding to the decrease in transmission at $\lambda = 1565nm$. The opposite effect is observed in the crystalline phase (Figure 5.18c), where weak field coupling results in the confined waveguide mode to propagate unperturbed to the output.

Deviating away from conventional metamaterial design principles, changing the period or duty cycle is no longer possible; however, spectral tuning for the meta-atom

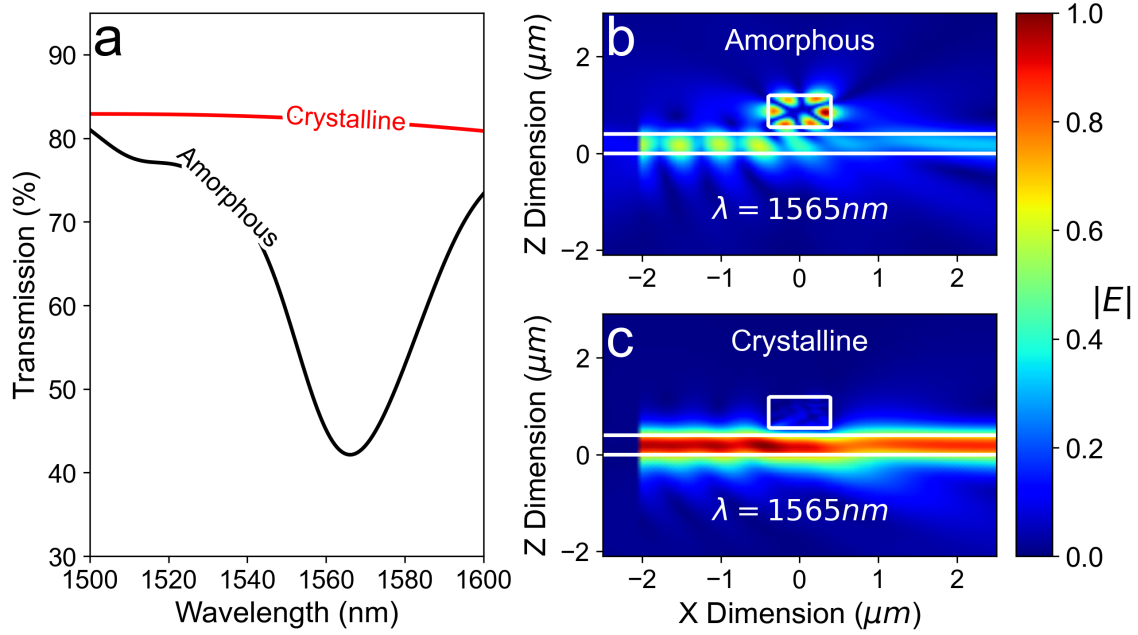


Figure 5.18: a.) spectral response for the GST meta-atom micro-block resonator in amorphous (black) and crystalline (red) material phase, b.) electric field intensity of the resonant coupling within amorphous GST meta-atom, c.) electric field intensity demonstrating the absence of resonant coupling within crystalline GST meta-atom.

nanostructure is still possible by adjusting the physical dimensions of the GST block itself. If the width (span in Y dimension) of the GST meta-atom is held constant to be the same width as the waveguide, then the thickness (span in the Z dimension) and length (span in the X dimension) can be altered to shift the spectral resonance to the desired wavelength of interest. Figure 5.19 show spectral shifting of the meta-atom resonance with two approaches: changes in thickness and length in panel a and b respectively. Between both dimensional tuning, the same trend is observed; when the meta-atom is enlarged, the spectrum red-shifts as longer wavelengths satisfy the resonant condition, while smaller dimensions result in the blue-shift of the spectrum

as shorter wavelengths then meet the resonant condition.

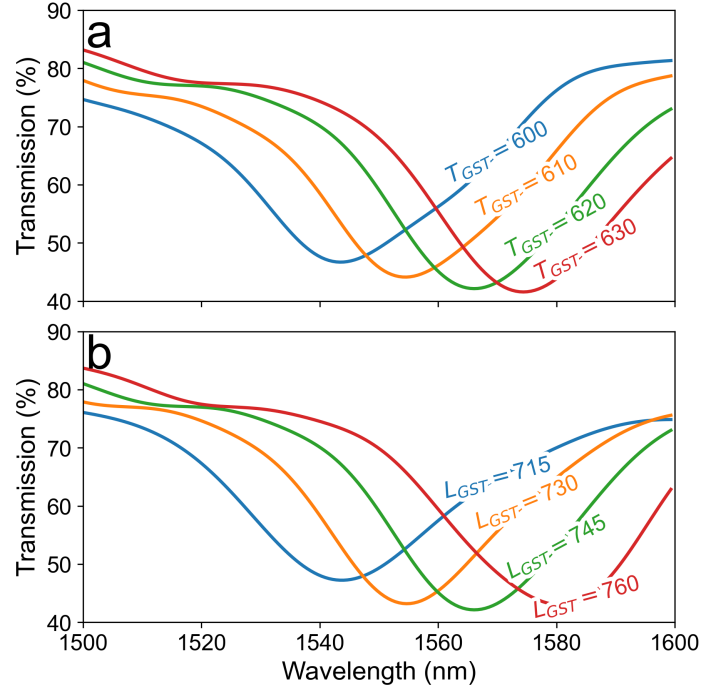


Figure 5.19: Resonance tuning of the GST meta-atom block by adjusting parameters such as a.) thickness and b.) length dimensions.

Continuing to leverage the low loss coupling between the bus waveguide and the GST meta-atom, provided by the silicon oxide buffer layer, an alternative unintrusive integrated thermal actuation solution was subsequently explored. Thermal investigations, using COMSOL multiphysics simulations, confirmed that the micro-heating element must be placed adjacent to the GST material to achieve sub-microsecond switching performance. However, from previous simulation analysis, it was demonstrated that the inclusion of an ITO as a buffer layer between the bus waveguide and the GST material generated high insertion losses. Therefore, two alternative ITO configurations were explored consisting of a top position, located directly above

the GST meta-atom and an off-centre position corresponding to an electric field intensity minimum associated with the spatial distribution of the resonant mode. From Figure 5.20a, it is observed that the overall spectral profile between the two configurations: top and buried, are nearly identical; however, the top position produces a resonance that is blue shifted relative to the buried position centered at $\lambda = 1555nm$. The electric field intensity maps of the buried configuration, from Figure 5.20b, show that the quasi-whispering gallery modes traversing the periphery of the GST meta-atom block is unperturbed by the addition of the ITO micro-heater at the field minima position; however, Figure 5.20c displaying the top configuration illustrate a clear disruption in the resonant mode distribution. Intense field localization only fills a portion of the GST meta-atom volume, which can be interpreted as a reduction in the physical geometry of the nanostructure; thus, corresponding to a spectral blue-shift.

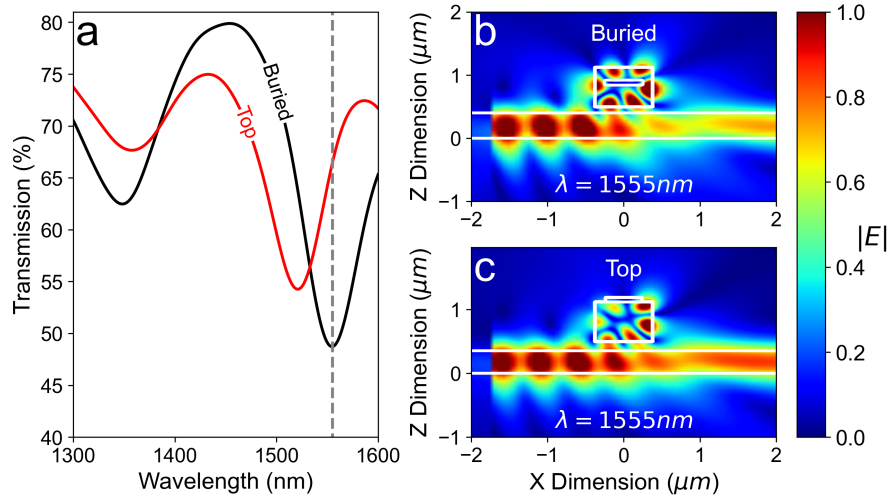


Figure 5.20: a.) Spectral response of the buried (black) and top (red) configuration for the placement of ITO micro-heater component, b.) electric field intensity showing the buried configuration, c.) electric field intensity showing the top configuration.

5.3 Addition of effective medium based PCM meta-material on integrated photonic waveguides for dispersion engineering

Reconfigurable resonant GST meta-grating and meta-atom, with tunable spectral response across the telecommunication bands and a non-disruptive approach to integrate micro-heater elements, demonstrated a promising approach to implement fast-switching, non-volatile and power efficient intensity modulators. However, device fabrication and cyclability or endurance present two main engineering challenges that hinder the usability of such device. The high aspect ratio dimensions (GST thickness is higher than the width of individual grating widths) of the meta-grating enforce the use of either a highly anisotropic etching process, or an efficient photo-resist lift-off process. Existing lift-off recipes available at the UofA NanoFAB, employing the use of positive photoresists, require a thickness ratio of (3:1) between the resist layer and the thin film. Therefore, given the 700nm thickness of GST for the previous meta-grating or meta-atom configurations, a photoresist thickness of nearly $2.1\mu\text{m}$ would be required. At such extreme thicknesses, the lift-off photoresist becomes mechanically unstable as the underlying layer of the bilayer composite collapses—leading to unreliable lift-off performance and possible delamination. To circumvent this issue, one could subdivide the total GST layer into many 100nm – 200nm layers; however, the series of deposition and lift-off steps would require several alignment procedures. Considering alignment tolerances of available lithography instruments offered at the NanoFAB, misaligned layer could have a detrimental effect on the overall spectral resonance. Furthermore, a dry etching approach is also

unavailable due to unproven chemical recipes that are unreliable for high anisotropic etching of chalcogenide phase-change materials.

Upon switching the chalcogenide phase-change material between the amorphous and crystalline states, the optical and electrical properties of the material drastically change due to significant changes in the atomic arrangement. Repeated amorphization and crystallization cycles induce stoichiometric changes to the material and therefore changes to the optical and electrical properties. One of the most prominent alterations is in the form of oxidation. For example, ambient oxidation of GST will lead to stoichiometric imbalances with significantly more germanium and selenium oxides than tellurium oxides. Under the influence of extended switching cycles, the presence of different oxidized compounds with varying material properties leads to the breakdown of the phase-change material itself. Dissimilar melting points of oxide compounds lead to the separation of phases upon a melt-quench process. As the separated phases aggregate and coalesce, the different thermal expansion coefficients among constituent phases lead to void formation along grain boundaries. Over an extended period of thermal cycles, void growth ultimately leads to delamination and non-uniformity throughout the phase-change material.

Atomic migration leading to changes in stoichiometry result in both mechanical and material failure; culminating in a phase-change material that can no longer be reliably switched between amorphous and crystalline states. Prolonged switching endurance and device cyclability can be improved by using less PCM volume. The integration of thin film PCM in a compact footprint can help maintain thermal uniformity during a phase switch event and decrease the likelihood of phase segregation. The decreased switching energies required for actuating a phase transition also means

shortened duration in which the material is held at elevated amorphization temperatures; therefore, leading to decreased risk of oxidation, and atomic migration. One ramification for the inclusion of thinner phase-change materials ($< 100nm$) is the inability to hold an optical resonance as the dimensions are too small to meet the resonant criteria. Instead, a reconfigurable phase-change non-resonant metasurface incorporated into an interferometer circuit design, such as a Mach Zehnder Interferometer, can act as a tunable phase-shifter. By leveraging metamaterial effective medium theory, desired material dispersion profiles are realizable by adjusting the ratio of subwavelength nanoscale inclusions of the constituent host materials. Figure 5.21 show a cartoon schematic of the proposed device platform. A section of a waveguide is integrated with the PCM metasurface phase-shifter and result in the accumulation of phase for an input signal and generate a spectral shift such that the new spectra maxima is positioned at the prior spectra minima. Key design parameters for such a configuration include the integrated PCM thin film thickness, the overall patch length, width of the PCM section and period of the grating structure. At highly subwavelength dimensions, below the Bloch mode condition, the overall effective index of the metasurface grating can be calculated by the Rytov approximation [117]:

$$(n_{am})^2 = \frac{W_{pcm}}{period}(n_{eff\ am})^2 + \left(1 - \frac{W_{pcm}}{period}\right) (n_{eff\ adj})^2 \quad (5.3)$$

$$(n_{cr})^2 = \frac{W_{pcm}}{period}(n_{eff\ cr})^2 + \left(1 - \frac{W_{pcm}}{period}\right) (n_{eff\ adj})^2 \quad (5.4)$$

Where W_{pcm} is the width of the PCM grating as indicated on the schematic in Figure 5.21, $n_{eff\ am}$ is the effective index of the mode under analysis for the waveguide

with the inclusion of PCM in the amorphous phase, $n_{eff\ cr}$ is the respective effective index value for the crystalline phase, and $n_{eff\ adj}$ is the respective effective index value of the adjacent material. The ratio of W_{pcm} and Period (P) is also referred to as the duty cycle or $dc = \frac{W_{pcm}}{period}$.

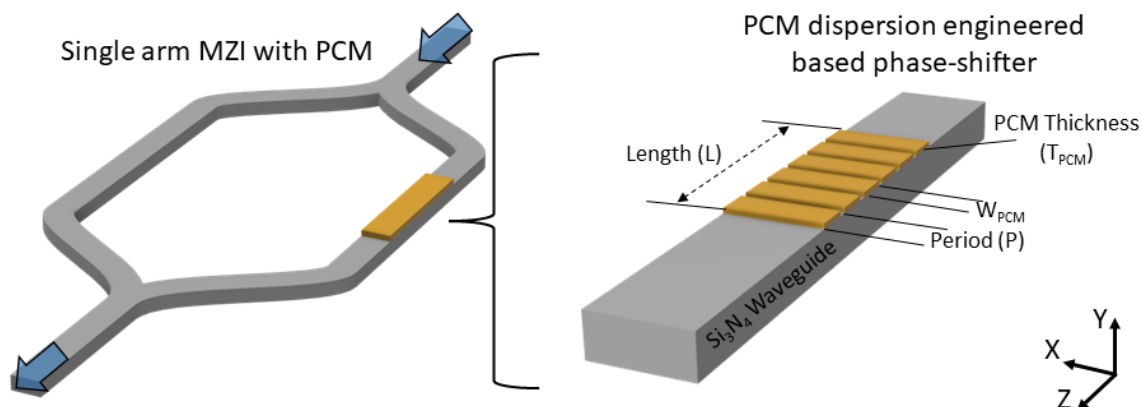


Figure 5.21: Schematic of a Mach Zehnder Interferometer (MZI) circuit (left) with the incorporation of a non-resonant metasurface phase-change material for a dispersion engineered phase response (right).

The effective indices of the amorphous, crystalline, and adjacent material on the silicon nitride waveguide platform were calculated using Lumerical MODE solutions finite difference eigenmode (FDE) solver. As a two-dimensional solver, FDE calculates all possible propagation modes given the spatial distribution of the refractive index. As shown in the schematic in Figure 5.21, a cross-sectional representation, in the XY plane, of the waveguide was modelled. The silicon nitride waveguide consisted of a thickness of 400nm (y direction) and a width of 750nm (x direction) that was surrounded by silicon dioxide—serving as both the substrate and cladding material. The FDE solver region is positioned for the waveguide to be at the centre of the simulation. To verify the results calculated by the eigenmode solver, convergence

testing was performed by sweeping the simulation span region and determining the appropriate length that resulted in the effective index value to converge to the same value. The span of the FDE solver region was determined to be $3\mu m$ in both the y and x directions. Subsequently, the effective index for the fundamental TE mode, at the center wavelength of 1500nm, was calculated for the oxide cladded silicon nitride waveguide and the GST thin film (20nm) loaded waveguide. A frequency sweep was performed for the selected fundamental TE mode between the wavelength ranges of 1500nm to 1600nm and the resulting effective index data was extracted. With the effective index values and for a series of duty cycles ranging between zero (purely oxide) and one (purely GST), the metasurface effective index values were determined for amorphous and crystalline states represented in Figure 5.22a and b respectively. Across both plots, the effective index is large for short wavelengths and small for longer wavelengths. Represented by color, the effective index values span a significant range of values from 1.58 – 1.66 in amorphous phase and 1.6 – 2.0 in the crystalline phase; thereby, demonstrating the versatility of a metamaterial effective medium approach.

Within the context of a photonic interferometer circuit, the effective index difference is a key parameter to determining the patch length required to achieve a desired phase shift. Plotted in the colormap of Figure 5.23, is the effective index difference (across crystalline and amorphous phases) variation as functions of duty cycle and wavelength. Small duty cycle ratios corresponding to less GST inclusions resulted in smaller effective index changes, while large duty cycle ratios result in larger effective index changes. Focusing on the center wavelength of 1550nm, the effective index is plotted against duty cycle to illustrate this trend in panel b of Figure 5.23.

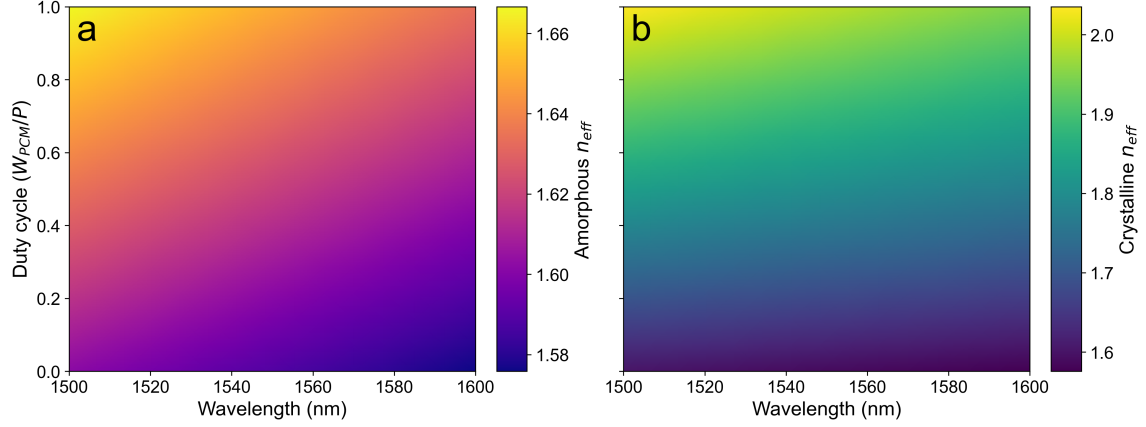


Figure 5.22: The achieved effective index variations, represented by color, for various duty cycles for a GST and silicon dioxide material pair across the telecom C-band spectrum in a.) amorphous phase and b.) crystalline phase.

From the plot of Figure 5.23a a duty cycle of 0.5 yields an effective index difference of 0.182. At this effective index difference value, the optical phase difference $\Delta\theta$ is calculated for a series of metasurface patch length values from $0\mu m$ to $10\mu m$ with the following formula:

$$\Delta\theta = \frac{2\pi\Delta n_{eff}L}{\lambda_c} \quad (5.5)$$

Where λ_c , the center wavelength is chosen to be 1550nm. Plotted in Figure 5.24a, is the phase difference for a given metasurface patch length bounded between 0 and π radians. As shown in the plot, the shortest patch length to achieve a π phase shift or L_π is determined to be $4.27\mu m$ for an unbalanced MZI with the integration of the metasurface GST phase-shifter on one arm. Figure 5.24b exemplifies the spectral shift achieved across the amorphous and crystalline states for a sample MZI with a free-spectral range of 5nm and an unbalanced arm length of $238\mu m$. As illustrated,

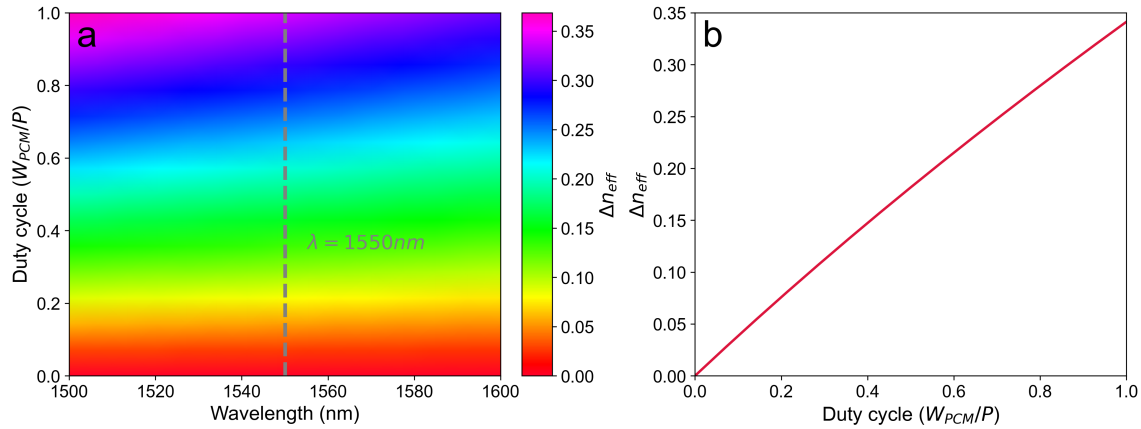


Figure 5.23: a.) The effective index difference between amorphous and crystalline phases, represented as color, for a range of duty cycles. b.) The effective index difference as a function of increasing duty cycle at a singular wavelength of 1550nm.

only for a phase difference of π , can the spectral response of an MZI be shifted such that the maxima will line up to previous minima and thereby generating an extinction ratio (transmission contrast) over 30dB.

Once again by leveraging the favourable thermo-conductive properties of ITO and implementing it as a near-adjacent micro-heater, a new stratified configuration of GST and ITO was considered. Similarly, ITO of 20nm thickness positioned on top of the silicon nitride waveguide was modelled in FDE and the effective index of the fundamental TE mode across 1500-1600nm was extracted. Figure 5.25a show the possible range of effective index difference values, presented as color, exhibit a nearly identical range to that of the GST and oxide combination (0 – 0.35). Although the refractive index of ITO material is relatively low in the near-infrared spectral band, the same effective index difference values can be obtained through the effective medium dispersion method. Taken into consideration the resolution limit of typical lithography tools available here at the NanoFAB, for example the RAITH TWO

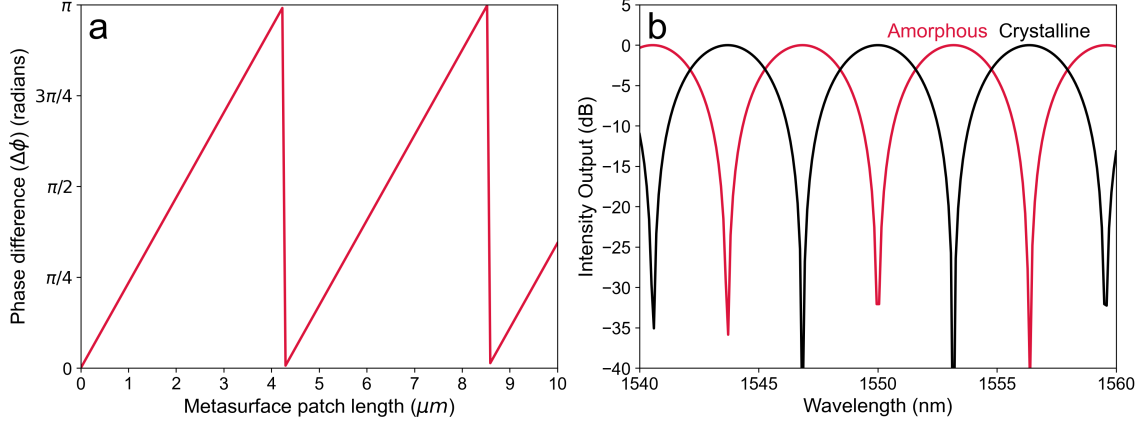


Figure 5.24: GST metasurface phase-shifter integration on a single arm MZI configuration; a.) the calculated phase difference between amorphous and crystalline states for various patch lengths to determine minimum length required to achieve π phase shift, b.) overall spectral response from the MZI GST metasurface phase-shifter for amorphous (red) and crystalline (black) phases.

30kV electron beam lithography system, then not all duty cycle values are realizable. If a minimum resolution of 100nm is set, then the smallest and largest duty cycle values which adhere to these dimensional specifications correspond to 0.357 ($W_{pcm} = 107nm$) and 0.643 ($W_{pcm} = 193nm$) if a period of 300nm is assumed. Plotted in Figure 5.25b are the achievable phase differences for the two GST widths of 107nm and 193nm in black and red respectively. A width of 193nm requires a L_{π} of $3.4\mu m$ and width of 107nm requires a L_{π} of $5.8\mu m$; therefore, defining the lower and upper limit of patch length dimensions.

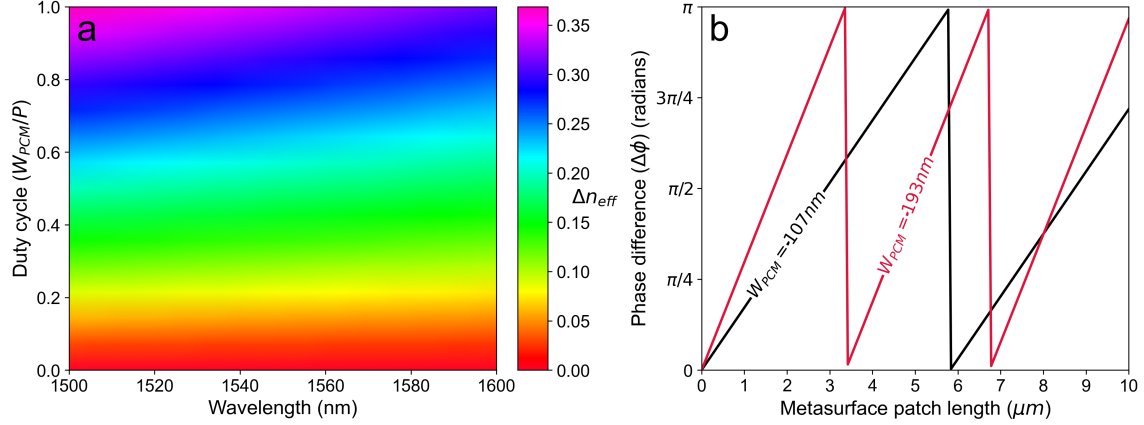


Figure 5.25: a.) Effective index difference between amorphous and crystalline phases for a GST and ITO material combination. b.) The calculated phase difference between amorphous and crystalline phases for various metasurface patch lengths for two duty cycles: $dc = 0.357$ ($W_{pcm} = 107nm$, black) and $dc = 0.643$ ($W_{pcm} = 193nm$, red).

5.4 Reconfigurable non-volatile MZI phase-shifters based on thin film Chalcogenide PCM

Programmable photonics enable the dynamic control of the path and properties of optical signals which enable flexible optical networks to adapt and deliver expanded functionalities to meet current network demands in an efficient manner. Electrically addressable tunable optical elements allow programmable photonics to support many critical applications including key developments in all – optical signal processing and computation to meet the growing demand for increased data-rates, lower latency response times, and cloud computing to accelerate processing for artificial intelligence (AI) and machine learning (ML) based programs. However, current volatile tuning methods, such as thermo-optic, carrier modulation, and electro-optic, do not scale in terms of power consumption demands required by AI algorithms and

cannot fully decouple from the use of electronic PRAM (programmable randomly addressable memory) which also translates to added complexity to accommodate for the electro-optic conversion. The pronounced contrast in electrical and optical properties between two stable material phases of amorphous and crystalline, present chalcogenide phase-change materials as a promising solution to implement an electrically addressable low static power consumption optical memory element. It has been demonstrated that weighting elements of a trained neural network can be translated into a matrix array of phase values corresponding to the phase-shifting arms of a cascaded mesh of MZI photonic circuits. Without expending additional external power to maintain the phase-shift values (for example in thermo-optic micro heater or carrier modulated PN junctions), specific chalcogenide PCMs patch dimensions can be designed to realize these phase values within a MZI network.

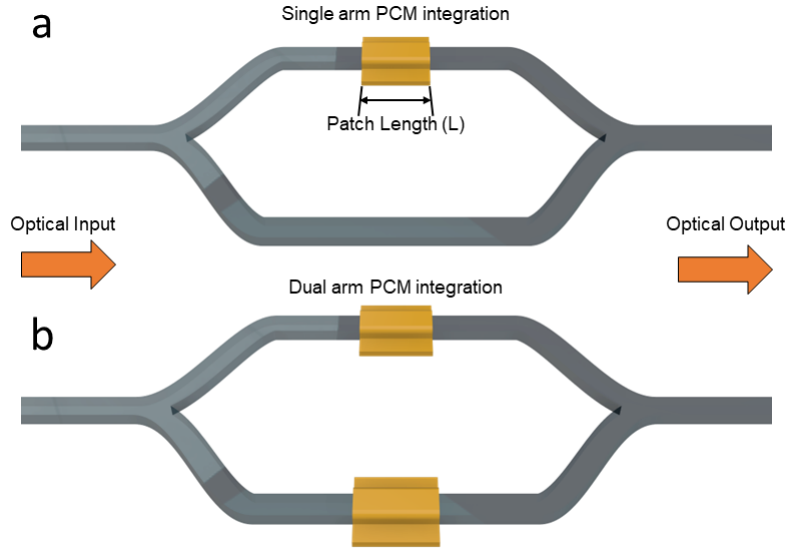


Figure 5.26: Schematic cartoon depicting the integration of chalcogenide phase-change material on MZI photonic circuits. a.) Single arm integration of PCM-based phase shifters. b.) dual arm or push-pull integration of PCM-based phase shifters.

Two main configurations are demonstrated here to illustrate signal modulation with non-volatile PCM integration in either a single or dual arm (also called push-pull) approach, as shown in Figure 5.26a,b respectively. In both configurations the incident optical signal is split equally (50:50 ratio) between two uncoupled waveguide paths with a passive y-branch component. The split signal acquires a phase difference ($\Delta\theta$) relative to each other after propagating through a certain distance and recombines with another y-branch component. Upon recombination of the two phase-shifted signals, constructive and destructive interference occur across a given spectral range. The overall optical output of the MZI can be described by the transfer function as:

$$\frac{I_{out}}{I_{in}} = \frac{1}{2} \left[1 + \cos(\beta_1 L_1 - \beta_2 L_2) \right] \quad (5.6)$$

where $\beta_{1,2}$ and $L_{1,2}$ are the propagation constants and path lengths of interference arms 1 and 2. As the equation suggests, the phase difference between the two light paths can originate from either a path length difference (ΔL), a difference in the propagation constant ($\Delta\beta$) (due to different waveguide geometries) or a combination of both. For a given MZI, the spectral distance between successive interference minima or maxima is defined as the free spectral range defined as:

$$FSR = \frac{\lambda_c^2}{\Delta L \cdot n_g} \quad (5.7)$$

where λ_c is the center wavelength, ΔL is the path length difference (moving forward will be denoted as L_{bias} , and n_g is the group index determined at the center wavelength. Departing from conventional formulations of the MZI transfer func-

tion considering volatile phase-shift modulation mechanisms, such as thermo-optic and plasma dispersion effects where a phase-shift is generated through the change in modal effective index as a result of externally applied voltage, the non-volatile properties of phase-change material physically alters the waveguiding conditions of the propagating mode and thereby generates the phase-shift across the two distinct atomic phases of amorphous and crystalline.

When considering an unbalanced MZI phase-shifter with PCM integration on a single arm, Equation (5.6) can be expanded as follows:

$$\frac{I_{out}}{I_{in}} = \frac{1}{2} \left[1 + \cos \left(\frac{2\pi\Delta n_{pcm}}{\lambda} L_{pcm} - \frac{2\pi n_{eff}}{\lambda} L_{bias} \right) \right] \quad (5.8)$$

where $\Delta n_{pcm} = n_{pcm} - n_{eff}$ is the effective index difference between a PCM loaded waveguide (n_{pcm}) in either amorphous or crystalline phase, and the default oxide cladded routing waveguide (n_{eff}) for a propagation length of L_{pcm} . Centered on a specific wavelength of operation, the series of maxima and minima generated from the spectral interference can correspond to each PCM phase. For a MZI configuration, ideally signal attenuation should be maintained to be the same across the two arms to achieve a high extinction ratio—measurement of the achievable transmission contrast between the maximum and minimum optical output. The interferometer arm loaded with the PCM patch will experience higher attenuation, especially in the crystalline phase, and result in a limited achievable minimum due to incomplete destructive interference. Therefore, to maintain high extinction ratios for a single arm PCM phase-shift MZI, the amorphous phase should generate the spectral minimum and the crystalline phase should generate the spectral maximum. Under these conditions, the arguments of the cosine in Equation (5.8) will produce a system of equations:

$$\frac{2\pi}{\lambda_c} (n_{eff} - n_{amorphous}) L_{pcm} - \frac{2\pi n_{eff}}{\lambda_c} L_{bias} = m\pi \quad (5.9)$$

$$\frac{2\pi}{\lambda_c} (n_{eff} - n_{crystalline}) L_{pcm} - \frac{2\pi n_{eff}}{\lambda_c} L_{bias} = n\pi \quad (5.10)$$

where m and n belong to the set of odd and even integers respectively. Rearranging the Equation (5.9) to solve for L_{pcm} and L_{bias} we arrive at three relations:

$$L_{pcm_single} = \frac{\lambda_c}{2(n_{crystal} - n_{amorph})} \quad (5.11)$$

$$L_{bias_single} = \left(1 - \frac{n_{amorph}}{n_{eff}}\right) L - \frac{m\lambda}{2n_{eff}} \quad (5.12)$$

$$m_{single} = \frac{n_{eff} - n_{amorph}}{n_{eff} - n_{crystal}} - \frac{2n_{eff}\lambda_c}{FSR \cdot n_g} \quad (5.13)$$

where $n-m = -1$. Through these three relations, a MZI modulator can be configured for a specified FSR that will determine the required path length difference and the respective PCM patch length to achieve a π phase-shift.

Additionally, the π phase-shift requirement can be divided between the two arms of the interferometer such that an individual arm can provide a phase shift of $\frac{\pi}{2}$ but in opposite polarity in relation to each other. This dual arm design is also known as a push-pull configuration. Assuming a symmetric integration of the PCM layer on both arms, then the effective index comparison becomes: $\Delta n_{pcm} = n_{crystalline} - n_{amorphous}$. Following the same derivation as before we arrive at three modified relations:

$$L_{pcm_{dual}} = \frac{\lambda_c}{4(n_{crystal} - n_{amorph})} \quad (5.14)$$

$$L_{bias_{dual}} = \frac{(2m + 1)\lambda_c}{4n_{eff}} \quad (5.15)$$

$$m_{dual} = \frac{2n_{eff}\lambda_c}{FSR \cdot n_g} - \frac{1}{2} \quad (5.16)$$

where $m \in integers$. A dual arm configuration reduces the PCM patch length by half compared to single arm alternative.

As described in the previous section the silicon-rich SiN_x waveguides available from Applied Nanotools are used to design the PCM phase-shifter elements of the MZI. Illustrated in the inset diagram, of Figure 5.27 is a cross sectional schematic of a PCM loaded SiN_x waveguide. Design parameters that were investigated here consist of the oxide buffer thickness separating the top of the waveguide and the PCM inclusion (d) as well as the thickness of the PCM thin film (t) itself. Comparing the four most widely used chalcogenide phase-change materials in literature (Ge-Sb-Te, Ge-Sb-Se-Te, Sb-S, and Sb-Se), Figure 5.27a plots the effective index difference between amorphous and crystalline phases for various PCM thickness separated from the waveguide by a 400nm oxide buffer. At thicknesses below 20nm, the achievable effective index values are within the same range as one another; however, when thickness are beyond 20nm, GST provides a significantly larger effective index contrast compared to the other alloys. Due to the inverse relationship of determining the patch length for a PCM phase-shift element (Equation (5.5)), the integration of GST would permit a footprint less than $10\mu m$; however, the large change in effective index is also complemented by a noticeable change in the materials extinction coefficient

and significantly increase propagation losses. For applications in telecommunications signal processing or all – optical computing, signal distortion or degradation must be avoided; therefore, maintaining low insertion losses is imperative. Material compositions such as Sb-S and Sb-Se offer a low loss alternative at the expense of a large index contrast between amorphous and crystalline phases. Deposited SbS film was characterized by variable-angle ellipsometry and fitted with a b-spline model to extract the optical parameters. These parameters were imported into Lumerical FDTD, where the simulated reflection and transmission spectra was experimentally verified. Therefore, for this demonstration SbS was chosen to realize the phase-shift element of the MZI.

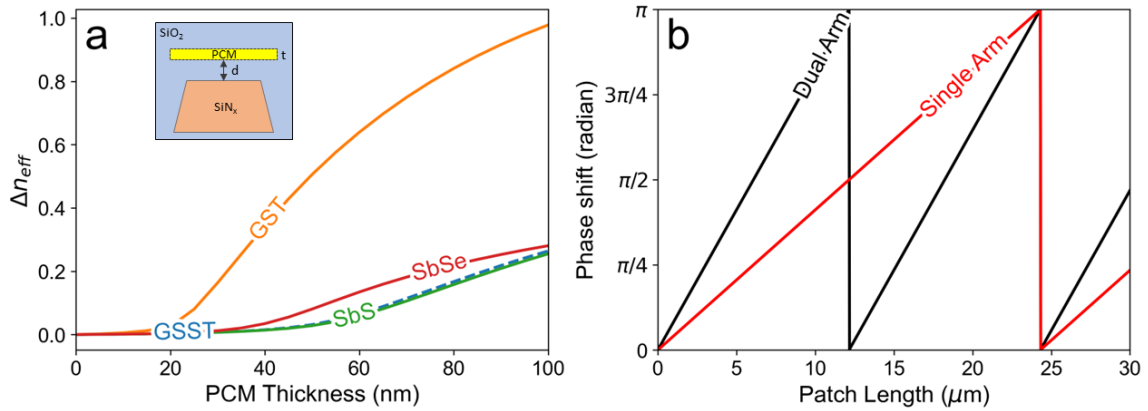


Figure 5.27: a.) The effective index difference between the amorphous and crystalline states for four different PCM alloys: Ge₂Sb₂Te₅ (orange), Ge₂Sb₂Se₄Te₁ (blue), Sb₂Se₃ (red), and Sb₂S₃ (green). Inset shows the cross-sectional silicon nitride waveguide geometry with PCM thin film integration. b.) The physical patch length difference between a single and dual arm configuration to achieve the required π phase shift.

For example, using Lumerical MODE FDE solutions a 100nm thick SbS layer was modeled on top of the SiN_x waveguide with a 400nm oxide buffer thickness

resulting in a $\Delta n_{eff} = 0.032$. Figure 5.27b plots the phase shift values relative to the Sbs patch length for both the dual arm and single arm configuration in black and red respectively. Bounded between phase shift limits of 0 and π radians, the plot demonstrates the footprint reduction by a factor of two in a dual arm configuration ($L_\pi = 12.15\mu m$) compared to a single arm design ($L_\pi = 24.3\mu m$).

Expanding on the phase-shift plot, a spatial distribution of the obtainable phase-shift values, represented as color ranging between blue (0 radians) and red (2π radians) transitioning through white (π radians), is plotted as a function of the effective index difference and the Sbs patch length for the single and dual arm configurations in Figure 5.28. The π phase shift necessary to achieve the largest extinction ratio for the MZI circuit is represented by white, where the first order π value is marked by a black line or called here the π -line. The shape of all constant phase shift values for various effective index difference and patch length value pairing demonstrates the characteristic inverse proportional relationship: as the effective index difference is increased, a shorter patch length is required for a π phase shift, while a decrease in the effective index difference necessitates a longer patch length to compensate. This relation is not only valid for PCM based MZI modulators but for any modulators and switches based on the MZI configuration. For example, the thermos-optic coefficient of silicon is $1.86 \times 10^{-4} K^{-1}$ [118] and carrier concentration changes based on externally applied bias voltage translates to an index change of around the same order of magnitude. Therefore, to achieve a full π phase shift without driving the device at exacerbated voltage levels, hundreds of micrometers to millimeter long phase shift elements are used to compensate [119–121]. Shifting along the π -line for either the single or dual arm configuration, visualizes the design trade-off between effective

index difference and the integrated SbS patch length to navigate such a design space for a PCM-based MZI phase-shifter.

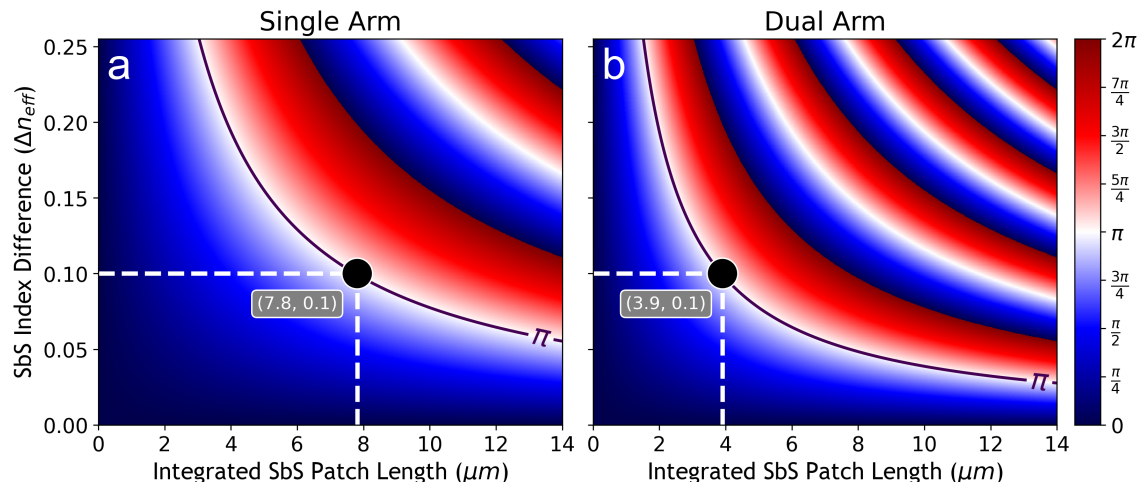


Figure 5.28: Achievable phase-difference between arms of a MZI visualized as a distribution of color based on the effective index difference and patch length for a.) single arm integration and b.) dual arm integration.

Plotted in Figure 5.29a, show the distribution of the effective index difference in relation to the two main design parameters: oxide buffer thickness and SbS thickness in the absence of an ITO layer. For example, as denoted in both panels of Figure 5.28, an effective index difference of 0.1 is required to generate a π phase shift within a patch length of $7.8\mu m$ and $3.9\mu m$ for a single and dual arm configuration respectively. Marked in the dashed cyan line, Figure 5.29a illustrate the combination of thickness values to achieve the required effective index difference. For oxide thicknesses below 200nm, the increase in SbS thickness produces a gradual increase in the effective index difference; however, beyond 200nm, the effective index difference values plateaus as the phase-change layer recedes away from the confined waveguide mode. Figure 5.29b plots the respective patch length required for a π phase shift for the same range of

thicknesses. The significant range of effective index difference values translates to a patch length stretching between orders of magnitude: from less than $10\mu m$ to over $300\mu m$. Similarly, SbS thickness parameter has a bigger impact on the patch length than the oxide buffer thickness.

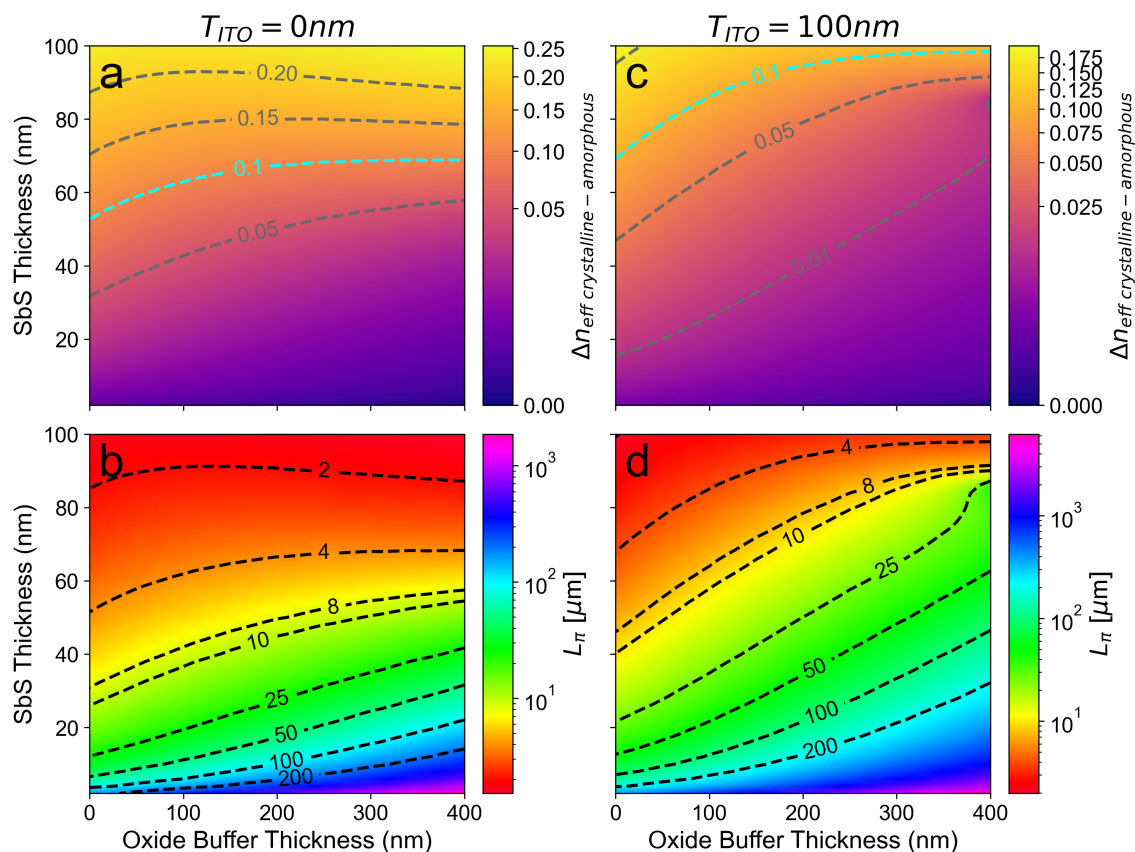


Figure 5.29: The cross-sectional parameter design space for thin film PCM integration on photonic waveguides with (c,d) and without (a,b) the inclusion of micro-heater element ITO. The first row of colormaps illustrate the achievable effective index contrast between amorphous and crystalline phases for without (a) and with 100nm of ITO (c). The second row is the associated range of patch lengths required for a π phase shift for without (b) and with 100nm of ITO (d).

Thus far, only the inclusion of a PCM layer have been considered; however, the

implementation of an integrated solution for actuating the phase switch event need to be analyzed. As mentioned in prior sections, the inclusion of a traditional metallic micro-heater is not feasible for two main reasons: speed of phase-change and thermal limitations for amorphization. The temperature distribution of a given solid medium is governed by the heat transport equation:

$$\rho c_p \frac{\partial T}{\partial t} - \nabla \cdot (k \nabla T) = Q \quad (5.17)$$

where ρ is the mass density of the material, c_p is the specific heat capacity of the medium, k is the thermal conductivity and Q is the applied heat energy transfer rate. The placement of a metallic micro-heater element will need to be positioned far away from the waveguide core to prevent excess optical losses and attenuation. However, the silicon oxide layer between the micro-heater and waveguide creates a significant thermal insulating barrier between the phase-change layer and the thermal source. Thus, elevating the phase-change layer to either crystallization ($T_g = 160^\circ\text{C}$) or amorphization ($T_g \geq 600^\circ\text{C}$) temperatures would occur on micro to millisecond time scales. Concurrently the thermal energy is not rapidly dissipated as the insulating silicon oxide material will hold onto the heat and thereby prevent sufficient quenching of the melted phase-change material in the amorphization process. To eliminate such a thermal barrier, a direct source of thermal energy should be considered.

Two main direct sources of thermal energy have been explored in literature: doped PIN junctions in silicon waveguides, and the addition of transparent conductive oxides (TCOs) in silicon nitride waveguides. TCO materials are a class of materials that exhibit both optical transparency and electrical conductivity, making them ideal for use as transparent conducting electrodes. In this demonstration, 100nm of ITO

was added on top of the SbS layer to act as a thermal source for actuating the phase change event. The ITO material properties was sampled from literature [122], which showed an epsilon near zero point in the near-infrared range centered on 1240nm. This translated to a refractive index value less than one across the telecommunication spectral range which, upon addition to the waveguide, decreased the overall effective index difference as plotted in Figure 5.29c. Compared to without ITO, the addition of ITO diminished the effective index difference values from 0 – 0.175 compared 0 – 0.25. To achieve the same 0.1 effective index difference, required a thicker SbS layer with a thinner oxide buffer layer. The addition of ITO also increased the patch length as shown in Figure 5.29d.

Visualizing the inverse relation between effective index difference and the patch length with ITO, for a π phase shift for single and dual arm integration as shown Figure 5.30 respectively, both plots demonstrate the π -line shifting to longer lengths. The same range of SbS thicknesses, now only produce an effective index difference from 0 – 0.11.

To overcome the diminished effective index values with the addition of a 100nm ITO layer, an increase in the SbS layer thickness could be considered to compensate; however, due to the high index profile of such a phase-change material, the phase-change layer itself could start to exhibit waveguiding characteristics, especially in the crystalline phase. Figure 5.31a depicts the change in the effective index difference between amorphous and crystalline phase as the SbS thickness is increased from 0 to 150nm. Two distinct regions can be differentiated as the slope of the effective index contrast line dramatically changes at a critical thickness of 86nm. Separated into single mode and hybrid mode below and above the critical thickness value re-

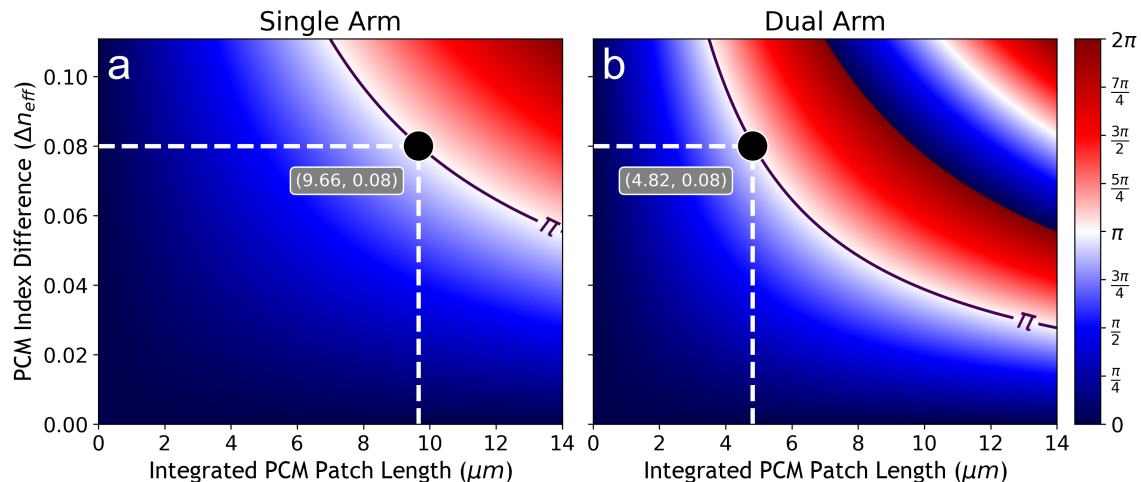


Figure 5.30: The achievable phase-difference between arms of a MZI visualized as a distribution of color based on the effective index difference and patch length with the addition of ITO for a.) single arm integration and b.) dual arm integration.

spectively, the corresponding mode distribution and waveguiding behaviour between the silicon nitride waveguide and the SbS layer are markedly different. Within the single mode region, the thickness of SbS layer perturb the fundamental TE waveguide mode causing a slight deviation in the overall modal field distribution in the amorphous and crystalline phases. In contrast, the addition of thicker SbS creates a condition for the dimensions of the phase-change layer to act as another dielectric waveguide—especially in the crystalline phase—where the silicon nitride and phase-change layer behave as a coupled waveguide system. Illustrated in Figure 5.31b-d are the corresponding x-component of the electric field modal distributions for a buffer thickness of 400nm and a SbS thickness of 86nm for one amorphous and two distinct crystalline modes. Like directional couplers, the crystalline SbS layer acts as a separate waveguide coupled to the main silicon nitride waveguide with a mode distribution similar to a super-mode. Therefore, it would be inaccurate to calcu-

late an effective index difference between a single fundamental mode and a coupled waveguide super-mode.

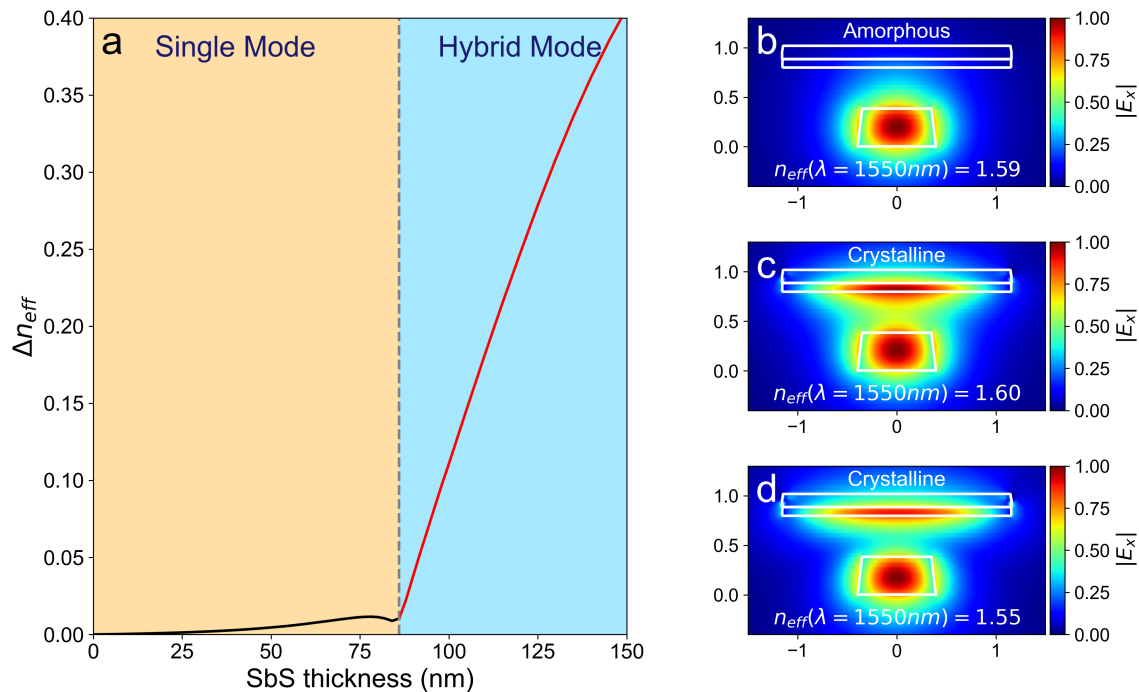


Figure 5.31: Differentiation between single mode and hybrid mode operation depending on the thickness of the integrated SbS layer; a.) plot of the effective index for SbS thickness ranging from 0-150nm with a grey dashed line demarcating the separation between single and hybrid mode operation. X-component electric field intensity distribution for SbS thickness of 86nm in b.) first mode amorphous phase, c.) first mode crystalline phase, and d.) second mode crystalline mode.

Considering the previously discussed design principles, an example calculation was performed to evaluate the spectral response of the PCM-MZI based modulator device. A waveguide cross section consisting of a 75nm SbS layer, 100nm ITO and a 400nm layer of oxide between the waveguide and PCM layer was modeled in MODE solutions and the calculated effective index difference between amorphous and crys-

talline phases is $\Delta n_{eff} = 0.0095$. Including a path length difference of $240\mu m$, the single arm and dual arm MZI response is plotted in Figure 5.32a,b respectively. The single arm configuration ($L_\pi = 81\mu m$) exhibits two modes of operation as the SbS layer can be in either the amorphous or crystalline phase; however, for the dual arm configuration ($L_\pi = 41\mu m$) if the SbS layers are addressed individually, then three distinct modes of operation exist. Here a mixed amorphous and crystalline phase between the short and long arm generate the π phased shifted spectra, but for the same phase across both interferometer arms, a third spectra is presented with an optical intensity output at 3dB centered on 1550nm. This behaviour is characteristic of a push pull configuration where the default response is optically bias at 50% while the high and low response is only $\pi/2$ phase shift away.

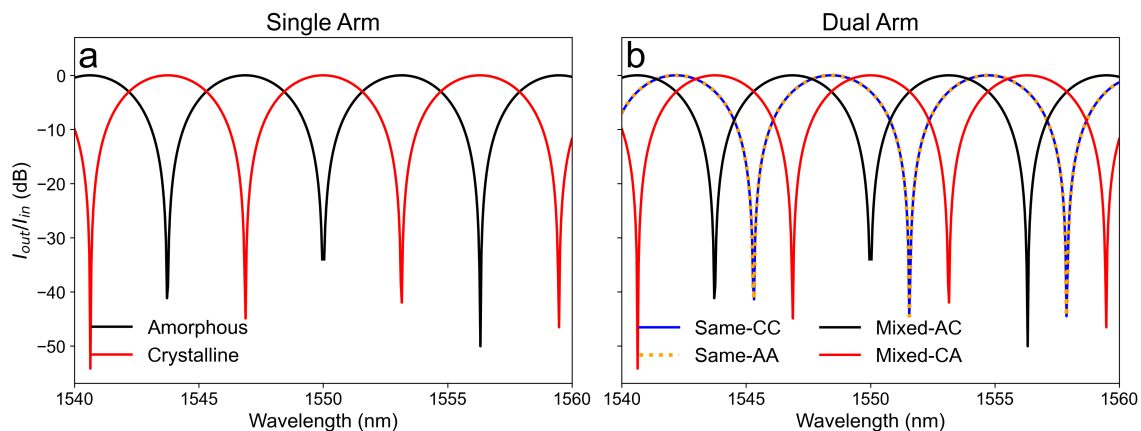


Figure 5.32: Spectral response of SbS integrated MZI photonic circuit in a.) single arm configuration and b.) dual arm configuration.

The conventional figure of merit to define a MZI – based modulator device is known as $V_\pi L[V \cdot cm]$ in units of voltage centimeters. The calculated value of a given MZI modulator relates the necessary combined voltage supplied with the length

of the actuation mechanism to achieve a full π phase shift which is the condition for maximizing the extinction ratio between high and low intensity output of the overall circuit. From Equation (5.5), it is evident that two parameters influence the change in phase: the effective index difference and the length segment of the waveguide structure. In silicon photonics, there are two main methods of eliciting a refractive index change: thermo-optic and free carrier plasma dispersion effects. The refractive index of silicon possesses a relatively large dependence on temperature with a thermo-optic coefficient value of $(dn/dT = 1.86 \times 10^{-4} K^{-1})$ at a temperature of 300 Kelvin and at a center wavelength near 1550nm [118, 123] (thermo-optic value itself is also temperature and wavelength dependent). Alternatively, a change in the refractive index can also be induced with a change in the concentration of free carriers such as electrons and holes. The same technological progress for the fabrication of transistors can be used to dope silicon waveguide structures with N-type or P-type impurity atoms to form PN junctions. A semi-empirical relationship relates the change in refractive index with a change in concentration of free carriers: $\Delta n(\lambda = 1550nm) = -[8.8 \times 10^{-22} \Delta N_e + 8.5 \times 10^{-18} (\Delta N_h)^{0.8}]$ [124, 125]. To illustrate the drastic reduction in lateral footprint between PCM-based phase shifters and conventional approaches, sample values were assumed to generate corresponding π -shifted interference spectra shown in Figure 5.33. For a single arm thermo-optic phase shifter MZI circuit, a 20°C difference in temperature for a 200 μm component is insufficient to achieve the full π phase shift (Figure 5.33b). Either the temperature and corresponding voltage will need to increase, or the overall length will have to be extended. The same is observed for the free carrier phase shifter MZI assuming a modest doping concentration (for both holes and electrons) of $10^{18} [cm^3]$. The

embedded control circuitry often has an upper voltage limit of 3-5V (dictated by conventional IC designs); therefore, the thermo-optic and carrier-based phase shifters require lengths exceeding $500\mu m$ to compensate.

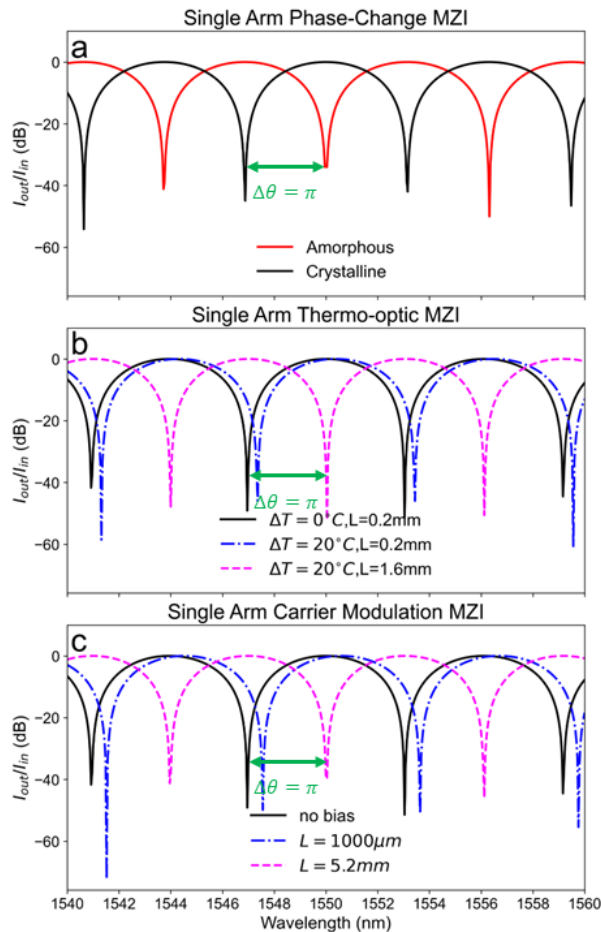


Figure 5.33: Comparison between spectral response for photonic MZI circuits with different phase-shift elements including a.) phase-change materials, b.) thermo-optic effect, c.) charge carrier modulation in PN junctions.

According to ANT layout design rules for chip submission, several photonic circuits including PCM-based MZI phase-shifters were designed on the silicon nitride material platform and sent for fabrication. Figure B.1 depicts the $25 \times 25mm$ design

area of the submitted sample chip for fabrication. At the time of writing this thesis, the silicon nitride library component list which are experimentally verified from ANT only consisted of strip waveguides, TE/TM grating couplers, and tapered edge couplers. To realize MZI circuits, beam splitter components are required. Therefore, several splitter components including y-branch splitters and 3dB directional couplers were designed (discussed in detail in Chapter 6). The top row encompasses calibration and test circuits to evaluate the performance of self-design components such as grating couplers and beam splitters (Figure B.2). The rest of the design area is dedicated to variations of the PCM-MZI phase-shifter. Figure B.3 show an expanded view of the array of MZI circuits. Both single and dual arm configurations consist of the same three path length differences: $300\mu m$, $400\mu m$, and $500\mu m$ which correspond to free spectral ranges of 4nm, 3nm, and 2.4nm respectively. Each MZI is configured with an input grating coupler and a corresponding output grating coupler spaced $250\mu m$ apart to accommodate the optical fiber spacing inside a v-groove array. The input and output waveguides are elongated to compensate for the physical dimensions of the fiber v-groove component so that the electrical contact pads are not shadowed by the v-groove and can be accessed with external probes. Contact pads in pass electrical current to the integrated PCM and ITO bilayer to actuate a phase transition. All PCM patches are designed for a π phase shift across the two phase of amorphous and crystalline.

In summary, this chapter explored the integration of chalcogenide PCMs on silicon photonic waveguides to realize reconfigurable non-volatile resonant and non-resonant structures which can act as weighting elements for optical neuromorphic computing in coherent (single wavelength) and incoherent (multi-wavelengths) con-

figurations. Periodic subwavelength GST meta-gratings were simulated on top of silicon nitride waveguides which show a drastic difference in optical response across amorphous and crystalline material phases. The lower refractive index amorphous phase allowed the propagating waveguide mode to generate a hybrid all-dielectric resonance within the meta-grating structure, producing an appreciable resonance in the near-infrared telecommunications spectral band (1500nm - 1600nm). In contrast, the higher crystalline phase refractive index rejected such resonant modes which resulted in a flat response over the entire spectral range. Additionally, the spectral position of the meta-grating resonance can be tuned to target a specific center wavelength by adjusting the grating period; therefore, the inclusion of multiple spectrally shifted meta-grating components can be incorporated into such incoherent systems. Alternatively, the change in refractive index associated with the PCM phase transition can be utilized within MZI circuits to implement optical phase-shift components. The inclusion of a non-resonant thin film PCM layer on photonic waveguide structures can reach a footprint below $10\mu m$ due to the high refractive index contrast between amorphous and crystalline phases. Upon a phase transition, the MZI output spectrum toggles between transmission maximum and minimum values corresponding to constructive and destructive interference. Without the supply of constant external power supply to maintain the phase shift values, such a non-volatile PCM-based phase shifter components can be leverage to realize ultra-low power coherent optical computation.

Chapter 6

Photonic Silicon Nitride Process Design Kit Development

Considering the limitations with the current Applied Nanotool silicon nitride library offerings and services, significant effort was taken to develop an in-house low-loss photonic stoichiometric silicon nitride platform with the capability of direct integration of chalcogenide phase-change material for future research. Due to the silicon-rich composition of the ANT silicon nitride platform, inherent material losses translate to relatively large signal propagation losses. The smaller refractive index contrast between silicon nitride and the cladding material of silicon oxide produces photonic components with increased footprint, larger bend radii and overall longer propagation lengths compared to its silicon counterparts and therefore would benefit from a low loss material. Stoichiometric silicon nitride (Si_3N_4) deposited through low-pressure chemical vapour deposition (or LPCVD) is the ideal material candidate for this requirement. However, the presence of hydrogen impurities during the deposition process can introduce Si-H and N-H bond formation resulting in high mechanical stresses within the thin film. At thicknesses exceeding 200-300nm, thin film

stress could result in cracks and fracturing—ultimately leading to delamination [126, 127]. Several remediation and compensation techniques have been developed and published in literature to overcome this challenge; however, to keep the fabrication process simple for a rapid turn around within the context of prototyping, a thickness of 300nm was chosen as the optimal thickness before significant post-deposition treatment would be required.

6.1 Stoichiometric silicon nitride material and design of waveguide dimensions

Here at the NanoFAB facility, 300nm of stoichiometric silicon nitride thin film was deposited on four-inch prime silicon wafers with a crystal orientation of (100) through LPCVD. Within a carrier boat, 5 wafers with a 5mm spacing between adjacent wafers, were loaded into the LPCVD chamber with each zone preheated to 767°C, 770°C, and 773°C. A mixture of precursor gasses including dichlorosilane (DCS) and ammonia (NH_3) was used with flowrates of 25sccm and 75sccm respectively at an overall chamber pressure of 250mTorr. Total deposition time was 101 minutes to deposit the targeted 300nm thickness with an average deposition rate of 2.96nm per minute. The deposited silicon nitride was subsequently characterized with variable angle ellipsometry to extract the refractive index (n) and extinction coefficients (κ). Plotting in Figure 6.1 is the n and k profile over the spectral range from 300nm to 1700nm for silicon nitride immediately after deposition (dashed line) and after a thermal annealing procedure at 1000°C for two hours (solid line) in a nitrogen rich atmosphere. Refractive index, represented by the lines in blue, show an overall decrease in the refractive index—especially in the near-infrared spectral range—after

thermal annealing. The combination of high temperature and nitrogen-rich atmosphere helps to reduce the Si-H bond and promote Si-N bond formation, resulting in a closer stoichiometric composition film with a refractive index value close to 1.97. The ellipsometry fitting was performed with a Tauc-Lorentz model which generated extinction coefficient values close to zero for both post-deposition and post-annealed films.

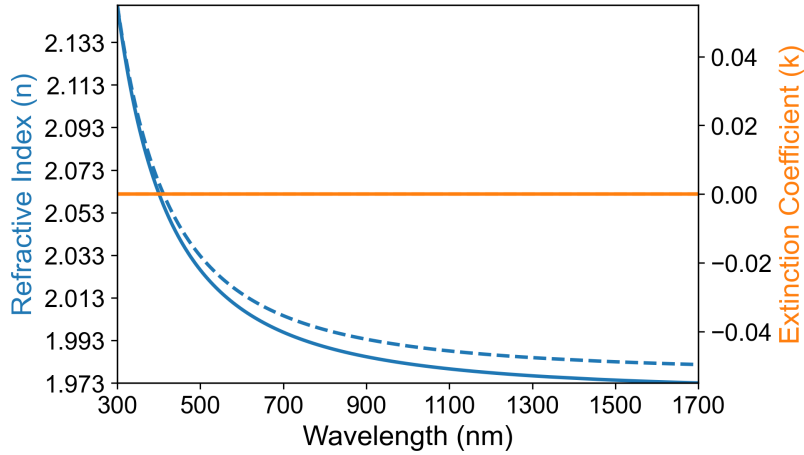


Figure 6.1: Dispersion profile of stoichiometric silicon nitride at a thickness of 300nm, deposited through LPCVD. Dashed and solid lines represent pre-thermal annealing and post-thermal annealing respectively. Blue correspond to the refractive index and orange refers to the extinction coefficient.

The measured material dispersion data was added to the material database within Lumerical to determine the optical waveguide characteristics. As one of the waveguide dimensions has already been determined by deposition constraints, the width of the rectangular waveguide was varied to distinguish between single and multi-mode propagation. Figure 6.2c is a plot showing the effective indices of the first two fundamental modes and the second higher order modes in both TE and TM polarizations

compared to the refractive index of silicon oxide. Any effective indices below the oxide line do not propagate, while values above the oxide line are valid modes that do propagate. Depending on the width of the rectangular waveguide, three distinct regions of propagation exist: widths below 300nm permit exclusively the fundamental TE mode, widths between 300nm and 1300nm permit both fundamental TE and TM modes, and finally widths above 1300nm permit multimode propagation. A width of 1200nm was chosen as an optimal dimension to carry both polarizations, with a preference for the fundamental TE mode. Figure 6.2a,b illustrate the significant difference between the two polarizations in electric field distribution. Centered on a wavelength of 1550nm, the TE polarization is largely confined within the waveguide structure along the width or X dimension and therefore generates a higher effective index value. In contrast, the TM polarization is distributed symmetrically along the height or Y dimension of the waveguide structure with high field intensity lobes positioned just beyond the boundary of the waveguide that is complemented by a lower effective index value. When using waveguides for signal routing, 90-degree bends are a necessity; therefore, the insertion loss of various bend radii are analyzed for both polarizations. Losses are present in two forms: interfacial or mode mismatch loss, and propagation loss as the mode traverses the length of the waveguide. Leveraging a scripted approach, several bend radii values are analyzed within Lumerical MODE solutions. At each bend radius, the modal overlap between the straight and bent waveguide geometries were calculated and subsequently added to the propagation loss incurred for traveling through the 90-degree bend. Insertion loss values are plotted in Figure 6.2d. Modal mismatch between the straight and bent waveguide sections dominate losses at smaller bend radii, while the gains made in larger bend

radii are tempered by presence of propagation losses for larger lengths associated with larger turning radii. Assuming a baseline loss of 0.1dB , a bend radius of $40\mu\text{m}$ was chosen for the TE polarization which will be focus of this photonic platform moving forward.

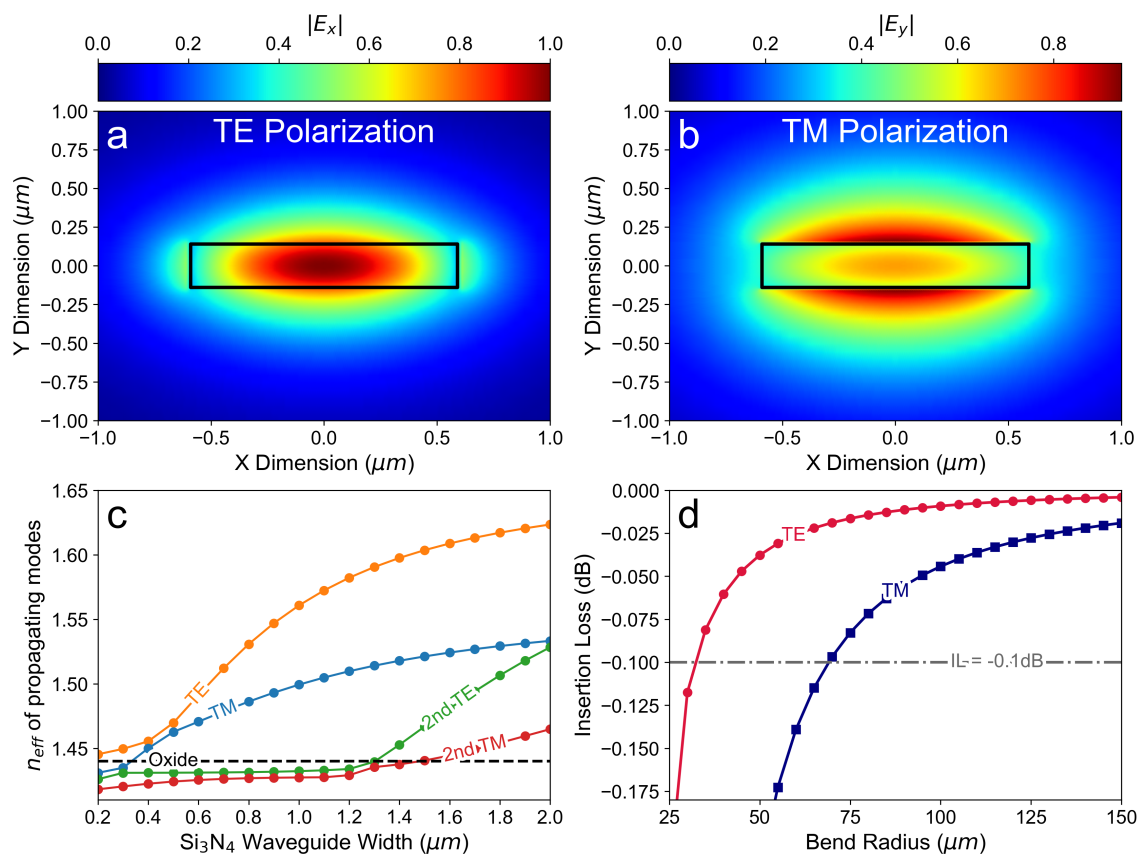


Figure 6.2: Properties of the chosen silicon nitride waveguide dimensions; electric field intensity distribution for a.) TE polarization and b.) TM polarization, c.) effective indices of the first fundamental and second waveguide modes for TE and TM polarizations, d.) bend radii for both polarizations with an insertion loss value of -0.1dB marked by a grey dashed line.

6.2 Waveguide coupling and design of power splitters for TE polarization

The combination of a large turning radius and relatively larger component footprints suggests that routing waveguides could run parallel to each other for a significant amount of the distance. In a parallel waveguide system, the propagating signal could couple to the adjacent waveguide and contribute to noise and undesirable signal cross-talk. Therefore, it is imperative to determine the minimum separation distance between adjacent parallel waveguides to limit potential unwanted signal cross-talk, especially in complex cascaded photonic circuit configurations. The behaviour of a two parallel waveguide system (also known as directional coupler) can be described by coupled mode theory [128]. The power pair of power coupling coefficients which describe the amount of optical power in either the cross or bar waveguide is given by the two relations:

$$\kappa^2 = \frac{P_{cross}}{P_o} = \sin^2(C \cdot L) \quad (6.1)$$

$$\tau^2 = \frac{P_{bar}}{P_o} = \cos^2(C \cdot L) \quad (6.2)$$

where P_{cross} , P_{bar} , and P_o is the power in the adjacent waveguide, the original waveguide and the initial input power respectively. Additionally, under losses conditions $\kappa^2 + \tau^2 = 1$.

To obtain the coupling coefficient and the length required to achieve full power transfer between waveguides, the supermode analysis approach is employed. Once again by using Lumerical finite difference eigenmode solver, two silicon nitride with

the same dimensions are modelled with a specific gap distance. The solver then calculates valid propagation modes that exist within the waveguide system. Depicted in Figure 6.3a,b are the symmetric and anti-symmetric TE modes. Full power transfer occurs for a π phase-shift difference between the two modes after propagating a certain length. This is described as:

$$\beta_1 L_x - \beta_2 L_x = \pi \quad (6.3)$$

$$L_x \left[\frac{2\pi n_1}{\lambda} - \frac{2\pi n_2}{\lambda} \right] = \pi \quad (6.4)$$

$$L_x = \frac{\lambda}{2\Delta n} \quad (6.5)$$

where $\beta_{1,2}$ are the propagation constants of the two modes, Δn is the effective index difference, and L_x is the cross over length for a full power transfer. Iterating through several gap distances between the two waveguides, the corresponding cross over length was calculated. Figure 6.3c shows the plot for the calculated cross over length for a given waveguide gap separation and it is found that this behaviour can be described by an exponential expression relating the gap and length parameters. Drawn in the dashed blue line is the curve that best fits the data points with coefficients $a = 8.27e - 6$ and $b = 2.929e6$. The cross-coupling expression (Equation (6.1)) can be re-written as:

$$\kappa^2 = \sin^2 \left(\frac{\pi}{2} \cdot \frac{L}{L_x} \right)$$

where it is recognized that full power transfer occurs for when the argument of sine is odd multiples of $\pi/2$ phase. To determine the minimum separation distance

between adjacent waveguides (in limiting parasitic coupling), a performance metric can be set such that a maximum allowable cross talk of 50dB can be tolerated over 1cm or $10,000\mu m$. Therefore, solving the two equations:

$$-50dB = 10 \log_{10}(\kappa) \quad (6.6)$$

$$L_x = \frac{\pi \cdot 10000\mu m}{2 \sin^{-1}(\sqrt{\kappa})} \quad (6.7)$$

then, L_x is equal to 4.97 meters. Subsequently, from the exponential expression, the separation gap is determined to be $4.54\mu m$. Including an additional safety margin, the separation distance moving forward is designated as $7\mu m$.

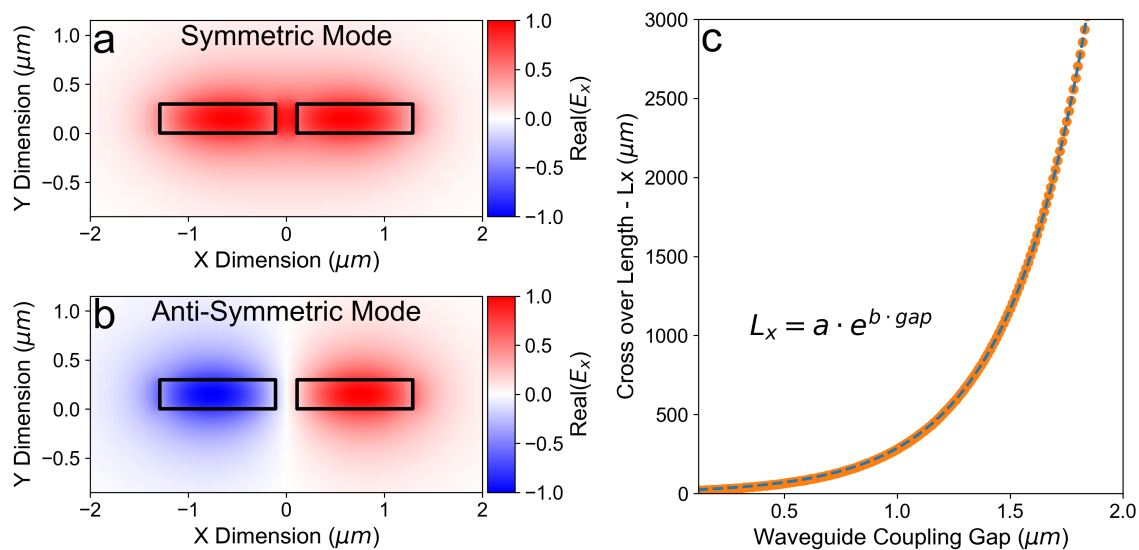


Figure 6.3: Parallel waveguide coupling dynamics; real component of the x direction electric field for a.) symmetric supermode and b.) anti-symmetric supermode. c.) The resulting cross over length for a given waveguide separation gap fitted with an exponential relation.

Directional couplers are the most common passive photonic components used for

splitting and recombining light in integrated circuits. Thus, to realize a cascaded network of PCM based MZI phase-shifters, a 3dB directional coupler is required. Assuming devices are fabricated in the NanoFAB with the RAITH TWO 30kV electron beam lithography tool, minimum feature sizes which are routinely patterned with no issues are 100nm and above. The separation gap for the design of a 3dB directional coupler can be set for 200nm. The calculated length is $8.32\mu m$. Routing between the coupling region and the $7\mu m$ separation distance to maintain cross-talk can be implemented with a S-bend waveguide whose geometry can be described by a cubic Bezier curve. Similarly to the 90 degree bend, the S-bend geometry will also induce propagation losses in the form of scattering if the bend angles are abrupt. To determine the appropriate length for a S-bend with the smallest insertion loss, several lengths are simulated. Plotted in Figure 6.4a are the insertion loss values with corresponding S-bend lengths. Beyond a length of $25\mu m$, the insertion loss plateaus and is dominated by the material losses within the waveguide; therefore, a length of $27\mu m$ was chosen for the directional coupler design. Simulating first in 2.5D varFDTD and then verifying the results in 3D FDTD, the 3dB cross over point of the bar and cross port transmission response did not align to the design center wavelength of 1550nm. The slowly varying waveguide, transitioning away from the 200nm coupling region also contributed to power coupling; thus, the additional coupling must be taken into consideration by shortening the coupling region. Adjusting the coupling lengths, the desired transmission response was obtained as illustrated in the electric field map in Figure 6.4b and the spectral response in Figure 6.4c.

The versatility of a 4-port component such as the directional coupler can find many applications among various photonic circuits; however, as evident in the previous

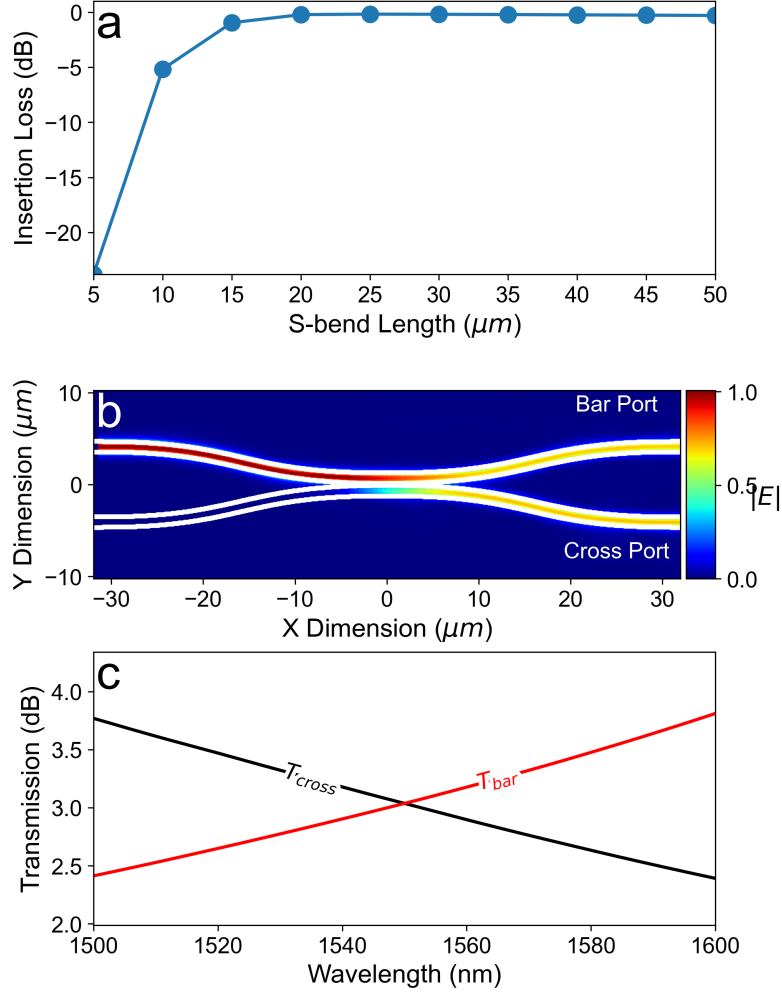


Figure 6.4: Properties and characteristics of 3dB directional coupler; a.) insertion loss for a waveguide s-bend geometry of various lengths, b.) electric field intensity distribution of the directional coupler at an operating wavelength of 1550nm, c.) spectral response for the cross (black) and bar (red) ports of the 3dB directional coupler.

demonstration, the transmission response is highly wavelength-dependent and only satisfies the 3dB splitting ratio at one designated wavelength. Y-branch splitter/combiners are also a useful alternative component for splitting and recombining optical

signals with the advantage of providing a broadband response, but at the reduction of a port with only 3-ports available. The most basic geometry consists of an input waveguide feeding into a wide slab section which permits multimode interaction to produce two mode intensities distributed between the two output waveguides. Such a component is also known as a multi-mode interference coupler or MMI. Tapering between the waveguide and the wider slab section can help reduce mode mismatch generated insertion losses. The relatively lower refractive index contrast between silicon nitride and oxide cladding material combination compared with traditional silicon on insulator implies larger optical component footprints and the design for such a MMI splitter component is no exception. Therefore, towards designing a low loss, compact and wavelength insensitive splitter component, a Y-branch or Y-junction geometry is explored. Figure 6.5a illustrate the schematic for the Y-branch design which consists of an input waveguide and two output waveguides separated by a gap. A polygon shape connects the input and output waveguides with its side-wall profile described by a spline interpolation based on discrete control widths (W1 – W5). Similarly constrained by the resolution of electron beam lithography, the minimum feature size is set for 200nm; therefore, the output separation gap is set to this dimension. The Y-branch geometry was first modelled within Lumerical 2.5D varFDTD and the results were subsequently verified with fully vectorial 3D FDTD. For both simulation models the same scripted approach was taken to parameterize all relevant design parameters such as the control widths, and the overall length of the junction geometry. The first and last widths are set as constants corresponding to the single width of the waveguide at $1.2\mu m$ and double waveguide widths in addition to the gap distance respectively. The rest of the width parameters can take on any

value and the spline interpolation will generate a sequence of vertices which defines the side profile of the junction polygon. An optimization routine known as particle swarm optimization (PSO) is used to determine the best sequence of widths to produce a low loss, wavelength insensitive 50% splitting ratio in a compact footprint across the wavelength range of 1500 – 1600nm. Inspired by the social behaviour of flocks of birds or schools of fish, particle swarm optimization is a population-based stochastic optimization technique that mimics the behaviour of a swarm of particles moving through a parameter search space to find the optimum solution [129]. Each particle represents a candidate solution and are initialized at random positions with random velocities in the parameter space. Each particle adjusts its position and velocity based on its own best-known position (personal best - p_{best}) and the global best-known position (global best - g_{best}). The global best is the position in the swarm with the lowest figure of merit value given by:

$$v_n = w \cdot v_n + c_1 rand() \cdot (p_{best} - x_n) + c_2 rand() \cdot (g_{best} - x_n) \quad (6.8)$$

where v_n and x_n are the particles velocity and position, w is known as the inertia weight which balances between exploration and exploitation, c_1 and c_2 are the cognitive and social learning coefficients that control the influence of personal and global best positions, and finally $rand()$ produce random numbers uniformly distributed between 0 and 1 to represent unpredictable behaviour in a natural swarm. After each optimization round or generation, the position of the particle is updated through the relation:

$$x_n(t+1) = x_n(t) + v_n(t+1)$$

The optimization is stopped once the maximum number of iterations have been reached or the desired level of convergence to a specified figure of merit value is obtained. The figure of merit defined here is to maximize overall transmission at a single output port. Since the 2.5D varFDTD approximation method is computationally efficient for the simulation of planar photonic circuit components, a large range of widths and length values were considered for the PSO routine. The optimal set of parameter values provided a suggestion of what the final values would take on; therefore, a smaller range was set for the fully vectorial solve within FDTD which would also consider scattering in the z or thickness dimension and the additional coupling between the output waveguides. Final optimized junction geometry produced an average splitting ratio of 49.37% across the entire spectral range as shown in Figure 6.5b, which translates to an overall insertion loss of only 0.05dB for a length of $6\mu m$.

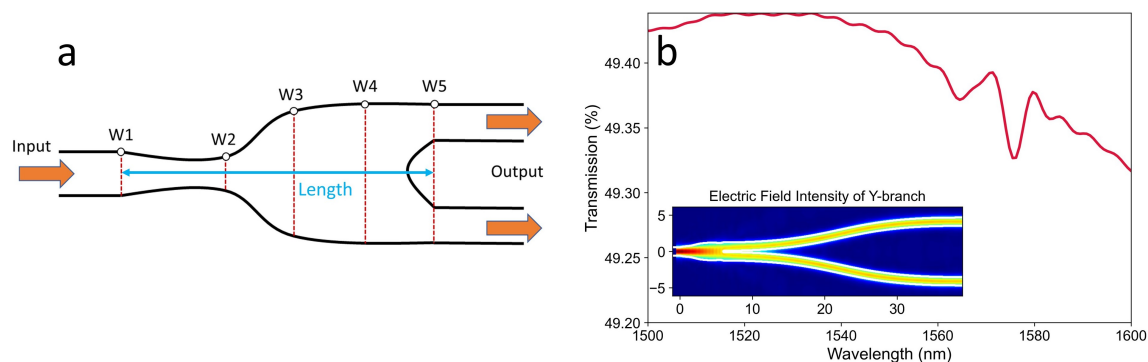


Figure 6.5: Design and simulation of Y-branch splitter/combiner; a.) schematic of the discretized splitter geometry into several distinct width parameters, b.) broadband transmission response at the output with inset showing the electric field intensity distribution at wavelength of 1550nm.

6.3 Design of photonic grating coupler constrained by fabrication limitations

Tackling the coupling issue to and from the integrated photonic circuit was the next challenge to solve. There are several possible ways to couple the large mode field diameter signal from an optical fiber to the integrated photonic waveguide, but the two main prevailing methods include edge coupling through a waveguide taper component and surface coupling through a grating coupler component. The main advantages of an edge coupler are the low loss high spectral bandwidth properties of transforming the large optical fiber mode down to the cross sectional mode found in a traditional rectangular strip waveguide. However, one distinct disadvantage of the edge coupling approach is the restriction for both the physical sample chip dimensions, and the placement of the optical fiber at the edges and thereby impeding large scale testing and evaluation of many circuit components. Surface coupling through grating couplers do not encounter such issues and are desirable for large scale testing of photonic circuits with no limitations on photonic chip dimensions. Therefore, the grating coupler was chosen as the photonic component of choice for implementing optical inputs and outputs. The behaviour of photonic grating couplers can be described by the Bragg grating equation:

$$\Lambda_i = \frac{\lambda_c}{n_{eff} - n_{clad} \sin(\theta)} \quad (6.9)$$

where Λ_i is the period for the i -th radiative unit cell, n_{eff} is the effective index of the unit cell, n_{clad} is the refractive index of the upper cladding material, θ is the angle measured from normal and λ_c is the central coupling wavelength [130, 131].

For simple grating geometries, where the grating period is the same across the entire structure, the incident light is diffracted into a single order that will propagate down the slab waveguide. The main drawbacks associated with such standard uniform grating couplers are the narrow bandwidth response (usually between 30-40nm) and the relatively low coupling efficiency. Low coupling efficiencies are the result of two main contributing factors: grating directionality and mode mismatch. A low grating directionality indicates that a large portion of the incident optical power is diffracted towards the substrate instead of towards the waveguide layer. Different approaches have been explored in literature to reduce power leakage to the substrate with the use of either polysilicon over layers, or dielectric thin film stack constituting a distributed Bragg reflector (DBR) and metallic mirrors embedded within the substrate [132–134]. Mode mismatch is a result of the difference in optical intensity profile radiated from the grating coupler do not match with the nearly Gaussian mode of an optical fiber. Control over the etch depth and the fill factor each grating period can tailor the radiated field profile to match that of the fiber. To avoid fabrication complexity associated with depositing extra reflector layers, the focus towards decreasing mode mismatch motivated the design process moving forward. Here, the grating coupler design employ a linear apodization over the grating structure which achieves two positive effects: a reduced optical impedance from waveguide to grating, and the opportunity to tailor the radiation profile to limit mode mismatch [135]. Importantly, the grating period remains as a free parameter which satisfy the Bragg condition by all grating structures. Presented in Figure 6.6a is the cross-sectional schematic highlight the evolution of the fill factor and by extension the grating period. Fill factor is described by:

$$F = F_o - Rz \quad (6.10)$$

where R is the apodization factor, F_o is the initial fill factor and z is the position along the length of the grating. The effective index of the radiative unit is found by:

$$n_{eff} = Fn_o + (1 - F)n_e \quad (6.11)$$

where n_o and n_e is the slab effective index of the silicon nitride layer and the etched region respectively. Scripting the Lumerical model within FDTD, the 2D grating geometry was instantiated, an optical fiber was created to deliver a TE polarized signal, and a PSO routine was performed to optimize the apodization factor and the placement of the optical fiber. A $F_o = 0.9$ was chosen to stay within resolution limits of the electron beam lithography tool and an angle of 8° was used to adhere to measurement specifications. The buried oxide layer thickness (T_{box}) also play an important role in recapturing some of the optical power that has been directed towards the substrate upon an initial pass. The reflection at the silicon and oxide interface redirects a fraction of the optical power back towards the grating and should travel a distance such that it will constructively interfere with the captured light propagating along the length of the grating. After a simple thickness sweep the optimal thickness was found to be $3.3\mu m$. This thickness will be used for the entire silicon wafer during fabrication. The PSO algorithm produced results generating a coupling efficiency of 37% centered on 1550nm. Illustrated in the inset of Figure 6.6, fields are concentrated within the silicon nitride slab layer with some fields transmitted through to the substrate.

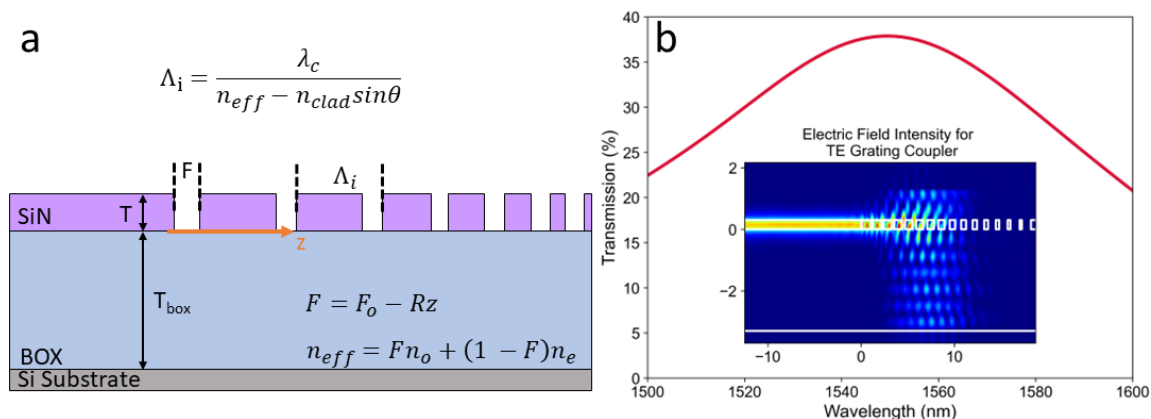


Figure 6.6: Design and simulation of TE grating coupler; a.) cross sectional schematic of a fully etched apodized grating structure, b.) spectral response of a 2D apodized grating with inset showing coupling of electric field from free space into the slab waveguide.

Verification of grating coupler performance in 3D fully vectorial environment also requires the modeling of a taper structure to transform the large waveguide slab mode down to the rectangular waveguide mode depicted in Figure 6.7. Typical taper structures, as in the case of the edge coupler for example, is a straightforward optical component and follow a simple rule: longer components, up to the propagation loss limit, provide a slowly varying waveguide shape to allow for the smooth and low loss transition between waveguide modes. However, a standard linear taper structure based on the silicon nitride on insulator material platform will reach or exceed $100\mu\text{m}$ in length. Patterning polygons with feature sizes as small as 100nm , will require the electron beam lithography tool to expose within a $100\mu\text{m} \times 100\mu\text{m}$ area or writefield. Geometries that extend pass this boundary will be exposed in the adjacent writefield with an alignment tolerance of around $10 - 20\text{nm}$. Moreover, the electromagnetic control coils used to deflect and steer the incident electron

beam introduce aberrations, much like an optical lens, especially at the outer edges. Therefore, it is advantageous to design a taper component that is compact and as low loss as possible. By changing the taper shape, similar performance can be achieved at a significantly reduced footprint. Two designs were considered: one linear/power profile, and a superposition of a parabolic sine squared profile. Following the Lumerical example, a taper is parameterized and analyzed to establish a baseline using the following equation:

$$w(x) = \alpha(L - m)^m + w_2 \quad (6.12)$$

$$\alpha = \frac{w_1 - w_2}{L^m} \quad (6.13)$$

where L is the length of the taper, w_1 is the width of the waveguide at $x = 0$, w_2 is the width at $x = L$, and m is the power factor. The taper structure is modelled within FDTD and a PSO routine was used to determine the optimal length and power m . Tapering down from a width of $12\mu m$ to the waveguide width of $1.2\mu m$ an overall insertion loss of 0.5dB with an average transmission of 90% was obtained for a length of $50\mu m$ with a m value of 1.88. Minimal field scattering was observed from the electric field intensity distribution shown in Figure 6.7a. In comparison, the parabolic sine squared geometry was modelled and simulated following the set of expressions:

$$Y = a(bz^2 + (1 - b)z) + (1 - a) \sin^2\left(\frac{c\pi z}{2}\right) \quad (6.14)$$

$$0 \leq \alpha \leq 1 \quad (6.15)$$

$$c \in \text{odd integer} \geq 3 \quad (6.16)$$

$$\frac{-c}{c-2} \leq b \leq \frac{c}{c-2} \quad (6.17)$$

$$0 \leq z \leq 1 \quad (6.18)$$

where z is the normalized taper length and Y is the normalized side taper profile [136]. A slight reduction in overall transmission (at an average of 89.6%) is obtained with the parabolic sine squared profile compared to the linear/power profile; however, the total length has been reduced to only $30\mu m$ and thus proving the more complex geometry can deliver a similar level of performance at a significantly reduced footprint.

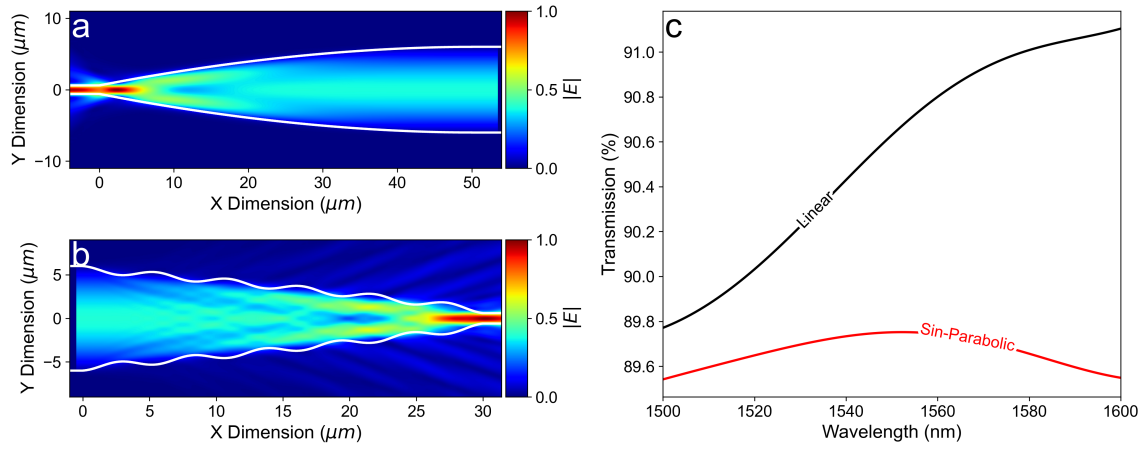


Figure 6.7: Performance comparison between two waveguide taper geometries; electric field intensity distribution for a.) a linear and b.) sine parabolic shape. c.) Broadband transmission response for linear (black) and sine parabolic (red).

Additional footprint reductions are made when considering the modal field diameter (MFD) of a single mode optical fiber, such as the SMF-28 fiber, which has an MFD of $9.5\mu m$. Therefore, the taper width can be reduced to $10\mu m$ instead of $12\mu m$ with no impact to the overall performance. Plotted in Figure 6.8 is the normalized transmission response of the 3D grating coupler component in black with a red dash line denoting the 1dB value. This TE grating coupler with a unique taper design produced a 1dB coupling bandwidth of 60nm. The Figure 6.8 inset illustrates the final GDS layout of the entire structure.

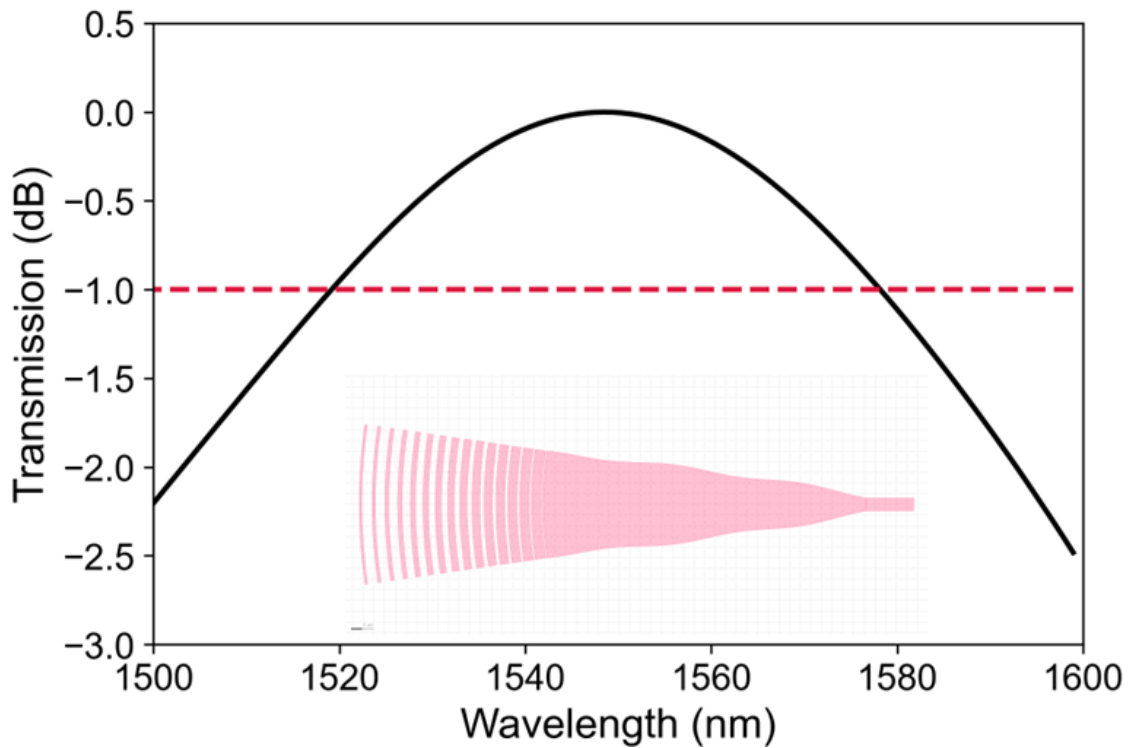


Figure 6.8: Normalized spectral response of the optimized TE grating coupler with red dashed line marking the 1dB value to illustrate the bandwidth of the coupling efficiency.

6.4 Fabrication process flow, exposure compensation, and scripted GDS layout

The NanoFAB, here at the University of Alberta facilitated the entire fabrication and development process to realize the library of silicon nitride photonic components. Prime crystalline silicon wafers are first cleaned with a piranha solution (3:1 ratio of sulfuric acid and hydrogen peroxide solution) for 15 minutes to remove any organic materials and other contaminants as shown in step 1 of Figure 6.9. The clean wafers are then loaded in an oxidation chamber to grow the buried silicon oxide layer (BOX) in a wet oxidation process (step 2 of Figure 6.9). Approximating the achievable thickness with a Deal-Groove model, it was calculated that given an initial oxide thickness of 1nm (piranha bath oxidizes the wafer surface to form a thin layer of silicon oxide) it would take 24 hours and 42 minutes at a temperature of 1100°C and a partial pressure of 0.92 atm to achieve a total thickness of $3.3\mu\text{m}$. The resulting silicon wafers had an average oxide thickness of $3.2597\mu\text{m}$ with a maximum of $3.2634\mu\text{m}$, and a minimum of $3.2497\mu\text{m}$. The oxide thickness distribution was mapped with Filmetrics shown in Figure C.1. The roughly 50 – 60nm difference between the targeted thickness and the actual thickness was analyzed to understand its impact on the coupling efficiency of the grating couplers and it was found to have minimal impact. Another round of piranha cleaning was performed before the wafers are then loaded into the LPCVD chamber to deposit stoichiometric silicon nitride (step 3 Figure 6.9). Unfortunately, due to the complexity of this deposition method, the thicknesses obtained deviated further from the targeted specification of 300nm. Average thickness was 316nm, with a maximum of 328nm and minimum of 308nm.

Similar thickness mapping is shown in Figure C.2. The 4-inch wafers are then diced into 12x12mm square sample pieces. Fabrication of silicon nitride photonic circuits starts with a piranha bath, followed by a wash in Surpass 3000—a cationic surface priming agent that promotes surface adhesion with the polymer-based photoresist. Surface priming begins with a 30 second rinse in deionized (DI) water followed by drying with nitrogen, 60 seconds in Surpass 3000 solution, and then another 30 second rinse in DI and drying with nitrogen. With only the photoresist as the masking layer, patterning photonic circuits necessitates the use of negative photoresist. Compatible with electron beam lithography, Micro-resist ma-N2403 series negative resist was used (step 4 Figure 6.9). 12mm sample chips are held down by a vacuum port and spun at a peak RPM of 5650rpm for 60 seconds to obtain, on average a resist thickness of 240nm. Resist thicknesses are verified with Filmetrics (Figure C.3). Exposed at an acceleration voltage of 30kV with a $15\mu\text{m}$ aperture, photonic components are dosed at $250\mu\text{C}/\text{cm}^2$ (step 5 Figure 6.9). After patterning, development of the resist consisted of a 90 second bath in MF319—a tetramethylammonium hydroxide (TMAH) based solution—followed by a wash with DI water. Dry etching was performed in an Oxford PlasmaPro 100 ICPRIE instrument with a CHF_3 and O_2 chemistry for 5 minutes (step 6 Figure 6.9). Any excess resist material is subsequently removed with a 10-minute sonication in remover PG.

When patterning sub-micrometer feature sizes with lithography tools, secondary effects from the physical interaction become non-negligible and must be taken into consideration. For example, diffractive effects in photolithography smoothens sharp edges and corners and distorting the original design especially at pattern features with dimensions close to the diffraction limit. Similarly in electron beam lithogra-

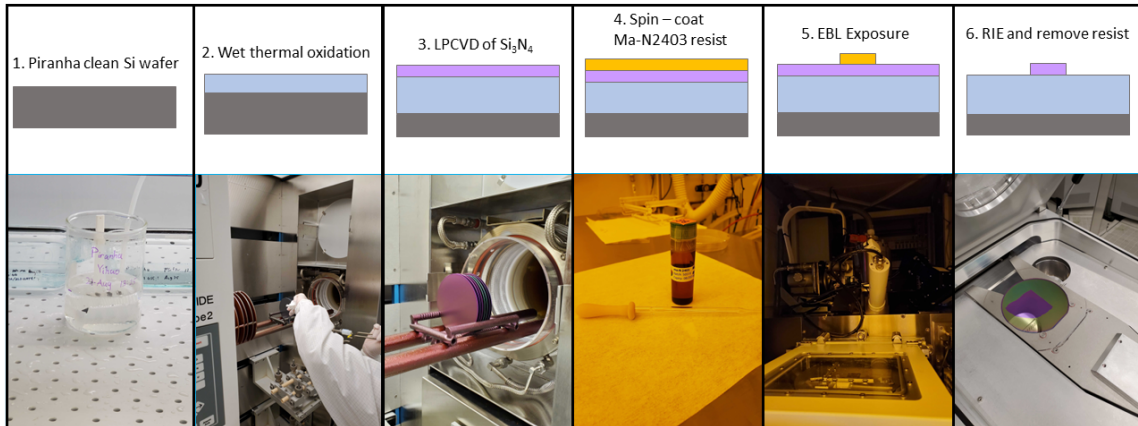


Figure 6.9: Typical process flow for the fabrication of photonic integrated circuits based on low loss stoichiometric silicon nitride material.

phy, the electron beam can undergo elastic and inelastic scattering with the resist material and the underlying substrate layer, causing the exposed pattern to significantly deviate from the intended design. This is known as the proximity effect and become exacerbated for features that are closely spaced such as in photonic grating couplers [137, 138]. The proximity effect arises from two main sources: forward scattering and backscattering of electrons. Forward scattering occurs when incident electrons of the Gaussian distributed beam interact with the resist material and scatters causing a broadening of the incident beam profile. Backscattering occurs when the primary electrons interact with the substrate material underneath the resist layer and is deflected back towards the resist material, leading to additional unwanted dosing. Secondary electrons can also be generated from both scattering interactions and contribute to an increase in the total exposure dose at all substrate regions. Consequently, the broadened electron beam profile, as illustrated in the top panel of Figure 6.10, will render adjacent regions to receive a higher total exposure

dose than originally intended and result in a profile outlined in the red dashed lines. The SEM image in the bottom panel of Figure 6.10, depicts a fabricated grating coupler after dry etching with the apodized gratings closer toward the taper region fuse together. In contrast, the farther spaced grating structures towards the back, are accurately patterned.

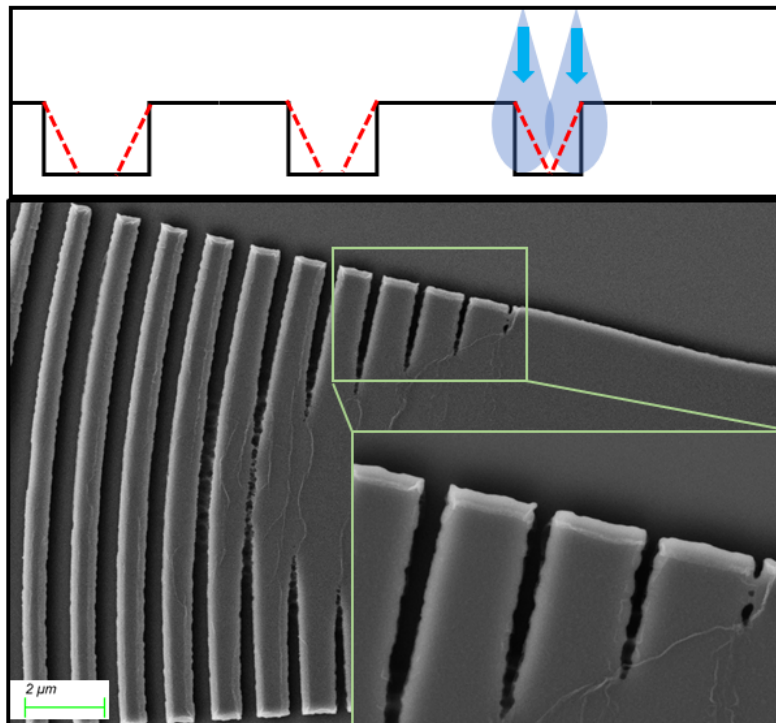


Figure 6.10: Incorrect exposure of patterns and geometries due to the presence of the proximity effect inherent to electron beam based lithography techniques. Top cartoon show the dispersion of incident electrons leading to a broadening and over exposure of adjacent features. Bottom SEM image show at sufficient exposure doses closely spaced features will merge into one.

Several corrective techniques exist to address the proximity effect in electron beam lithography:

1. Exposure dose modulation-by varying the exposure dosage along the pattern geometry to compensate for scattering effects, overdosing of adjacent features can be limited, resulting in the accurate representation of the feature.
2. Proximity effect correction-reshaping the desired pattern geometry based on a mathematical corrective expression to compensate for electron scattering.
3. Shaped beam exposure-specially designed beam apertures and lenses can shape the electron beam profile to match the desired pattern.
4. Resist processing optimization-different resist formulations can have lower sensitivity to backscattering electrons in combination with processing optimizations in terms of exposure time, resist baking time, and developer solution to minimize proximity effects.

Integrated within the RAITH electron beam lithography software environment (NANOSUITE), a proximity effect correction module called nanoPECS that is based on the dose modulation technique is utilized to correct for the proximity effect. To begin correcting for the proximity effect, the user must first define the sample layer stack. Here, the layer definition consists of the negative photoresist Ma-N2403 (thickness = 240nm) followed by the stoichiometric silicon nitride material (thickness = 300nm) with material parameters such as atomic weight, density and ionization potential describing each layer. Subsequently, a Monte Carlo simulation is performed to approximate the trajectories of one million electrons as shown in Figure 6.11a. Figure 6.11b plots several proximity functions that best fit the energy deposition as a function of radial distance from the beam center. Mathematically, the energy

distribution of the scattered electrons can be approximated as the weighted sum of several Gaussian distributions and one additional exponential function as follows:

$$f_{proximity} = \frac{1}{\pi(1 + \eta + v + v_2)} \left(\frac{1}{\alpha^2} e^{-\frac{x^2}{\alpha^2}} + \frac{\eta}{\beta^2} e^{-\frac{x^2}{\beta^2}} + \frac{v}{2\gamma^2} e^{-\frac{x}{\gamma}} + \frac{v_2}{\gamma_2^2} e^{-\frac{x^2}{\gamma_2^2}} \right) \quad (6.19)$$

Upon fracturing the geometry into smaller pieces as shown in Figure 6.11d, the proximity function will be used to compute a corrected exposure dose matrix that will be assigned to each fractured piece that will compensate for the proximity effect. Finally, an overview of the exposed resist profile can be generated to confirm the solution as shown in Figure 6.11c.

By applying this technique to the grating coupler geometry, it is evident from the SEM images in Figure 6.12, that overdosing in the small gap grating region is no longer present and the full component is accurately reproduced according to the optimized design. The inset in panel a shows the compensated exposure dose distribution across the grating coupler geometry. It is self-evident that the large area taper region receives less dosage and the sparsely spaced grating in the back receives a proportionally higher dosage. The cross-sectional analysis in panel b also confirms that the small gaps in the front gratings have been properly realized.

Layout for fabrication was generated through a MATLAB based object-oriented programming framework called Raith_GDSII MATLAB toolbox written by Aaron Hryciw [139]. Four class definitions in the toolbox provide a simple, versatile, and scriptable means of generating hierarchical patterns and position lists for the RAITH electron beam lithography system (Figure 6.13a). The four main classes are defined as: Raith_element, Raith_structure, Raith_library and Raith_positionlist. The first

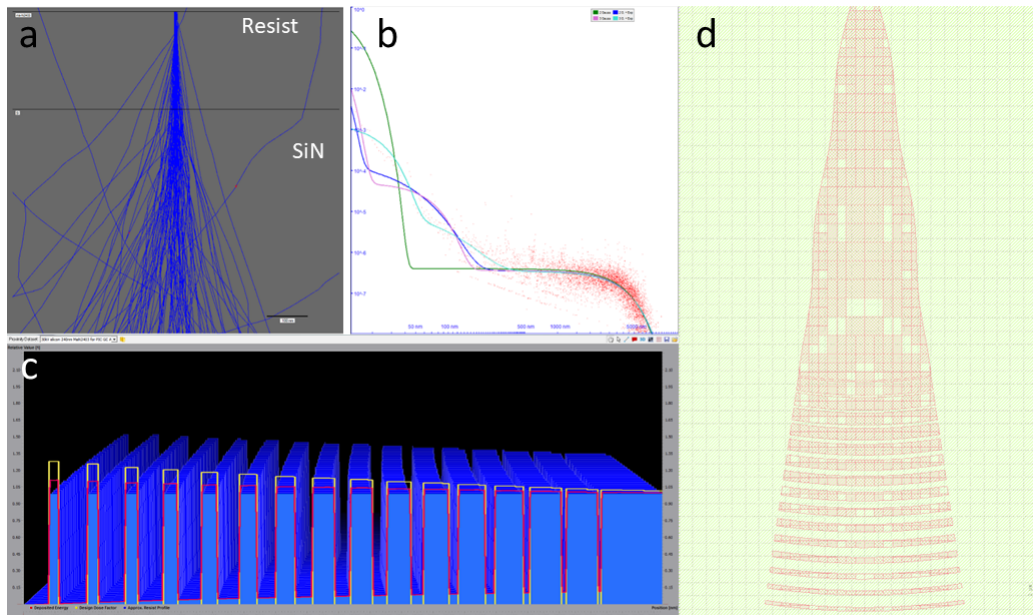


Figure 6.11: The process of proximity effect correction; starting with a.) Monte Carlo simulation of electron trajectories incident on a layer stack of resist and silicon nitride material, b.) normalized energy distribution along the radial direction away from the center of the incident beam, c.) simulated post-exposure photoresist profile with dose correction applied, d.) exposure dose fracturing applied to the grating coupler GDS layout.

three classes reflect the structure of the GDSII stream format and are used to generate patterns for exposure that are subsequently referenced by the positionlist definition.

The purpose of each class is described as follows:

- *Raith_element*-used to define low level patterns and shapes including polygons, paths, dots, arcs, circles, text, and fixed beam moving stage (FBMS) geometries.
- *Raith_structure*-comprised of a collection of *Raith_elements* objects with defined names, useful for grouping a collection of geometries.

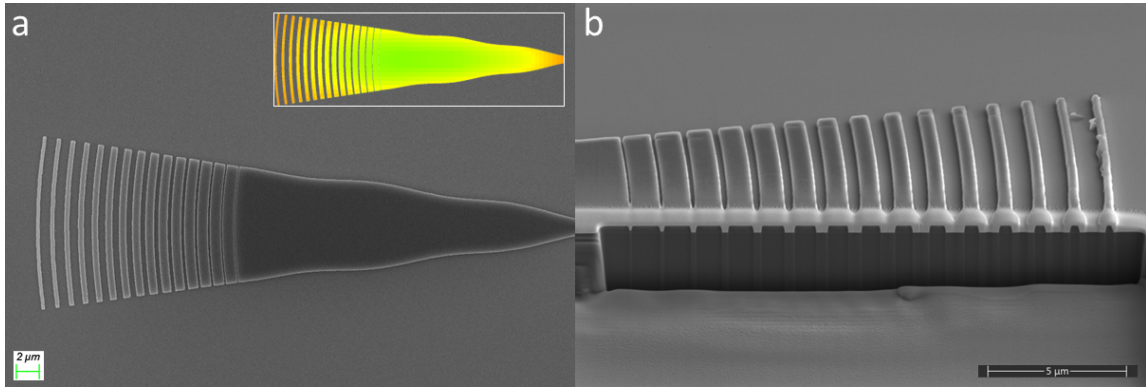


Figure 6.12: Fabricated grating coupler with the application of proximity effect correction (fractured exposure dosage pattern); a.) top view of the fabricated grating coupler with an inset representing variable exposure dosage as color, b.) cross sectional view of fabricated grating coupler cut with focused ion beam milling.

- *Raith_library*-comprised of a collection of uniquely named Raith_structure objects which can be exported to supported GDSII file formats such as (.gds) or Raith proprietary file format (.csf).
- *Raith_positionlist*-comprising of chip-level coordinates or addresses defined within the electron beam lithography tool to pattern the corresponding Raith_structure geometries.

Following these definitions, complex structures such as FBMS waveguide spirals spanning thousands of microns in length with no writefield stitching was developed and shown in Figure 6.13b and matrix arrays of compound patterns with different assigned exposure dosages for rapid recipe optimization are demonstrated in Figure 6.13c.

In summary, this chapter presented a comprehensive overview of the design, simulation modelling, and fabrication of a passive photonic process design kit (PDK)

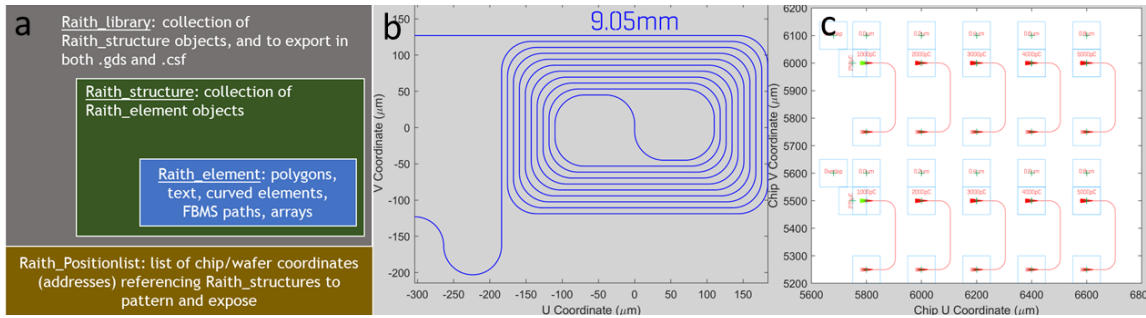


Figure 6.13: Development of MATLAB based toolbox for layout and exposure preparation; a.) hierarchical organization of layout classes and definitions, b.) layout of waveguide spiral based on FBMS lines with text elements, c.) arrayed layout of various components and geometries consisting of grating coupler, waveguides and single pixel lines.

based on stoichiometric silicon nitride, aimed to realize an optical hardware accelerator for neural network applications with the inclusion of chalcogenide phase change materials. Several passive components were designed including 3dB directional couplers, y-branch splitters/combiners, and grating couplers. The optimized geometries were fabricated on a Si_3N_4 on insulator material stack and exposed using a 30kV electron beam lithography tool. Proximity effect correction was used to compensate the distortion observed in patterned structures. The exposure correction profiles were subsequently incorporated into a object-oriented programming framework used to instantiate the photonic design layout. A full range fabrication process flow was carried out in the NanoFAB facility, from deposition of thin films to lithography and etching.

Chapter 7

Conclusion & Future Challenges

7.1 Conclusion

The rapid growth and advancement in high-speed broadband telecommunication architectures have realized a high-capacity data stream infrastructure that can carry and transmit enormous volumes of information from an expanding collection of interconnected devices and sensors. Manual data analysis and the use of analytical models are inefficient and impractical for many large volume data applications; however, recent progress in machine learning algorithms adapted to mimicking the signal pathway and organization of a biological brain, such as deep neural networks, have proven to be successful at filtering and processing large datasets. Neural networks provide functionalities such as object classification, pattern recognition and inference predictions which underpin the progress and development of semiconductor designs, robotic automation and the co-integration of cloud and edge computing networks. However, the development of next-generation telecom and computing infrastructure to accommodate the expansion of such key technology sectors require a platform that is simultaneously low energy consumption, high bandwidth, adaptable and reconfig-

urable. Hindered by physical limitations of copper interconnects and combined with the slow down of Moore’s law, performance scaling in electronics is unable to meet such requirements. Signal transmission in the optical domain is free from resistive losses and capacitive charging delays which presents a viable platform to implement computational functionalities with high bandwidth, low latency, and efficient power consumption performance.

This thesis demonstrates the hybridization of optical fibers and integrated photonic circuits with chalcogenide phase-change metamaterials to realize an all – optical neural network hardware accelerator platforms with optical memory functionality to surpass traditional Von-Neumann computing bottlenecks. We explored a reconfigurable metasurface signal intensity modulator with switchable group delay dispersion integrated on the tip of an optical fiber. The period of the arrayed geometry of cuboid unit cells, patterned through focused ion-beam milling, controls the spectral positioning of the resonant response and therefore is adaptable for wavelength-division multiplexing modulation schemes. Similarly, the addition of phase-change metamaterials with photonic integrated circuits have illustrated both intensity and phase modulation in a compact footprint. Periodic subwavelength grating PCM structures provide two distinct optical responses across the amorphous and crystalline phases. Depending on the physical dimensions of the grating structure, the waveguide mode couples into the amorphous structure at a particular wavelength. In contrast, irrespective of the grating geometry, the propagating mode does not couple into the crystalline phase and produces a flat response. Therefore, a combination of spectrally shifted PCM grating structures in a photonic network can realize both positive and negative values to replicate weighted summations of a neural network. By lever-

aging the PCMs large optical contrast in refractive index across amorphous and crystalline material phases, non-resonant integration of PCM in photonic waveguides were demonstrated to be efficient low energy and compact phase-shifters in MZI configurations. Both homogeneous uniform thin film integration and heterogeneous dispersion engineered effective medium integration of PCM patches on either single or dual arm MZI circuits permitted a full π -phase shift of the output spectrum without the continuous supply of external energy.

The implications of a self-holding phase-shift value is the missing key-component of current demonstrations in coherent MZI mesh network based photonic hardware accelerators for neural networks. Current demonstration of photonic matrix vector multiplication with singular value decomposition utilizes volatile approaches such as thermos-optic or carrier concentrations which still rely on electrical programming read from an exterior memory module—Von Neumann architecture. High refractive index contrast, non-volatile chalcogenide phase-change alloys with optical memory functionality present a suitable material platform to migrate away from the Von-Neumann configuration and realize a zero-energy ultra-fast optical hardware accelerator to address the computational performance requirements of next-generation machine learning applications.

7.2 Future Challenges

The inclusion of chalcogenide phase change materials with photonic integrated circuits, in either MZIs or MRRs, have presented a viable reconfigurable and non-volatile mechanism for index modulation; however, current literature demonstrations show technical limitations in four main categories: inefficient phase-switching mech-

anisms, constrained material endurance performance, high insertion losses-especially in the crystalline phase, and reliance on electro-optic signal conversions for signal accumulation and threshold activation functions. Although PCMs can undergo phase transitions within picoseconds-under illumination from a femtosecond pulse laser-the platform of photonic integrated circuits requires an integrated solution for implementing phase transitions. Therefore, recent publications have gravitated towards the use of metallic or TCO micro-heaters to deliver sufficient energy required for amorphization or crystallization [110, 113, 114]. These methods suffer from long switching times due to the thermal time constant (as discussed in Chapter 5) and high switching energies. Unconventional approaches employing the use of 2D materials such as graphene have demonstrated a potential solution to achieve low power phase switching [112, 140]. The repeated and frequent switching cycles of a PCM based modulation component introduces material fatigue in the form of phase-separation and formation of crystallized sub-domains which will ultimately lead to material failure and result in an inability to phase switch [141]. In-situ deposition of a protective coating, for example $ZnS : SiO_2$, could help to prevent oxidation of PCMs and phase separation; however, to ensure material endurance and longevity, material discovery and new stoichiometric formulations should be explored. Additionally, the use of high-throughput deposition techniques could also aid in uncovering new PCMs alloy compositions alternative to GST with minimal optical losses. Lastly, non-linear materials such as saturable absorbers could be leveraged to perform threshold activation in the optical domain to avoid bandwidth limited and lossy electro-optic conversions that current neural network photonic accelerators rely on [142, 143].

References

1. Jordan, M. I. & Mitchell, T. M. Machine learning: Trends, perspectives, and prospects. *Science* **349**. Publisher: American Association for the Advancement of Science, 255–260. <https://www.science.org/doi/full/10.1126/science.aaa8415> (2023) (July 2015).
2. Samek, W., Montavon, G., Lapuschkin, S., Anders, C. J. & Müller, K.-R. Explaining Deep Neural Networks and Beyond: A Review of Methods and Applications. *Proceedings of the IEEE* **109**. Conference Name: Proceedings of the IEEE, 247–278. ISSN: 1558-2256 (Mar. 2021).
3. LeCun, Y., Bengio, Y. & Hinton, G. Deep learning. en. *Nature* **521**. Number: 7553 Publisher: Nature Publishing Group, 436–444. ISSN: 1476-4687. <https://www.nature.com/articles/nature14539> (2022) (May 2015).
4. Dario Amodei, D. H. *AI and compute* en-US. May 2018. <https://openai.com/research/ai-and-compute> (2023).
5. Sevilla, J. *et al. Compute Trends Across Three Eras of Machine Learning in 2022 International Joint Conference on Neural Networks (IJCNN)* ISSN: 2161-4407 (July 2022), 1–8.
6. Bohr, M. A 30 Year Retrospective on Dennard’s MOSFET Scaling Paper. *IEEE Solid-State Circuits Society Newsletter* **12**. Conference Name: IEEE Solid-State Circuits Society Newsletter, 11–13. ISSN: 1098-4232 (2007).
7. Horowitz, M. *1.1 Computing’s energy problem (and what we can do about it)* in *2014 IEEE International Solid-State Circuits Conference Digest of Technical Papers (ISSCC)* ISSN: 2376-8606 (Feb. 2014), 10–14.
8. Waldrop, M. M. The chips are down for Moore’s law. en. *Nature News* **530**. Cg_type: Nature News Section: News Feature, 144. <http://www.nature.com/news/the-chips-are-down-for-moore-s-law-1.19338> (2023) (Feb. 2016).

9. Miller, D. A. B. Attojoule Optoelectronics for Low-Energy Information Processing and Communications. *Journal of Lightwave Technology* **35**. Conference Name: Journal of Lightwave Technology, 346–396. ISSN: 1558-2213 (Feb. 2017).
10. Cardenas, J. *et al.* Low loss etchless silicon photonic waveguides. EN. *Opt. Express, OE* **17**. Publisher: Optica Publishing Group, 4752–4757. ISSN: 1094-4087. <https://opg.optica.org/oe/abstract.cfm?uri=oe-17-6-4752> (2022) (Mar. 2009).
11. Pfeiffer, M. H. P. *et al.* Photonic Damascene Process for Low-Loss, High-Confinement Silicon Nitride Waveguides. *IEEE Journal of Selected Topics in Quantum Electronics* **24**. Conference Name: IEEE Journal of Selected Topics in Quantum Electronics, 1–11. ISSN: 1558-4542 (July 2018).
12. Rahim, A. *et al.* Taking silicon photonics modulators to a higher performance level: state-of-the-art and a review of new technologies. *AP* **3**. Publisher: SPIE, 024003. ISSN: 2577-5421, 2577-5421. <https://www.spiedigitallibrary.org/journals/advanced-photonics/volume-3/issue-2/024003/Taking-silicon-photonics-modulators-to-a-higher-performance-level/10.1117/1.AP.3.2.024003.full> (2023) (Apr. 2021).
13. Lischke, S. *et al.* Ultra-fast germanium photodiode with 3-dB bandwidth of 265 GHz. en. *Nat. Photon.* **15**. Number: 12 Publisher: Nature Publishing Group, 925–931. ISSN: 1749-4893. <https://www.nature.com/articles/s41566-021-00893-w> (2023) (Dec. 2021).
14. Smith, D. R., Pendry, J. B. & Wiltshire, M. C. K. Metamaterials and Negative Refractive Index. *Science* **305**. Publisher: American Association for the Advancement of Science, 788–792. <https://www-science-org.login.ezproxy.library.ualberta.ca/doi/full/10.1126/science.1096796> (2023) (Aug. 2004).
15. Valentine, J. *et al.* Three-dimensional optical metamaterial with a negative refractive index. en. *Nature* **455**. Number: 7211 Publisher: Nature Publishing Group, 376–379. ISSN: 1476-4687. <https://www.nature.com/articles/nature07247> (2023) (Sept. 2008).
16. Tittl, A. *et al.* A Switchable Mid-Infrared Plasmonic Perfect Absorber with Multispectral Thermal Imaging Capability. *Advanced Materials* **27**, 4597–4603. ISSN: 1521-4095. <https://onlinelibrary.wiley.com/doi/abs/10.1002/adma.201502023> (2021) (2015).

17. Kim, J., Han, K. & Hahn, J. W. Selective dual-band metamaterial perfect absorber for infrared stealth technology. en. *Sci Rep* **7**. Number: 1 Publisher: Nature Publishing Group, 6740. ISSN: 2045-2322. <https://www.nature.com/articles/s41598-017-06749-0> (2023) (July 2017).
18. Wang, S. *et al.* A broadband achromatic metalens in the visible. en. *Nature Nanotech* **13**. Number: 3 Publisher: Nature Publishing Group, 227–232. ISSN: 1748-3395. <https://www.nature.com/articles/s41565-017-0052-4> (2023) (Mar. 2018).
19. Liu, W., Cheng, H., Tian, J. & Chen, S. Diffractive metalens: from fundamentals, practical applications to current trends. *Advances in Physics: X* **5**, 1742584. ISSN: null. <https://doi.org/10.1080/23746149.2020.1742584> (2023) (Jan. 2020).
20. Karvounis, A., Ou, J.-Y., Wu, W., MacDonald, K. F. & Zheludev, N. I. Nano-optomechanical nonlinear dielectric metamaterials. *Applied Physics Letters* **107**, 191110. ISSN: 0003-6951. <https://doi.org/10.1063/1.4935795> (2023) (Nov. 2015).
21. Ou, J. Y., Plum, E., Jiang, L. & Zheludev, N. I. Reconfigurable Photonic Metamaterials. *Nano Lett.* **11**. Publisher: American Chemical Society, 2142–2144. ISSN: 1530-6984. <https://doi.org/10.1021/nl200791r> (2023) (May 2011).
22. Valente, J., Ou, J.-Y., Plum, E., Youngs, I. J. & Zheludev, N. I. A magneto-electro-optical effect in a plasmonic nanowire material. en. *Nat Commun* **6**. Number: 1 Publisher: Nature Publishing Group, 7021. ISSN: 2041-1723. <https://www.nature.com/articles/ncomms8021> (2023) (Apr. 2015).
23. Ou, J.-Y., Plum, E., Zhang, J. & Zheludev, N. I. An electromechanically reconfigurable plasmonic metamaterial operating in the near-infrared. en. *Nature Nanotech* **8**. Number: 4 Publisher: Nature Publishing Group, 252–255. ISSN: 1748-3395. <https://www.nature.com/articles/nnano.2013.25> (2023) (Apr. 2013).
24. Dicken, M. J. *et al.* Frequency tunable near-infrared metamaterials based on VO₂ phase transition. EN. *Opt. Express, OE* **17**. Publisher: Optica Publishing Group, 18330–18339. ISSN: 1094-4087. <https://opg.optica.org/oe/abstract.cfm?uri=oe-17-20-18330> (2023) (Sept. 2009).

25. Werner, D. H., Kwon, D.-H., Khoo, I.-C., Kildishev, A. V. & Shalaev, V. M. Liquid crystal clad near-infrared metamaterials with tunable negative-zero-positive refractive indices. EN. *Opt. Express, OE* **15**. Publisher: Optica Publishing Group, 3342–3347. ISSN: 1094-4087. <https://opg.optica.org/oe/abstract.cfm?uri=oe-15-6-3342> (2023) (Mar. 2007).
26. Chen, H.-T. *et al.* Active terahertz metamaterial devices. en. *Nature* **444**. Number: 7119 Publisher: Nature Publishing Group, 597–600. ISSN: 1476-4687. <https://www.nature.com/articles/nature05343> (2023) (Nov. 2006).
27. Hand, T. & Cummer, S. Characterization of Tunable Metamaterial Elements Using MEMS Switches. *IEEE Antennas and Wireless Propagation Letters* **6**. Conference Name: IEEE Antennas and Wireless Propagation Letters, 401–404. ISSN: 1548-5757 (2007).
28. Abdollahramezani, S. *et al.* Tunable nanophotonics enabled by chalcogenide phase-change materials. en. *Nanophotonics* **9**. Publisher: De Gruyter, 1189–1241. ISSN: 2192-8614. <https://www.degruyter.com/document/doi/10.1515/nanoph-2020-0039/html> (2023) (May 2020).
29. Yamada, N. *et al.* High Speed Overwritable Phase Change Optical Disk Material. en. *Jpn. J. Appl. Phys.* **26**. Publisher: IOP Publishing, 61. ISSN: 1347-4065. <http://iopscience.iop.org/article/10.7567/JJAPS.26S4.61/meta> (2023) (Jan. 1987).
30. Zhang, Y. *et al.* Broadband transparent optical phase change materials for high-performance nonvolatile photonics. en. *Nat Commun* **10**. Number: 1 Publisher: Nature Publishing Group, 4279. ISSN: 2041-1723. <https://www.nature.com/articles/s41467-019-12196-4> (2022) (Sept. 2019).
31. Mandal, A., Cui, Y., McRae, L. & Gholipour, B. Reconfigurable chalcogenide phase change metamaterials: a material, device, and fabrication perspective. en. *J. Phys. Photonics* **3**. Publisher: IOP Publishing, 022005. ISSN: 2515-7647. <https://doi.org/10.1088/2515-7647/abe54d> (2021) (Mar. 2021).
32. Guerin, S., Hayden, B., Hewak, D. W. & Vian, C. Synthesis and Screening of Phase Change Chalcogenide Thin Film Materials for Data Storage. *ACS Comb. Sci.* **19**. Publisher: American Chemical Society, 478–491. ISSN: 2156-8952. <https://doi.org/10.1021/acscmbosci.7b00047> (2023) (July 2017).
33. Wuttig, M., Bhaskaran, H. & Taubner, T. Phase-change materials for non-volatile photonic applications. *Nature Photon* **11**. Number: 8 Publisher: Nature Publishing Group, 465–476. ISSN: 1749-4893. <https://www.nature.com/articles/nphoton.2017.126> (2023) (Aug. 2017).

34. Gholipour, B., Zhang, J., MacDonald, K. F., Hewak, D. W. & Zheludev, N. I. An All-Optical, Non-volatile, Bidirectional, Phase-Change Meta-Switch. *Advanced Materials* **25**, 3050–3054. ISSN: 1521-4095. <https://onlinelibrary.wiley.com/doi/abs/10.1002/adma.201300588> (2021) (2013).
35. Karvounis, A., Gholipour, B., MacDonald, K. F. & Zheludev, N. I. All-dielectric phase-change reconfigurable metasurface. *Appl. Phys. Lett.* **109**. Publisher: American Institute of Physics, 051103. ISSN: 0003-6951. <https://aip.scitation.org/doi/full/10.1063/1.4959272> (2021) (Aug. 2016).
36. Wang, Q. *et al.* Optically reconfigurable metasurfaces and photonic devices based on phase change materials. *Nature Photonics* **10**, 60–65. ISSN: 1749-4893. <https://doi.org/10.1038/nphoton.2015.247> (Jan. 2016).
37. Qin, S. *et al.* Near-infrared thermally modulated varifocal metalens based on the phase change material Sb_2S_3 . EN. *Opt. Express, OE* **29**. Publisher: Optica Publishing Group, 7925–7934. ISSN: 1094-4087. <https://opg.optica.org/oe/abstract.cfm?uri=oe-29-5-7925> (2023) (Mar. 2021).
38. Lin, R. J. *et al.* Achromatic metalens array for full-colour light-field imaging. en. *Nat. Nanotechnol.* **14**. Number: 3 Publisher: Nature Publishing Group, 227–231. ISSN: 1748-3395. <https://www.nature.com/articles/s41565-018-0347-0> (2023) (Mar. 2019).
39. Paniagua-Domínguez, R. *et al.* A Metalens with a Near-Unity Numerical Aperture. *Nano Lett.* **18**. Publisher: American Chemical Society, 2124–2132. ISSN: 1530-6984. <https://doi.org/10.1021/acs.nanolett.8b00368> (2023) (Mar. 2018).
40. Almeida, E., Bitton, O. & Prior, Y. Nonlinear metamaterials for holography. en. *Nat Commun* **7**. Number: 1 Publisher: Nature Publishing Group, 12533. ISSN: 2041-1723. <https://www.nature.com/articles/ncomms12533> (2023) (Aug. 2016).
41. Zhang, X. *et al.* Metasurface-based broadband hologram with high tolerance to fabrication errors. en. *Sci Rep* **6**. Number: 1 Publisher: Nature Publishing Group, 19856. ISSN: 2045-2322. <https://www.nature.com/articles/srep19856> (2023) (Jan. 2016).
42. Larouche, S., Tsai, Y.-J., Tyler, T., Jokerst, N. M. & Smith, D. R. Infrared metamaterial phase holograms. en. *Nature Mater* **11**. Number: 5 Publisher: Nature Publishing Group, 450–454. ISSN: 1476-4660. <https://www.nature.com/articles/nmat3278> (2023) (May 2012).

43. Plum, E., Fedotov, V. A. & Zheludev, N. I. Optical activity in extrinsically chiral metamaterial. *Applied Physics Letters* **93**, 191911. ISSN: 0003-6951. <https://doi.org/10.1063/1.3021082> (2023) (Nov. 2008).
44. Wang, Z., Cheng, F., Winsor, T. & Liu, Y. Optical chiral metamaterials: a review of the fundamentals, fabrication methods and applications. en. *Nanotechnology* **27**. Publisher: IOP Publishing, 412001. ISSN: 0957-4484. <https://dx.doi.org/10.1088/0957-4484/27/41/412001> (2023) (Sept. 2016).
45. Ma, W., Cheng, F. & Liu, Y. Deep-Learning-Enabled On-Demand Design of Chiral Metamaterials. *ACS Nano* **12**. Publisher: American Chemical Society, 6326–6334. ISSN: 1936-0851. <https://doi.org/10.1021/acsnano.8b03569> (2023) (June 2018).
46. Yang, J. *et al.* Photonic crystal fiber metalens. en. *Nanophotonics* **8**. Publisher: De Gruyter, 443–449. ISSN: 2192-8614. <https://www.degruyter.com/document/doi/10.1515/nanoph-2018-0204/html> (2023) (Mar. 2019).
47. Zhao, Q., Qu, J., Peng, G. & Yu, C. Endless Single-Mode Photonics Crystal Fiber Metalens for Broadband and Efficient Focusing in Near-Infrared Range. en. *Micromachines* **12**. Number: 2 Publisher: Multidisciplinary Digital Publishing Institute, 219. ISSN: 2072-666X. <https://www.mdpi.com/2072-666X/12/2/219> (2023) (Feb. 2021).
48. Hadibrata, W., Wei, H., Krishnaswamy, S. & Aydin, K. Inverse Design and 3D Printing of a Metalens on an Optical Fiber Tip for Direct Laser Lithography. *Nano Lett.* **21**. Publisher: American Chemical Society, 2422–2428. ISSN: 1530-6984. <https://doi.org/10.1021/acs.nanolett.0c04463> (2023) (Mar. 2021).
49. Zhou, C. *et al.* All-Dielectric Fiber Meta-Tip Enabling Vortex Generation and Beam Collimation for Optical Interconnect. en. *Laser & Photonics Reviews* **15**, 2000581. ISSN: 1863-8899. <https://onlinelibrary.wiley.com/doi/abs/10.1002/lpor.202000581> (2023) (2021).
50. Xomalis, A. *et al.* Fibre-optic metadvice for all-optical signal modulation based on coherent absorption. en. *Nat Commun* **9**. Number: 1 Publisher: Nature Publishing Group, 182. ISSN: 2041-1723. <https://www.nature.com/articles/s41467-017-02434-y> (2023) (Jan. 2018).
51. Reed, G. T., Mashanovich, G., Gardes, F. Y. & Thomson, D. J. Silicon optical modulators. en. *Nature Photon* **4**. Number: 8 Publisher: Nature Publishing Group, 518–526. ISSN: 1749-4893. <https://www.nature.com/articles/nphoton.2010.179> (2022) (Aug. 2010).

52. Kohli, N., Sang, B. L., Nabki, F. & Menard, M. Tunable Bandpass Filter with Serially Coupled Ring Resonators Assisted MZI. *IEEE Photonics Journal*. Conference Name: IEEE Photonics Journal, 1–1. ISSN: 1943-0655 (2021).
53. Mao, D. *et al.* Adiabatic Coupler With Design-Intended Splitting Ratio. *Journal of Lightwave Technology* **37**. Conference Name: Journal of Lightwave Technology, 6147–6155. ISSN: 1558-2213 (Dec. 2019).
54. Xu, Y., Tian, Z., Meng, X. & Chai, Z. Methods and applications of on-chip beam splitting: A review. *Frontiers in Physics* **10**. ISSN: 2296-424X. <https://www.frontiersin.org/articles/10.3389/fphy.2022.985208> (2022) (2022).
55. Cai, J. *et al.* Design Optimization of Silicon and Lithium Niobate Hybrid Integrated Traveling-Wave Mach-Zehnder Modulator. *IEEE Photonics Journal* **13**. Conference Name: IEEE Photonics Journal, 1–6. ISSN: 1943-0655 (Aug. 2021).
56. Harris, N. C. *et al.* Efficient, compact and low loss thermo-optic phase shifter in silicon. EN. *Opt. Express, OE* **22**. Publisher: Optica Publishing Group, 10487–10493. ISSN: 1094-4087. <https://opg.optica.org/oe/abstract.cfm?uri=oe-22-9-10487> (2022) (May 2014).
57. Li, Q., Han, J.-H., Ho, C. P., Takagi, S. & Takenaka, M. Ultra-power-efficient 2x2 Si Mach-Zehnder interferometer optical switch based on III-V/Si hybrid MOS phase shifter. EN. *Opt. Express, OE* **26**. Publisher: Optica Publishing Group, 35003–35012. ISSN: 1094-4087. <https://opg.optica.org/oe/abstract.cfm?uri=oe-26-26-35003> (2022) (Dec. 2018).
58. Iseghem, L. V. *et al.* Low power optical phase shifter using liquid crystal actuation on a silicon photonics platform. EN. *Opt. Mater. Express, OME* **12**. Publisher: Optica Publishing Group, 2181–2198. ISSN: 2159-3930. <https://opg.optica.org/ome/abstract.cfm?uri=ome-12-6-2181> (2022) (June 2022).
59. Sun, H., Qiao, Q., Guan, Q. & Zhou, G. Silicon Photonic Phase Shifters and Their Applications: A Review. en. *Micromachines* **13**. Number: 9 Publisher: Multidisciplinary Digital Publishing Institute, 1509. ISSN: 2072-666X. <https://www.mdpi.com/2072-666X/13/9/1509> (2022) (Sept. 2022).
60. Bogaerts, W. *et al.* Silicon microring resonators. en. *Laser & Photonics Reviews* **6**, 47–73. ISSN: 1863-8899. <https://onlinelibrary.wiley.com/doi/abs/10.1002/lpor.201100017> (2022) (2012).

61. Naraine, C. M. *et al.* Subwavelength Grating Metamaterial Waveguides and Ring Resonators on a Silicon Nitride Platform. en. *Laser & Photonics Reviews* **17**, 2200216. ISSN: 1863-8899. <https://onlinelibrary.wiley.com/doi/abs/10.1002/lpor.202200216> (2023) (2023).
62. Van, V. *Optical Microring Resonators: Theory, Techniques, and Applications* en. Google-Books-ID: _woNDgAAQBAJ. ISBN: 978-1-315-30350-5 (CRC Press, Dec. 2016).
63. Harris, N. C. *et al.* Linear programmable nanophotonic processors. EN. *Optica, OPTICA* **5**. Publisher: Optica Publishing Group, 1623–1631. ISSN: 2334-2536. <https://opg.optica.org/optica/abstract.cfm?uri=optica-5-12-1623> (2022) (Dec. 2018).
64. Bogaerts, W. *et al.* Programmable photonic circuits. en. *Nature* **586**. Number: 7828 Publisher: Nature Publishing Group, 207–216. ISSN: 1476-4687. <https://www.nature.com/articles/s41586-020-2764-0> (2022) (Oct. 2020).
65. Reck, M., Zeilinger, A., Bernstein, H. J. & Bertani, P. Experimental realization of any discrete unitary operator. *Phys. Rev. Lett.* **73**. Publisher: American Physical Society, 58–61. <https://link.aps.org/doi/10.1103/PhysRevLett.73.58> (2022) (July 1994).
66. Shen, Y. *et al.* Deep learning with coherent nanophotonic circuits. en. *Nature Photon* **11**. Number: 7 Publisher: Nature Publishing Group, 441–446. ISSN: 1749-4893. <https://www.nature.com/articles/nphoton.2017.93> (2022) (July 2017).
67. Shokraneh, F., Nezami, M. S. & Liboiron-Ladouceur, O. Theoretical and Experimental Analysis of a 4×4 Reconfigurable MZI-Based Linear Optical Processor. *Journal of Lightwave Technology* **38**. Conference Name: Journal of Lightwave Technology, 1258–1267. ISSN: 1558-2213 (Mar. 2020).
68. Yang, L., Ji, R., Zhang, L., Ding, J. & Xu, Q. On-chip CMOS-compatible optical signal processor. EN. *Opt. Express, OE* **20**. Publisher: Optica Publishing Group, 13560–13565. ISSN: 1094-4087. <https://opg.optica.org/oe/abstract.cfm?uri=oe-20-12-13560> (2023) (June 2012).
69. Tait, A. N., Nahmias, M. A., Shastri, B. J. & Prucnal, P. R. Broadcast and Weight: An Integrated Network For Scalable Photonic Spike Processing. EN. *J. Lightwave Technol., JLT* **32**. Publisher: IEEE, 3427–3439. <https://opg.optica.org/jlt/abstract.cfm?uri=jlt-32-21-3427> (2022) (Nov. 2014).

70. Rios, C., Hosseini, P., Wright, C. D., Bhaskaran, H. & Pernice, W. H. P. On-Chip Photonic Memory Elements Employing Phase-Change Materials. *Advanced Materials* **26**, 1372–1377. ISSN: 1521-4095. <http://onlinelibrary.wiley.com/doi/abs/10.1002/adma.201304476> (2021) (2014).
71. Zhang, H. *et al.* Ultracompact Si-GST Hybrid Waveguides for Nonvolatile Light Wave Manipulation. *IEEE Photonics Journal* **10**. Conference Name: IEEE Photonics Journal, 1–10. ISSN: 1943-0655 (Feb. 2018).
72. Faneca, J. *et al.* Towards low loss non-volatile phase change materials in mid index waveguides. en. *Neuromorph. Comput. Eng.* **1**. Publisher: IOP Publishing, 014004. ISSN: 2634-4386. <https://dx.doi.org/10.1088/2634-4386/ac156e> (2023) (Aug. 2021).
73. Delaney, M. *et al.* Nonvolatile programmable silicon photonics using an ultralow-loss Sb₂Se₃ phase change material. *Science Advances* **7**. Publisher: American Association for the Advancement of Science, eabg3500. <https://www.science.org/doi/10.1126/sciadv.abg3500> (2022) (June 2021).
74. Ríos, C. *et al.* Integrated all-photonic non-volatile multi-level memory. en. *Nature Photon* **9**. Number: 11 Publisher: Nature Publishing Group, 725–732. ISSN: 1749-4893. <https://www.nature.com/articles/nphoton.2015.182> (2022) (Nov. 2015).
75. Zheng, J. *et al.* GST-on-silicon hybrid nanophotonic integrated circuits: a non-volatile quasi-continuously reprogrammable platform. EN. *Opt. Mater. Express, OME* **8**. Publisher: Optical Society of America, 1551–1561. ISSN: 2159-3930. <http://www.osapublishing.org/ome/abstract.cfm?uri=ome-8-6-1551> (2021) (June 2018).
76. Wu, C. *et al.* Low-Loss Integrated Photonic Switch Using Subwavelength Patterned Phase Change Material. *ACS Photonics* **6**. Publisher: American Chemical Society, 87–92. <https://doi.org/10.1021/acsp Photonics.8b01516> (2022) (Jan. 2019).
77. Richardson, D. J., Fini, J. M. & Nelson, L. E. Space-division multiplexing in optical fibres. en. *Nature Photon* **7**. Number: 5 Publisher: Nature Publishing Group, 354–362. ISSN: 1749-4893. <https://www.nature.com/articles/nphoton.2013.94> (2023) (May 2013).
78. Li, G., Bai, N., Zhao, N. & Xia, C. Space-division multiplexing: the next frontier in optical communication. EN. *Adv. Opt. Photon., AOP* **6**. Publisher: Optica Publishing Group, 413–487. ISSN: 1943-8206. <https://opg.optica.org/aop/abstract.cfm?uri=aop-6-4-413> (2023) (Dec. 2014).

79. Zhang, H. *et al.* Molybdenum disulfide (MoS₂) as a broadband saturable absorber for ultra-fast photonics. EN. *Opt. Express, OE* **22**. Publisher: Optica Publishing Group, 7249–7260. ISSN: 1094-4087. <https://opg.optica.org/oe/abstract.cfm?uri=oe-22-6-7249> (2023) (Mar. 2014).
80. Gholipour, B. *et al.* Amorphous Metal-Sulphide Microfibers Enable Photonic Synapses for Brain-Like Computing. *Advanced Optical Materials* **3**, 635–641. ISSN: 2195-1071. <https://onlinelibrary.wiley.com/doi/abs/10.1002/adom.201400472> (2022) (2015).
81. Dudley, J. M. & Taylor, J. R. Ten years of nonlinear optics in photonic crystal fibre. en. *Nature Photon* **3**. Number: 2 Publisher: Nature Publishing Group, 85–90. ISSN: 1749-4893. <https://www.nature.com/articles/nphoton.2008.285> (2023) (Feb. 2009).
82. Danto, S., Ruff, Z., Wang, Z., Joannopoulos, J. D. & Fink, Y. Ovonic Memory Switching in Multimaterial Fibers. en. *Advanced Functional Materials* **21**, 1095–1101. ISSN: 1616-3028. <https://onlinelibrary.wiley.com/doi/abs/10.1002/adfm.201002252> (2023) (2011).
83. Gholipour, B. *et al.* Lithography Assisted Fiber-Drawing Nanomanufacturing. en. *Sci Rep* **6**. Number: 1 Publisher: Nature Publishing Group, 35409. ISSN: 2045-2322. <https://www.nature.com/articles/srep35409> (2023) (Oct. 2016).
84. Abouraddy, A. F. *et al.* Towards multimaterial multifunctional fibres that see, hear, sense and communicate. en. *Nature Mater* **6**. Number: 5 Publisher: Nature Publishing Group, 336–347. ISSN: 1476-4660. <https://www.nature.com/articles/nmat1889> (2023) (May 2007).
85. Savinov, V. & Zheludev, N. I. High-quality metamaterial dispersive grating on the facet of an optical fiber. *Applied Physics Letters* **111**, 091106. ISSN: 0003-6951. <https://doi.org/10.1063/1.4990766> (2023) (Aug. 2017).
86. Piccinotti, D., MacDonald, K. F., Gregory, S. A., Youngs, I. & Zheludev, N. I. Artificial intelligence for photonics and photonic materials. en. *Rep. Prog. Phys.* **84**. Publisher: IOP Publishing, 012401. ISSN: 0034-4885. <https://dx.doi.org/10.1088/1361-6633/abb4c7> (2023) (Dec. 2020).
87. Feldmann, J., Youngblood, N., Wright, C. D., Bhaskaran, H. & Pernice, W. H. P. All-optical spiking neurosynaptic networks with self-learning capabilities. en. *Nature* **569**. Number: 7755 Publisher: Nature Publishing Group, 208–214. ISSN: 1476-4687. <https://www.nature.com/articles/s41586-019-1157-8> (2022) (May 2019).

88. Martins, T. *et al.* Fiber-integrated phase-change reconfigurable optical attenuator. *APL Photonics* **4**. Publisher: American Institute of Physics, 111301. <https://aip.scitation.org/doi/full/10.1063/1.5116000> (2021) (Nov. 2019).
89. Zhang, H. *et al.* Optical-resonance-enhanced nonlinearities in a MoS₂-coated single-mode fiber. EN. *Opt. Lett., OL* **43**. Publisher: Optica Publishing Group, 3100–3103. ISSN: 1539-4794. <https://opg.optica.org/ol/abstract.cfm?uri=ol-43-13-3100> (2023) (July 2018).
90. Bao, Q. *et al.* Broadband graphene polarizer. en. *Nature Photon* **5**. Number: 7 Publisher: Nature Publishing Group, 411–415. ISSN: 1749-4893. <https://www.nature.com/articles/nphoton.2011.102> (2023) (July 2011).
91. Zhao, Y., Zhang, J., Du, J. & Wang, J. Meta-facet fiber for twisting ultra-broadband light with high phase purity. *Applied Physics Letters* **113**, 061103. ISSN: 0003-6951. <https://doi.org/10.1063/1.5043268> (2023) (Aug. 2018).
92. Urbas, A. M. *et al.* Roadmap on optical metamaterials. en. *J. Opt.* **18**. Publisher: IOP Publishing, 093005. ISSN: 2040-8986. <https://dx.doi.org/10.1088/2040-8978/18/9/093005> (2023) (Aug. 2016).
93. Zheludev, N. I. & Kivshar, Y. S. From metamaterials to metadevices. en. *Nature Mater* **11**. Number: 11 Publisher: Nature Publishing Group, 917–924. ISSN: 1476-4660. <https://www.nature.com/articles/nmat3431> (2023) (Nov. 2012).
94. Stockman, M. I. *et al.* Roadmap on plasmonics. en. *J. Opt.* **20**. Publisher: IOP Publishing, 043001. ISSN: 2040-8986. <https://dx.doi.org/10.1088/2040-8986/aaa114> (2023) (Mar. 2018).
95. Perkins, J. & Gholipour, B. Optoelectronic Gas Sensing Platforms: From Metal Oxide Lambda Sensors to Nanophotonic Metamaterials. en. *Advanced Photonics Research* **2**, 2000141. ISSN: 2699-9293. <https://onlinelibrary.wiley.com/doi/abs/10.1002/adpr.202000141> (2023) (2021).
96. Eggleton, B. J., Luther-Davies, B. & Richardson, K. Chalcogenide photonics. en. *Nature Photon* **5**. Number: 3 Publisher: Nature Publishing Group, 141–148. ISSN: 1749-4893. <https://www.nature.com/articles/nphoton.2011.309> (2023) (Mar. 2011).
97. Huang, C.-C. *et al.* Scalable high-mobility MoS₂ thin films fabricated by an atmospheric pressure chemical vapor deposition process at ambient temperature. en. *Nanoscale* **6**. Publisher: Royal Society of Chemistry, 12792–12797. <https://pubs.rsc.org/en/content/articlelanding/2014/nr/c4nr04228j> (2023) (2014).

98. Huang, C. C., Gholipour, B., Ou, J. Y., Knight, K. & Hewak, D. W. Electrical phase change of CVD-grown Ge-Sb-Te thin-film device. en. *Electronics Letters* **47**. Publisher: IET Digital Library, 288–289. ISSN: 1350-911X. <https://digital-library.theiet.org/content/journals/10.1049/el.2010.3276> (2023) (Feb. 2011).
99. Hughes, M. A. *et al.* Ion-implantation-enhanced chalcogenide-glass resistive-switching devices. *Applied Physics Letters* **105**, 083506. ISSN: 0003-6951. <https://doi.org/10.1063/1.4894245> (2023) (Aug. 2014).
100. Loke, D. *et al.* Breaking the Speed Limits of Phase-Change Memory. *Science* **336**. Publisher: American Association for the Advancement of Science, 1566–1569. <https://www.science.org/doi/full/10.1126/science.1221561> (2023) (June 2012).
101. Wuttig, M. & Yamada, N. Phase-change materials for rewriteable data storage. en. *Nature Mater* **6**. Number: 11 Publisher: Nature Publishing Group, 824–832. ISSN: 1476-4660. <https://www.nature.com/articles/nmat2009> (2023) (Nov. 2007).
102. Hughes, M. A. *et al.* n-type chalcogenides by ion implantation. en. *Nat Commun* **5**. Number: 1 Publisher: Nature Publishing Group, 5346. ISSN: 2041-1723. <https://www.nature.com/articles/ncomms6346> (2023) (Nov. 2014).
103. Piccinotti, D. *et al.* Stoichiometric Engineering of Chalcogenide Semiconductor Alloys for Nanophotonic Applications. *Advanced Materials* **31**. Publisher: John Wiley & Sons, Ltd, 1807083. ISSN: 0935-9648. <https://doi.org/10.1002/adma.201807083> (2021) (Apr. 2019).
104. Schlich, F. F., Zalden, P., Lindenberg, A. M. & Spolenak, R. Color Switching with Enhanced Optical Contrast in Ultrathin Phase-Change Materials and Semiconductors Induced by Femtosecond Laser Pulses. *ACS Photonics* **2**. Publisher: American Chemical Society, 178–182. <https://doi.org/10.1021/ph500402r> (2023) (Feb. 2015).
105. Zhang, Y. *et al.* Electrically reconfigurable non-volatile metasurface using low-loss optical phase-change material. en. *Nat. Nanotechnol.* **16**. Number: 6 Publisher: Nature Publishing Group, 661–666. ISSN: 1748-3395. <https://www.nature.com/articles/s41565-021-00881-9> (2023) (June 2021).
106. Gholipour, B. *et al.* Phase-change-driven dielectric-plasmonic transitions in chalcogenide metasurfaces. en. *NPG Asia Mater* **10**, 533–539. ISSN: 1884-4057. <https://www.nature.com/articles/s41427-018-0043-4> (2021) (June 2018).
107. *Ansys Lumerical FDTD — Simulation for Photonic Components* en-US. <https://www.ansys.com/products/photronics/fdtd> (2023).

108. Giewont, K. *et al.* 300-mm Monolithic Silicon Photonics Foundry Technology. *IEEE Journal of Selected Topics in Quantum Electronics* **25**. Conference Name: IEEE Journal of Selected Topics in Quantum Electronics, 1–11. ISSN: 1558-4542 (Sept. 2019).
109. *NanoSOI Fabrication Service — Applied Nanotools Inc.* <https://www.appliednt.com/nanosoi-fabrication-service/>.
110. Kato, K., Kuwahara, M., Kawashima, H., Tsuruoka, T. & Tsuda, H. Current-driven phase-change optical gate switch using indium–tin-oxide heater. en. *Appl. Phys. Express* **10**. Publisher: IOP Publishing, 072201. ISSN: 1882-0786. <https://iopscience.iop.org/article/10.7567/APEX.10.072201/meta> (2022) (June 2017).
111. Pernice, W. H. P. & Bhaskaran, H. Photonic non-volatile memories using phase change materials. en. *Applied Physics Letters* **101**. Publisher: American Institute of PhysicsAIP, 171101. ISSN: 0003-6951. <https://aip.scitation.org/doi/abs/10.1063/1.4758996> (2022) (Oct. 2012).
112. Zheng, J., Zhu, S., Xu, P., Dunham, S. & Majumdar, A. Modeling Electrical Switching of Nonvolatile Phase-Change Integrated Nanophotonic Structures with Graphene Heaters. *ACS Appl. Mater. Interfaces* **12**. Publisher: American Chemical Society, 21827–21836. ISSN: 1944-8244. <https://doi.org/10.1021/acsam.0c02333> (2022) (May 2020).
113. Taghinejad, H. *et al.* ITO-based microheaters for reversible multi-stage switching of phase-change materials: towards miniaturized beyond-binary reconfigurable integrated photonics. EN. *Opt. Express, OE* **29**. Publisher: Optica Publishing Group, 20449–20462. ISSN: 1094-4087. <https://opg.optica.org/oe/abstract.cfm?uri=oe-29-13-20449> (2023) (June 2021).
114. Erickson, J. R. *et al.* Designing fast and efficient electrically driven phase change photonics using foundry compatible waveguide-integrated microheaters. EN. *Opt. Express, OE* **30**. Publisher: Optica Publishing Group, 13673–13689. ISSN: 1094-4087. <https://opg.optica.org/oe/abstract.cfm?uri=oe-30-8-13673> (2022) (Apr. 2022).
115. Farmakidis, N. *et al.* Electronically Reconfigurable Photonic Switches Incorporating Plasmonic Structures and Phase Change Materials. en. *Advanced Science* **9**, 2200383. ISSN: 2198-3844. <https://onlinelibrary.wiley.com/doi/abs/10.1002/advs.202200383> (2022) (2022).

116. Padmaraju, K. & Bergman, K. Resolving the thermal challenges for silicon microring resonator devices. en. *Nanophotonics* **3**. Publisher: De Gruyter, 269–281. ISSN: 2192-8614. <https://www.degruyter.com/document/doi/10.1515/nanoph-2013-0013/html?lang=de> (2022) (Aug. 2014).
117. Cheben, P., Halir, R., Schmid, J. H., Atwater, H. A. & Smith, D. R. Sub-wavelength integrated photonics. en. *Nature* **560**. Number: 7720 Publisher: Nature Publishing Group, 565–572. ISSN: 1476-4687. <https://www.nature.com/articles/s41586-018-0421-7> (2023) (Aug. 2018).
118. Cocorullo, G., Della Corte, F. G. & Rendina, I. Temperature dependence of the thermo-optic coefficient in crystalline silicon between room temperature and 550 K at the wavelength of 1523 nm. *Appl. Phys. Lett.* **74**. Publisher: American Institute of Physics, 3338–3340. ISSN: 0003-6951. <https://aip.scitation.org/doi/abs/10.1063/1.123337> (2022) (May 1999).
119. Kim, Y., Han, J.-H., Ahn, D. & Kim, S. Heterogeneously-Integrated Optical Phase Shifters for Next-Generation Modulators and Switches on a Silicon Photonics Platform: A Review. en. *Micromachines* **12**. Number: 6 Publisher: Multidisciplinary Digital Publishing Institute, 625. ISSN: 2072-666X. <https://www.mdpi.com/2072-666X/12/6/625> (2023) (June 2021).
120. Maegami, Y. *et al.* High-efficiency strip-loaded waveguide based silicon Mach-Zehnder modulator with vertical p-n junction phase shifter. EN. *Opt. Express, OE* **25**. Publisher: Optica Publishing Group, 31407–31416. ISSN: 1094-4087. <https://opg.optica.org/oe/abstract.cfm?uri=oe-25-25-31407> (2023) (Dec. 2017).
121. Liu, S. *et al.* Thermo-optic phase shifters based on silicon-on-insulator platform: state-of-the-art and a review. en. *Front. Optoelectron.* **15**, 9. ISSN: 2095-2767. <https://doi.org/10.1007/s12200-022-00012-9> (2023) (Apr. 2022).
122. Alam, M. Z., De Leon, I. & Boyd, R. W. Large optical nonlinearity of indium tin oxide in its epsilon-near-zero region. *Science* **352**. Publisher: American Association for the Advancement of Science, 795–797. <https://www.science.org/doi/full/10.1126/science.aae0330> (2023) (May 2016).
123. Cocorullo, G. & Rendina, I. Thermo-optical modulation at 1.5 μ m in silicon etalon. en. *Electronics Letters* **28**. Publisher: IET Digital Library, 83–85. ISSN: 1350-911X. <https://digital-library.theiet.org/content/journals/10.1049/el.19920051> (2023) (Jan. 1992).

124. Soref, R. A. & Bennett, B. R. *Kramers-Kronig Analysis Of Electro-Optical Switching In Silicon* in *Integrated Optical Circuit Engineering IV* **0704** (SPIE, Mar. 1987), 32–37. <https://www.spiedigitallibrary.org/conference-proceedings-of-spie/0704/0000/Kramers-Kronig-Analysis-Of-Electro-Optical-Switching-In-Silicon/10.1117/12.937193.full> (2023).
125. Liu, A. *et al.* Recent development in a high-speed silicon optical modulator based on reverse-biased pn diode in a silicon waveguide. en. *Semicond. Sci. Technol.* **23**, 064001. ISSN: 0268-1242. <https://dx.doi.org/10.1088/0268-1242/23/6/064001> (2023) (May 2008).
126. Luke, K., Dutt, A., Poitras, C. B. & Lipson, M. Overcoming Si₃N₄ film stress limitations for high quality factor ring resonators. EN. *Opt. Express, OE* **21**. Publisher: Optical Society of America, 22829–22833. ISSN: 1094-4087. <https://www.osapublishing.org/oe/abstract.cfm?uri=oe-21-19-22829> (2021) (Sept. 2013).
127. Nam, K. H., Park, I. H. & Ko, S. H. Patterning by controlled cracking. en. *Nature* **485**, 221–224. ISSN: 1476-4687 (May 2012).
128. Yariv, A. Coupled-mode theory for guided-wave optics. *IEEE Journal of Quantum Electronics* **9**. Conference Name: IEEE Journal of Quantum Electronics, 919–933. ISSN: 1558-1713 (Sept. 1973).
129. Kennedy, J. & Eberhart, R. *Particle swarm optimization* in *Proceedings of ICNN'95 - International Conference on Neural Networks* **4** (Nov. 1995), 1942–1948 vol.4.
130. Wang, Y., Flueckiger, J., Lin, C. & Chrostowski, L. *Universal grating coupler design* in *Photonics North 2013* **8915** (SPIE, Oct. 2013), 284–290. <https://www.spiedigitallibrary.org/conference-proceedings-of-spie/8915/89150Y/Universal-grating-coupler-design/10.1117/12.2042185.full> (2023).
131. Cheng, L., Mao, S., Li, Z., Han, Y. & Fu, H. Y. Grating Couplers on Silicon Photonics: Design Principles, Emerging Trends and Practical Issues. en. *Micromachines* **11**. Number: 7 Publisher: Multidisciplinary Digital Publishing Institute, 666. ISSN: 2072-666X. <https://www.mdpi.com/2072-666X/11/7/666> (2022) (July 2020).
132. Roelkens, G., Thourhout, D. V. & Baets, R. High efficiency Silicon on Insulator grating coupler based on a poly-Silicon overlay. EN. *Opt. Express, OE* **14**. Publisher: Optica Publishing Group, 11622–11630. ISSN: 1094-4087. <https://opg.optica.org/oe/abstract.cfm?uri=oe-14-24-11622> (2023) (Nov. 2006).

133. Ding, Y., Peucheret, C., Ou, H. & Yvind, K. Fully etched apodized grating coupler on the SOI platform with 0.58dB coupling efficiency. EN. *Opt. Lett., OL* **39**. Publisher: Optica Publishing Group, 5348–5350. ISSN: 1539-4794. <https://opg.optica.org/ol/abstract.cfm?uri=ol-39-18-5348> (2023) (Sept. 2014).
134. Vermeulen, D. *et al.* High-efficiency fiber to chip grating couplers realized using an advanced CMOS compatible Silicon On Insulator platform. EN. *Opt. Express, OE* **18**. Publisher: Optica Publishing Group, 18278–18283. ISSN: 1094-4087. <https://opg.optica.org/oe/abstract.cfm?uri=oe-18-17-18278> (2023) (Aug. 2010).
135. Marchetti, R. *et al.* High-efficiency grating-couplers: demonstration of a new design strategy. en. *Sci Rep* **7**. Number: 1 Publisher: Nature Publishing Group, 16670. ISSN: 2045-2322. <https://www.nature.com/articles/s41598-017-16505-z> (2023) (Nov. 2017).
136. Sethi, P., Haldar, A. & Selvaraja, S. K. Ultra-compact low-loss broadband waveguide taper in silicon-on-insulator. EN. *Opt. Express, OE* **25**. Publisher: Optica Publishing Group, 10196–10203. ISSN: 1094-4087. <https://opg.optica.org/oe/abstract.cfm?uri=oe-25-9-10196> (2023) (May 2017).
137. Chang, T. H. P. Proximity effect in electron-beam lithography. *Journal of Vacuum Science and Technology* **12**, 1271–1275. ISSN: 0022-5355. <https://doi.org/10.1116/1.568515> (2023) (Nov. 1975).
138. Ren, L. & Chen, B. *Proximity effect in electron beam lithography* in *Proceedings. 7th International Conference on Solid-State and Integrated Circuits Technology, 2004*. **1** (Oct. 2004), 579–582 vol.1.
139. Hryciw, A. *Raith_GDSII MATLAB toolbox* original-date: 2021-09-22T16:37:55Z. Feb. 2023. https://github.com/ahryciw/Raith_GDSII (2023).
140. Fang, Z. *et al.* Ultra-low-energy programmable non-volatile silicon photonics based on phase-change materials with graphene heaters. en. *Nat. Nanotechnol.* Publisher: Nature Publishing Group, 1–7. ISSN: 1748-3395. <https://www.nature.com/articles/s41565-022-01153-w> (2022) (July 2022).
141. Martin-Monier, L. *et al.* Endurance of chalcogenide optical phase change materials: a review. EN. *Opt. Mater. Express, OME* **12**. Publisher: Optica Publishing Group, 2145–2167. ISSN: 2159-3930. <https://opg.optica.org/ome/abstract.cfm?uri=ome-12-6-2145> (2022) (June 2022).
142. Selden, A. C. Pulse transmission through a saturable absorber. *British Journal of Applied Physics* **18**, 743. <https://dx.doi.org/10.1088/0508-3443/18/6/306> (1967).

143. Cheng, Z., Tsang, H. K., Wang, X., Xu, K. & Xu, J.-B. In-Plane Optical Absorption and Free Carrier Absorption in Graphene-on-Silicon Waveguides. *IEEE Journal of Selected Topics in Quantum Electronics* **20**, 43–48 (2014).

Appendix A: Fiber-integrated phase change metasurface with switchable group delay dispersion

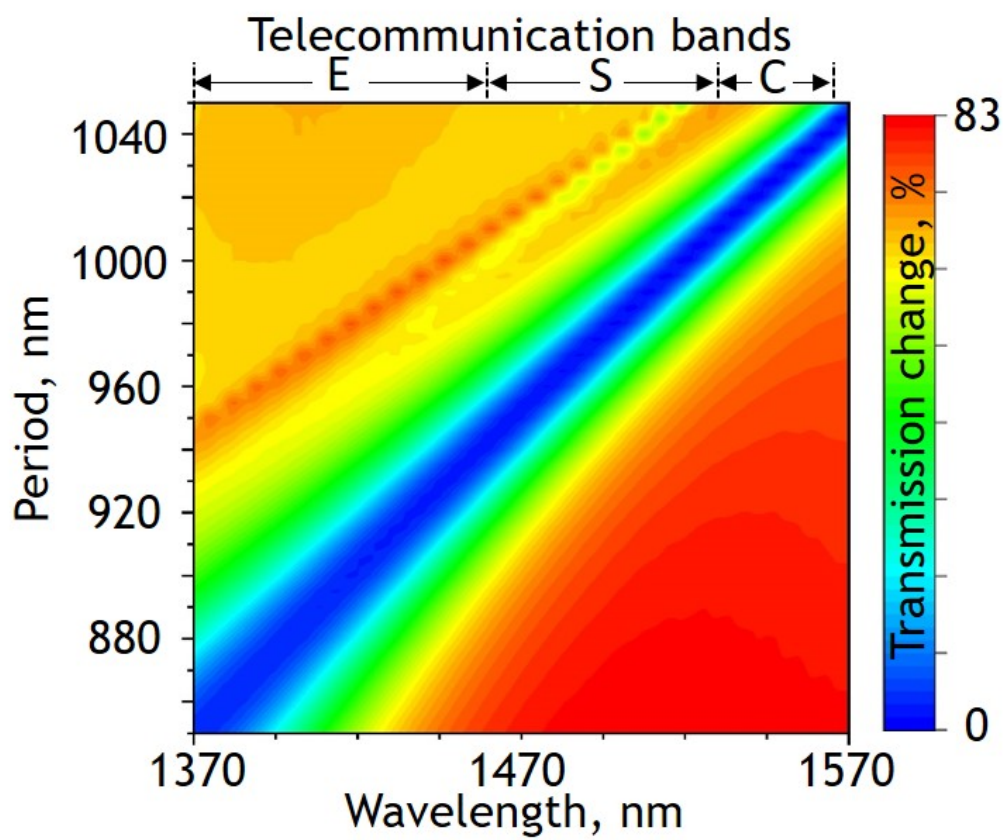


Figure A.1: Numerically simulated change in transmission between amorphous and crystalline phases for metasurface ranging from 850nm to 1050nm periods.

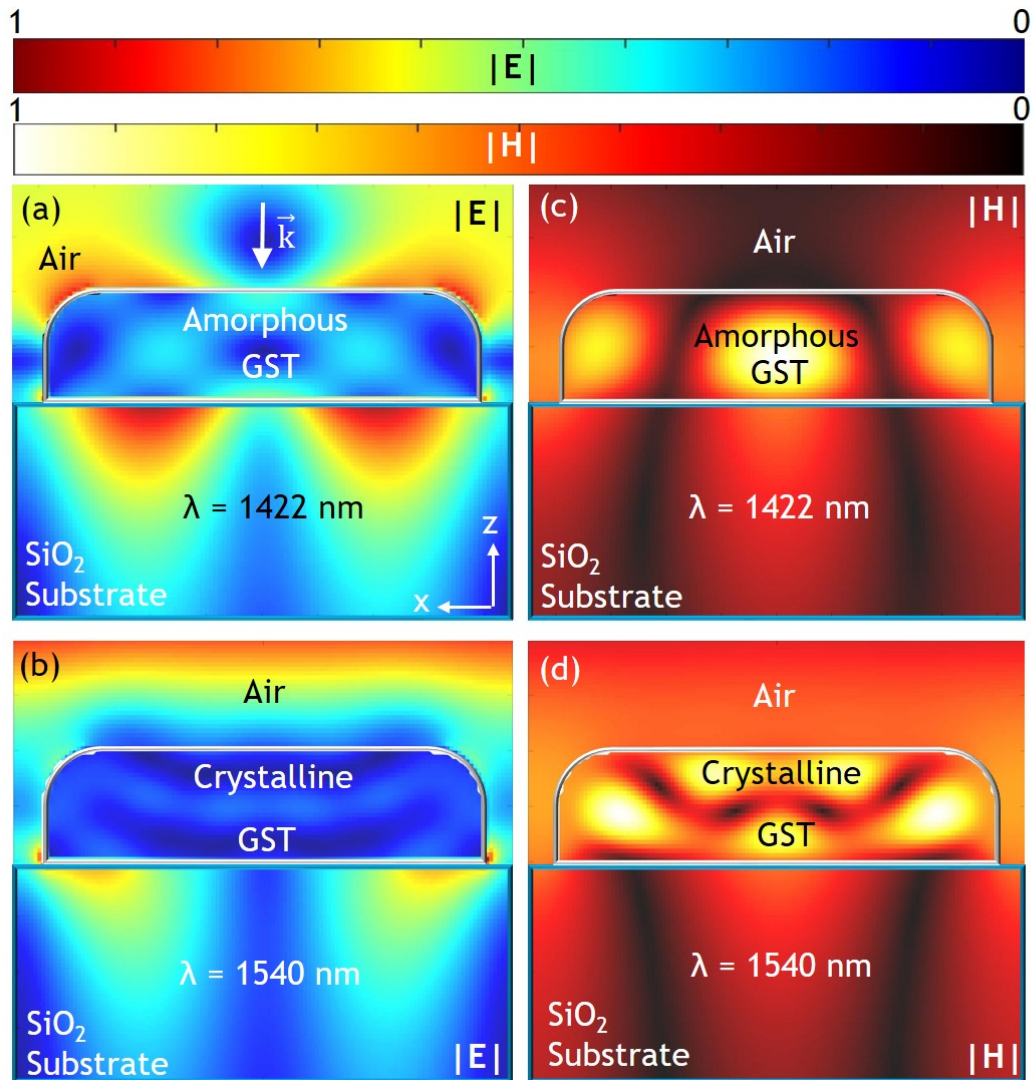


Figure A.2: Electric (a.,b.) and magnetic (c.,d.) field distribution of a metasurface with $w = 80nm$, $t = 200nm$, and $P = 900nm$, in the amorphous (a.,c.) and crystalline (b.,d.) crystalline phases; plotted at their respective resonance wavelengths.

Appendix B: Chalcogenide phase change MZI phase-shifters

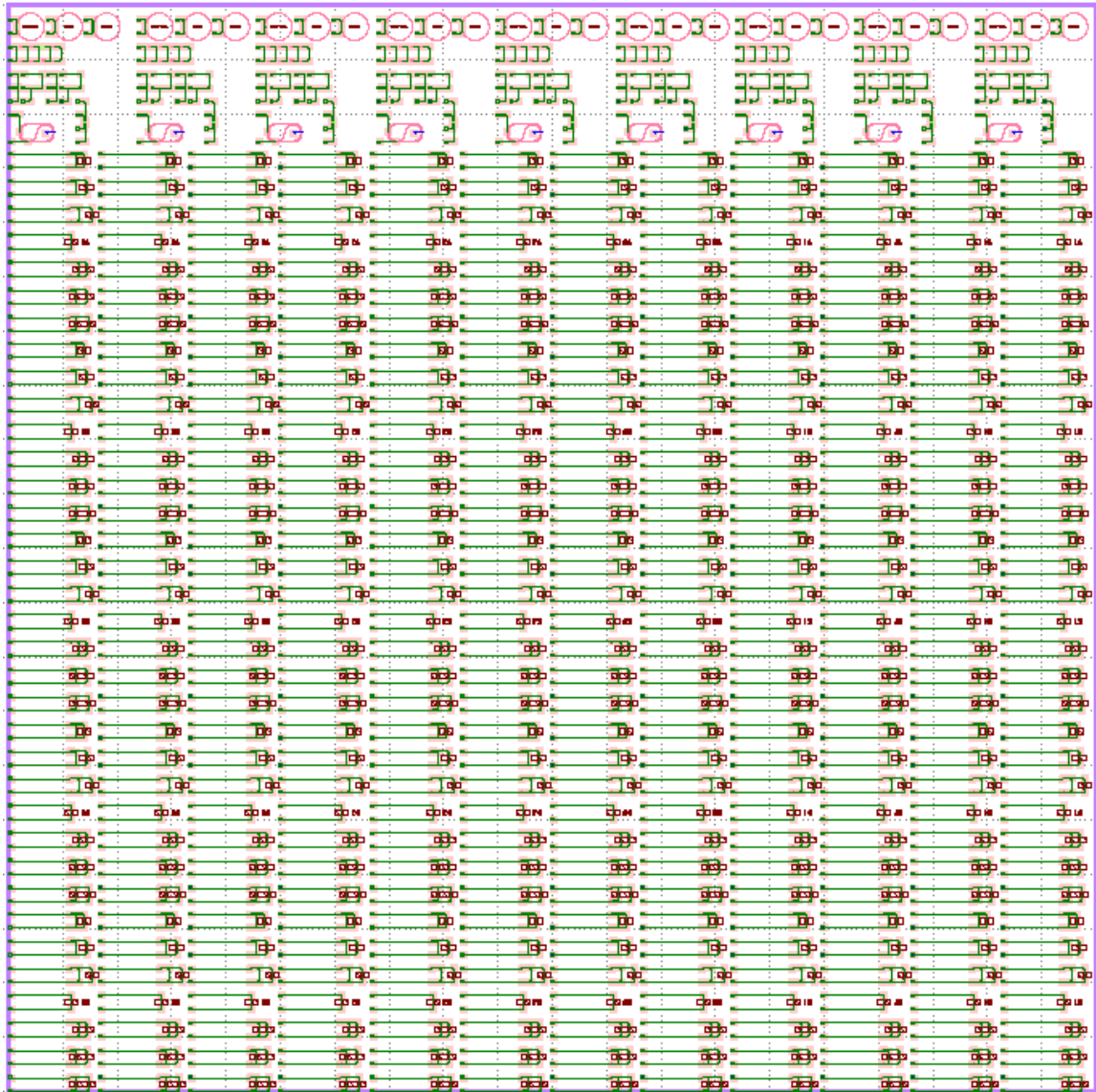


Figure B.1: GDS layout of sample photonic chip submitted for fabrication with Applied Nanotools containing various MZI circuit configurations with PCM and passive photonic calibration circuits for testing.

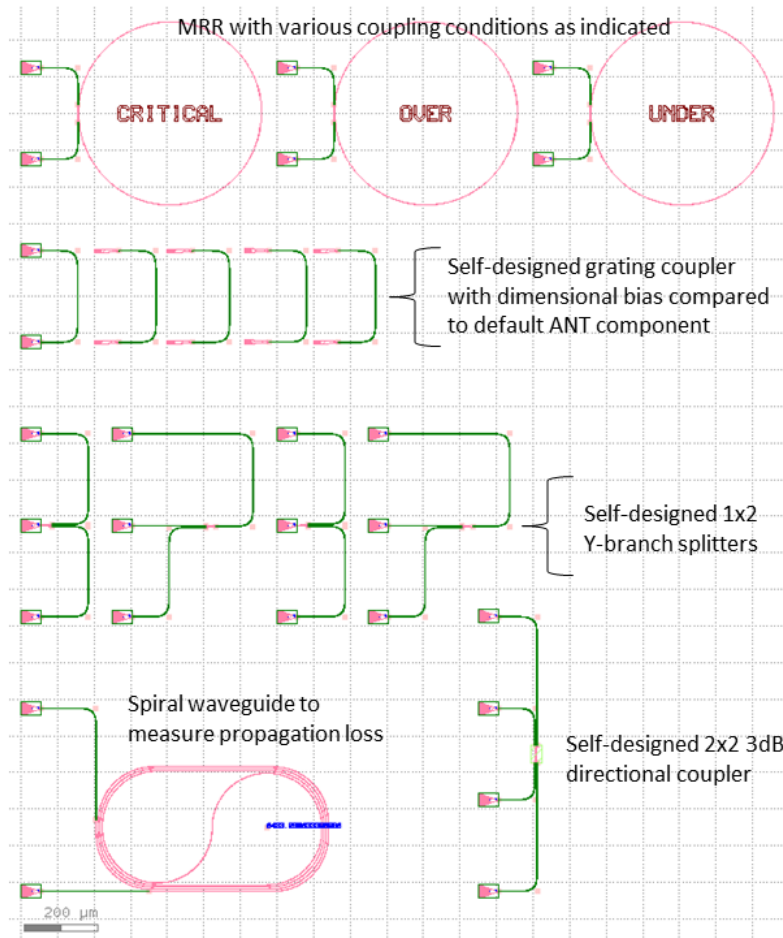


Figure B.2: Expanded view of the passive calibration circuits for evaluating and comparing the performance of photonic silicon nitride micro-ring resonators, TE polarization grating couplers, 1x2 50% y-branch splitters and combiners, 2x2 3dB directional couplers and spiral waveguides.

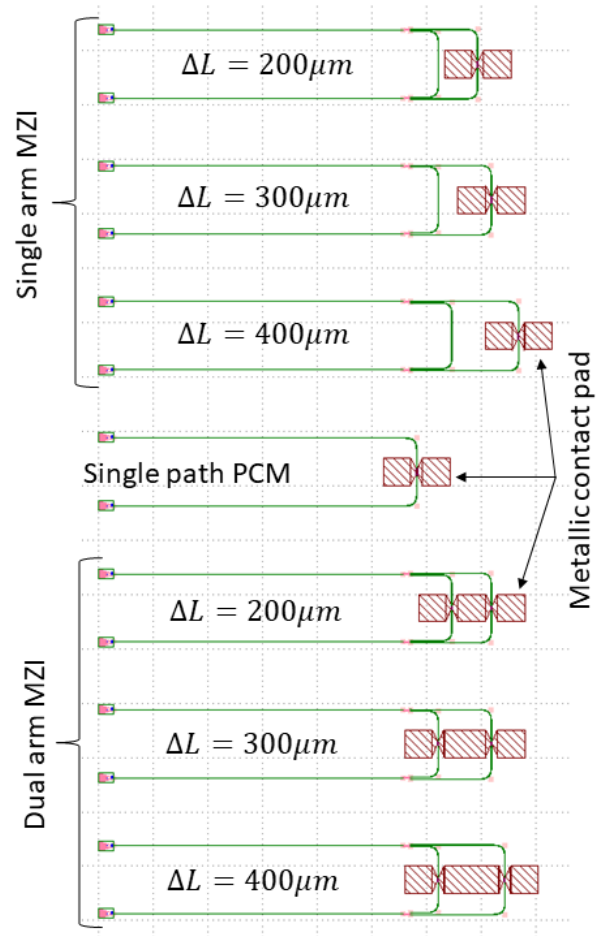


Figure B.3: 11 Column array of MZI with the incorporation of PCM in both single and dual arm configurations with metallic electrode integration to actuate a phase transition through thermal switching.

Appendix C: Silicon nitride photonic fabrication

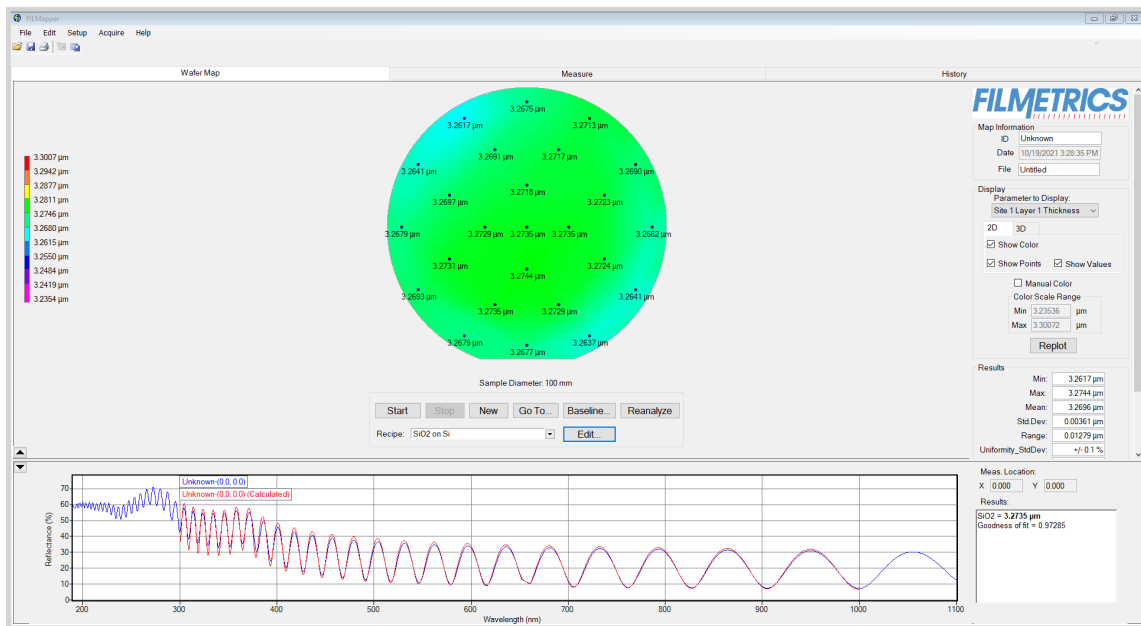


Figure C.1: Silicon dioxide thickness measurement of a 4-inch wafer via spectroscopic reflectometry tool: Filmetrics.

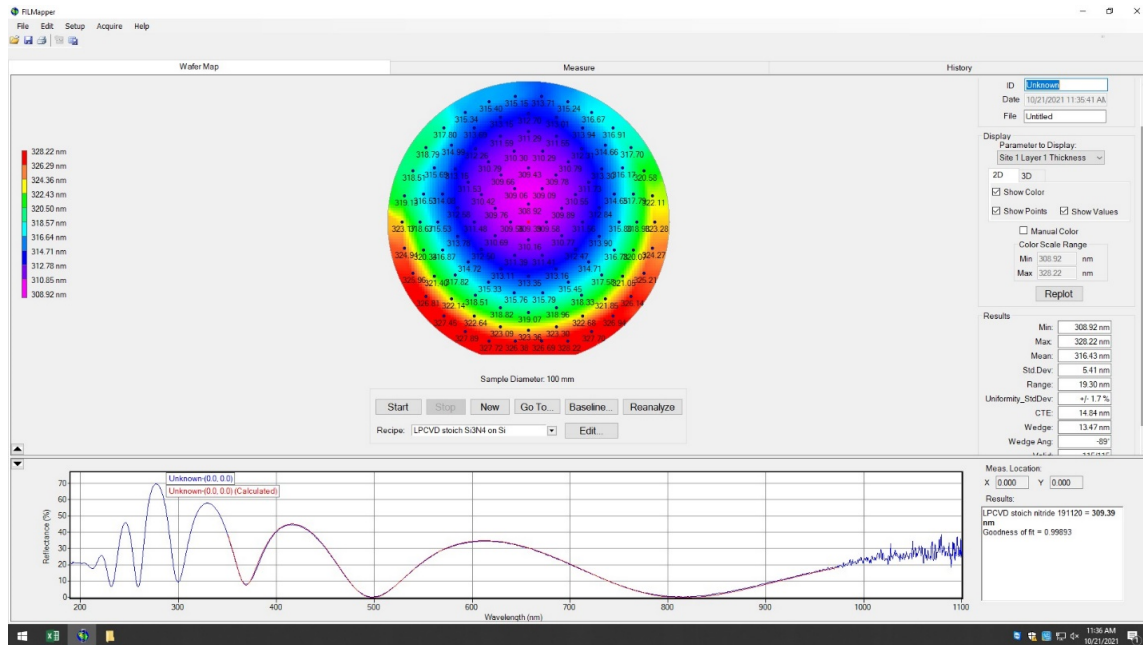


Figure C.2: Stoichiometric silicon nitride thickness measurement of a 4-inch wafer with Filmetrics metrology tool. Thickness values are represented as color with violet and red corresponding to the minimum and maximum values respectively.

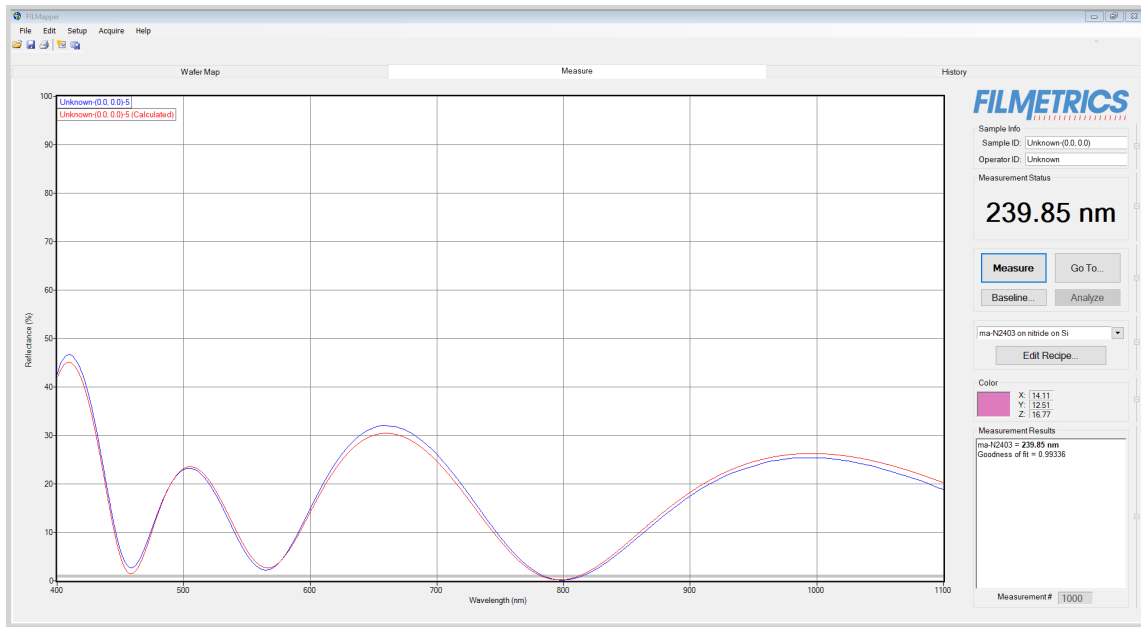


Figure C.3: Thickness measurement of photoresist Ma-N2403 on silicon nitride sample chip with Filmetrics.